

TEHNICAL UNIVERSITY
"GHEORGHE ASACHI" IAȘI
Doctoral School of the Faculty of Automatic
Control and Computer Engineering

IMAGE PROCESSING TECHNIQUES AND SEGMENTATION EVALUATION

- DOCTORAL THESIS -

PhD Supervisor:
Univ. Prof. Dr. Vasile Manta

PhD Candidate:
Eng. Cristian Smochină

Iasi, 2011

Summary

This thesis presents contributions in the field of microscopic image analysis, in particular the automatic segmentation of fluorescent images of cell nuclei and colon crypts. The evaluation methodology of the segmentation results is detailed and a new evaluation criterion is presented.

The proposed discrepancy method is based on the comparison: machine segmentation vs. ground-truth segmentation. This error measure eliminates the inconveniences that appear in the case of concave objects and allows easy control of the method sensibility regarding the objects shape similarity according to the field in which it is used.

An analysis of the most used image processing methods in microscopic image segmentation is presented by considered both the pathological fields: cytology and histology. Segmentation methods are also proposed for both fields: segmentation of the nuclei (used in cytometry) and crypts segmentation (used in hystometry).

Since the critical problem in microscopic images from tissues with colon carcinoma is the touching nuclei, three techniques are proposed to find the boundaries of touching/clustered nuclei. Since all methods need accurate background delineation, two approaches are proposed for this matter.

The segmentation problem of specific chained configurations is solved using the points with high concavity and a set of templates and rules to validate and to pair these points. The clustered/touching cell nuclei within complex structures are separated using the shape of the section profile or a cross-correlation with a specific template of the separation areas.

Regarding the histological structures, two automatic segmentation techniques robustly identify the epithelial layer/crypts. Both proposed methods use hierarchical approaches like morphological hierarchy or anisotropic diffusion pyramid. A useful study of the sampling step and a comparison between the hierarchy (without sampling) and the pyramid (with sampling) is presented. The significant implication of these techniques consists of the coarse-to-fine approach. First the high level information is preferred against the local one to allow an easy detection of the positions for the interest objects. Next, a more detailed analysis of the hierarchical representations is performed in order to obtain an accurate segmentation.

The evaluation has been done by comparison against ground-truth segmentations or by visual inspecting by a human expert. The results confirmed that the proposed methods could efficiently solve the segmentation problems of microscopic images.

Acknowledgments

I would like to thank my supervisor, Prof. Vasile Manta, for his guidance, patience, for the valuable advices and for giving me the opportunity to push my limits within this PhD. Many thanks to all members of my faculty, especially to Ms Elena Mațcu-Zbranca for her great work and patience with my administrative papers and to my colleagues for the nice collaboration: Cristina, Paul, Marius, Nicolae and Andrei.

Special acknowledgment to Eng. Radu Rogojanu from TissueGnostics GmbH and Institute of Pathophysiology and Allergy Research, Vienna who provided me the microscopic images and all the biological/medical knowledge. Without his interest and patience along with encouraging discussions on results (even not always good), this thesis wouldn't have been possible.

Special thanks to Prof. Walter Kropatsch, head of the Pattern Recognition and Image Processing Group (PRIP), Vienna for welcoming me as a former member in his group and for providing a stimulating research environment. The results of this fruitful collaboration represent an important part of this thesis. I am also very thankful to all the members of PRIP group, for the interesting and useful discussions and for the good time and special moments spent in Vienna.

I would express my gratitude to my dear mother, father, sister and grandmother for supporting me with their love every minute during my work and my education.

Contents

| | |
|---|-----------|
| Summary | 1 |
| Acknowledgments | 3 |
| Contents..... | 5 |
| I. Introduction | 9 |
| I.1. Image processing in microscopic field..... | 10 |
| I.1.1. Fluorescence microscopy images | 10 |
| I.2. Specifications for the cytological and histological tasks | 11 |
| I.2.1. Nuclei segmentation..... | 11 |
| I.2.2. Crypts segmentation..... | 12 |
| I.3. Problem statement and motivation..... | 13 |
| I.4. Summary of publications..... | 15 |
| II. Techniques used in microscopic images segmentation | 17 |
| II.1. Introduction | 18 |
| II.2. Segmentation techniques for cytological tasks..... | 19 |
| II.2.1. Thresholding and watershed | 19 |
| II.2.2. Concavity points, polygonal approximation, geometrical model fitting..... | 20 |
| II.2.3. Active contours and support vector machine..... | 21 |
| II.2.4. Graphs | 21 |
| II.2.5. Multiresolution and clusters | 22 |
| II.2.6. Artificial and Bayesian networks..... | 22 |
| II.3. Segmentation techniques for histological tasks..... | 23 |
| II.4. Discussions | 25 |
| II.5. Detailed segmentation methods..... | 29 |
| II.5.1. Region growing..... | 29 |
| II.5.2. Watershed | 29 |
| II.5.3. Anisotropic diffusion..... | 30 |
| II.5.4. Cross-correlation..... | 31 |
| II.5.5. Maximally stable extremal region..... | 32 |
| II.6. Conclusions | 33 |
| III. Segmentation evaluation methods..... | 35 |
| III.1. Introduction | 35 |

| | |
|--|-----------|
| III.1.1. Supervised evaluation criteria..... | 37 |
| III.1.2. Considered criteria | 40 |
| III.2. Discussions about the existing problems | 41 |
| III.3. Discrepancy measure based on geodesic path and curves similarity..... | 42 |
| III.3.1. Preliminaries | 42 |
| III.3.2. Distance between segmentations curves | 43 |
| III.3.2.1. Geodesic path..... | 43 |
| III.3.3. Curves similarity measure | 44 |
| III.3.3.1. The error from the segmented to the reference curve..... | 44 |
| III.3.3.2. The error from the reference to the segmented curve..... | 46 |
| III.3.4. Segmentation error..... | 46 |
| III.3.5. Particular example..... | 47 |
| III.4. Results | 49 |
| III.4.1. Synthetic test images..... | 49 |
| III.4.2. Real test images | 50 |
| III.5. Conclusions | 54 |
| IV. Segmentation techniques for cytometry..... | 55 |
| IV.1. Introduction | 55 |
| IV.2. Background detection..... | 57 |
| IV.2.1. Detection using region growing..... | 57 |
| IV.2.2. Detection using image reconstruction and hysteresis thresholding | 58 |
| IV.3. Nuclei segmentation within chained configurations..... | 59 |
| IV.3.1. Concave points detection..... | 59 |
| IV.3.2. Separation segments validation using geometrical information..... | 60 |
| IV.3.2.1. Geometrical templates for touching nuclei..... | 61 |
| IV.3.2.2. Validation rules | 62 |
| IV.3.3. Results | 63 |
| IV.3.3.1. Evaluation | 65 |
| IV.4. Touching nuclei detection using profile shape | 66 |
| IV.4.1. V-shape detection..... | 66 |
| IV.4.1.1. Particular example..... | 66 |
| IV.4.1.2. Validation the separation regions..... | 68 |
| IV.4.1.3. Region growing for more accurately separation regions..... | 68 |
| IV.4.2. Watershed for detecting boundaries of full nuclei..... | 69 |
| IV.4.2.1. Merging regions | 70 |
| IV.4.3. Results | 70 |
| IV.5. Touching nuclei detection using cross-correlation | 72 |
| IV.5.1. Cross-correlation with a Gaussian-complement..... | 73 |
| IV.5.1.1. Separation regions enhancement using the anisotropic diffusion | 74 |

| | |
|--|------------|
| IV.5.2. Detecting the separation regions | 74 |
| IV.5.3. Watershed on distance transform..... | 75 |
| IV.5.4. Results | 76 |
| IV.5.4.1. Evaluation | 76 |
| IV.6. Conclusion..... | 78 |
| V. Segmentation techniques for hytometry | 81 |
| V.1. Epithelial layer segmentation in DAPI stained nuclei images | 81 |
| V.1.1. Lumens segmentation using the morphological hierarchy..... | 82 |
| V.1.1.1. Building the morphological hierarchy..... | 83 |
| V.1.1.2. Lumen reconstruction..... | 83 |
| V.1.2. Crypt's outer border | 85 |
| V.1.2.1. Lumen validation..... | 85 |
| V.1.2.2. Outer border detection..... | 86 |
| V.1.3. Results | 87 |
| V.2. Sampling step importance in hierarchical semantic segmentation | 87 |
| V.2.1. Motivation | 88 |
| V.2.2. Lumens segmentation using the morphological pyramid..... | 89 |
| V.2.2.1. Moving from un-sampled to sampled domain | 90 |
| V.2.2.2. Lumen reconstruction..... | 92 |
| V.2.3. Filtering and sampling vs. sampling and filtering | 92 |
| V.2.4. Results | 93 |
| V.3. Epithelial area detection in cytokeratin microscopic images | 95 |
| V.3.1. Image enhancement..... | 96 |
| V.3.2. Crypt outer borders detection | 97 |
| V.3.2.1. Anisotropic diffusion pyramid..... | 97 |
| V.3.3. Crypts separation and lumen detection | 99 |
| V.3.3.1. Crypts separation..... | 100 |
| V.3.3.2. Lumen detection..... | 100 |
| V.3.4. Results | 102 |
| V.4. Conclusions | 104 |
| VI. Conclusions | 105 |
| VI.1. Contributions | 105 |
| VI.1.1. Segmentation evaluation criteria..... | 105 |
| VI.1.2. Image processing techniques used in microscopic image analysis..... | 105 |
| VI.1.3. Cell nuclei segmentation within complex arrangement structures | 106 |
| VI.1.4. Semantic segmentation of the epithelial layer/crypts..... | 106 |
| VI.1.4.1. The relationship between the sampled and un-sampled domain..... | 107 |
| VI.2. Future research..... | 108 |
| References..... | 109 |

I. Introduction

Image segmentation is a critical task in automatic image analysis and a fundamental step of low-level vision which provide important information for further image understanding. In many image analysis applications, it is often the first, most important and most difficult step. Due to its importance, a great variety of segmentation algorithms have been proposed in the last few decades for a wide range of applications and domains. Medical image analysis received a considerable attention from researchers due to its practical and vital applications for human health. In this thesis, our particular interest is on microscopic image processing and its evaluation.

In diagnostic pathology, the pathologists give a diagnostic after a set of biological samples (tissues stained with different markers) are viewed and many specific features of the objects of interest (size, shape, colour or texture) have been analysed. This complex, time consuming and tedious diagnostic process is an important part in clinical medicine but also in biomedical research and can be enhanced by providing the pathologists or the researchers with quantitative data extracted from the images.

The image processing techniques are of special interest because they allow large scale statistical evaluation in addition to classical eye screening qualitative valuation. These additional information and the accurate measurements of the objects parameters with a computer aided image processing system are used in both sections of pathology: cytology (the study of cells) and histology (anatomical study of the microscopic structure of tissues) [Ta, *et al.*, 2009].

Beside the segmentation algorithms, it is indispensable to have a robust technique to evaluate the performance of these algorithms, to characterize and to highlight the situations where the results offered by algorithms do not satisfy the requirements imposed by the field in which they are used. Performance evaluation is critical for all computer vision algorithms and up against segmentation, relatively fewer effort have been spent for building an evaluation method usable in any computer vision field [Zhang, 1996].

In this dissertation we present new contributions and significant improvements in automated cytological and histological segmentation and segmentation evaluation.

I.1. Image processing in microscopic field

To overcome the possible subjectivity caused by different visual interpretations of different pathologists, image processing techniques are used because they allow large scale statistical evaluation in addition to classical eye screening evaluation.

Tissue development and disease-related processes such as tumorigenesis are determined in large part by communication between neighbouring cells. Therefore, it is necessary to analyse and to monitor the status of each cell in its natural tissue environment [Baggett, *et al.*, 2005].

I.1.1. Fluorescence microscopy images

The phenomenon of fluorescence refers to the emission of light at a different and usually longer wavelength than the illumination. Fluorescence (FL) microscopy uses the fluorescence properties of the applied immunological markers to acquire microscopic images of biological samples. The fluorescence is introduced during tissue sample preparation. Depending on the fluorescence marker used on tissues, different biological components (proteins) can be highlighted. In FL microscopy, the fluorescent probes bind certain proteins like deoxyribonucleic acid (DNA) or cytokeratins from tissue samples.

In this study, we are interested in visualizing two types of objects (biological proteins): nucleus (contains DNA) and crypts (cell structures composed of epithelial cells highlighted by their cytokeratins).

The fluorescent marker Di Aminido Phenyl Indol (DAPI) [Morikawa and Morikawa, 1981] is used to visualize the cell nuclei. This stain binds strongly to DNA which is present only in the cell nucleus. DAPI labels specifically cell nuclei and it is used as a counterstaining in multicolour fluorescent techniques. DAPI is capable to intercalate into DNA attaching the minor groove of A-T rich DNA sequences, forming a fluorescent complex. Nuclei have the normal phenotype when the staining is bright and homogenous. Apoptotic nuclei can be identified by the condensed chromatin accumulating at the periphery of the nuclear membrane or by a total fragmented morphology of nuclear bodies [Kapuściński and Skoczylas, 1978]. In Fig.I.1a the bright area represents the nuclei and is the binding result between the DAPI and DNA from the cell nucleus.

To separate the epithelial layer (crypts), immunofluorescence staining is performed in paraffin embedded sections with the anti-cytokeratin 8 (CK-8) antibody and a fluorochrome-labelled secondary antibody [Moll, *et al.*, 2008]. The CK-8 is used because it reacts with cytokeratins, proteins found only in the cytoskeleton of epithelial cells. In Fig.I.1b the bright area is the binding result between the CK-8 and the epithelial components; the small dark regions within the crypts are caused by the epithelial nuclei and their lack of cytokeratins.

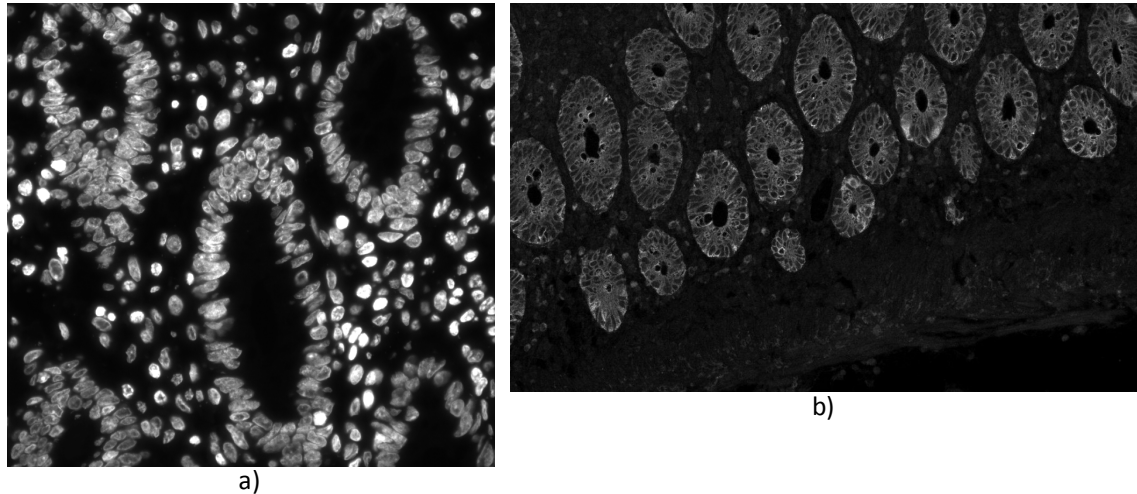


Fig.1.1 Fluorescence images of colon tissue stained with DAPI a) and CK-8 b) markers.

In classic microscopy, the tissue sample is placed between a source of visible light and digital microscope camera. The light is either absorbed by or transmitted through the sample depending on its consistency. In FL, the recorded light is the fluorescence of the used markers. This work uses 8 bit grey-scale images acquired using the automated TissueFAXSTM slide scanner (TissueGnostics GmbH, Austria).

I.2. Specifications for the cytological and histological tasks

This study focuses on automatic analyses of the images obtained from colorectal tissue sections containing the following two proteins responses: DNA (images with cells nuclei, Fig.I.1a) and cytokeratins (images with crypts, Fig.I.1b).

The following biological information must be extracted: the nuclei from the DAPI images (e.g., Fig.I.1a, Fig.IV.1) and the crypts from the DAPI (Fig.V.1a) and CK-8 images (Fig.I.1b, Fig.V.10). The core of this work lies in the two segmentation tasks: the first one which must find the boundaries of the cells nuclei and the second one which detect the crypts. The segmentation results must be evaluated and compared with the human solution for these particular tasks.

I.2.1. Nuclei segmentation

There are two main types of nuclei according to their position: isolated and clustered/touching. Segmentation of nuclei in grouped structures introduces additional problems compared with the isolated ones because these are in a close packing arrangement, often in contact with their neighbours [Baggett, *et al.*, 2005].

By analysing the content of these images (e.g., Fig.I.1a, Fig.IV.1) we can highlight the common problems that appear, problems pointed out also in other papers which present research in this field [Nattkemper, 2005]:

- different grey values for the background caused by the non-uniform illumination;
- the cells or nuclei structures can appear as artefacts in the non-uniformly stained slices;
- low contrast and weak boundaries on out-of-focus nuclei;
- the physical structure of the cells, as well as their biological status at the moment of sample prelevation determine a non-uniform distribution of material inside the nucleus, often denser near the border and with lower intensities within the nuclei [Todman and Claridge, 1997];
- strong variation can appear inside the nuclei which may mislead the segmentation algorithm;
- considerable variation of object features like shape and/or size and/or orientation and different nuclei distribution within the epithelial layer;
- besides isolated nuclei, clustered or touching cell nuclei have very weak boundaries and often are not convex.

Some epithelial nuclei from tumour area might look slightly bigger and with an overall lower intensity than those of normal cells due to an intense nuclear activity and DNA decondensation. However, as such differences in appearance are not well studied and are not accepted criteria for tumour diagnosis, the methods should detect all the nuclei, i.e., to find the boundary for each nucleus. The proposed methods related to nuclei segmentation are detailed in Section IV.

I.2.2. Crypts segmentation

The epithelial layer of the human colon is made up of epithelial cells and forms the basic functional unit of the intestine: the crypt (crypt of Lieberkühn) [Humphries and Wright, 2008]. Each crypt comprises two main structures of interest: the lumen and the epithelial layer (Fig.I.1). The epithelial layer contains epithelial nuclei and surrounds the lumen which is an empty area. The interstitial cells on the other side form heterogeneous regions (stroma) placed between crypts which contains the extra cellular matrix (ECM), fibroblasts, macrophages, vessels etc.

The task is to analyse the tissue components like crypts, lumen and stroma, without dealing directly with the small objects like nuclei and cells. A rough description and a short overview of the problems to be solved are presented below:

- some images are slightly underexposed due to weak local biological response;
- some image portions don't contain useful information;
- the crypt appears like a "donut" (or 2D projection of a torus) with many small 'holes' and a central black area inside (lumen) (Fig.I.1b);

- the lumen is a black area with different sizes surrounded by the epithelial layer;
- the “donut” has a non-homogeneous organization due to the dark regions smaller than the lumen;
- the pixels within a crypt correspond to three main components: i) background, dark regions and the noisy pixels, ii) weak biological binding response and iii) strong response (highest values);
- the stroma separates the crypts but situations of touching/very close crypts can appear;
- no relevant information or cells exist between touching/very close crypts;
- the number of crypts may be used in computing distribution statistics.

The proposed techniques should extract the crypts components (lumen and epithelial layer), i.e., to find the inner and the outer boundaries of the crypt. The proposed methods related to crypts segmentation are detailed in Section V.

I.3. Problem statement and motivation

The objective of segmentation in the microscopic images is to extract the cellular, nuclear or tissue components, i.e. to find the boundaries for the cells, cells nuclei or histological structures from stained tissues with different markers with an adequate accuracy. This problem is challenging due to the large variations of the features from these components, variations which are probably more present and accentuated here than in any other field. The problems shown in I.2 confirm that the segmentation of microscopic images is a hard task.

Intensive research is done in biology and cytometry/histometry to develop treatments for different diseases by analysing how the cell, cell nucleus or biological structure reacts to some probes/treatment. One mandatory tool for these investigations is the automated microscopic image analysis able to provide significant information from huge amount of data/images in a short time.

Three major issues arise. First, the low-level biological object like cell nuclei have to be detected in a reliable way. The second issue refers to histological structures detection (crypts). The last one imposes the performance evaluation of the segmentation results.

- **Cell nuclei segmentation.** The main motivation for nuclei segmentation is to provide the pathologists and researchers with quantitative data regarding the nuclei arrangements and different type of statistics (size, area, intensities distribution, organization structures, density). Research on cellular systems (cytomics) allows an analysis of cell heterogeneity in different cell systems (cytomes). The analysis of the cytological parameters for each cell in their natural tissue environment gives a much

broader perspective of tissue development in both normal and diseased cases [Baggett, *et al.*, 2005]. Several segmentation methods have been developed due to the great diversity of biological samples where different artefacts and feature must be manually or automatically recognized [Guimarães, *et al.*, 2000], [Figueiro, *et al.*, 2003];

- **Crypts segmentation.** The main motivation for segmenting crypts is to provide the pathologists with quantitative data regarding the epithelial area (crypts boundaries) and epithelium-to-stroma ratios. These ratios may provide important information for the assessment of cancer in colon or other organs [de Kruijf Esther, *et al.*, 2011]. If the DAPI images are used, one alternative approach is to segment each nucleus and to analyse the structures that they form. Since this approach can encounter additional problems, the objective is to directly find the boundaries of the crypts, i.e. to delineate the area covered by the epithelial nuclei without dealing with the individual nuclei;
- **Segmentation evaluation.** Automatic segmentation is much faster than visual analysis and does not suffer from the disadvantages of the typical human analysis like subjectivity and fatigue of the evaluator. Samples from more patients can be evaluated, thus providing data which is more relevant from a statistical point of view. As segmentation applied on large amounts of data produces an equally large number of masks, a rigorous analysis and evaluation of the segmentation performance is mandatory.

I.4. Summary of publications

This thesis is mostly based on 10 published papers in journals (3), conferences indexed by IEEE Xplore (2), Springer Lecture Notes in Computer Science-LNCS (1) and Bioinformatics-LNBI (1), ACM (1) and others international conferences (2). A complete list of the publications that support this thesis is presented in this section, as follows:

- Chapter II is based on:
 - ✓ **Cristian Smochina**, Vasile Manta, *Industrial inspection system using triangulation*, In Journal Buletinul Institutului Politehnic din Iasi, Tom LVI (LVIII), fasc. 3-4, Automatic Control and Computer Science, pp. 75-82, 2008 [**Smochina and Manta, 2008**].
 - ✓ **Cristian Smochina**, Paul Herghelegiu and Vasile Manta, *Image processing techniques used in microscopic image segmentation*, In Journal Buletinul Institutului Politehnic din Iasi, Automatic Control and Computer Science, Tom LVII (LXI), fasc. 2, pp. 83-98, 2011 [**Smochina, et al., 2011e**].
- Chapter III contains results presented in:
 - ✓ **Cristian Smochina**, Vasile Manta and Radu Rogojanu, *New discrepancy measure for evaluation of segmentation quality*, In Proc. 11th IASTED International Conference on Computer Graphics and Imaging, Innsbruck, Austria, track 679-053, 2010 [**Smochina, et al., 2010a**].
- The results presented in Chapter IV are published in:
 - ✓ **Cristian Smochina**, Vasile Manta, Giovanna Bises and Radu Rogojanu, *Automatic cell nuclei detection in tissue sections from colorectal cancer*, In Proc. 14th International Conference on System Theory and Control, Sinaia, Romania, pp. 519-524, 2010 [**Smochina, et al., 2010b**].
 - ✓ Radu Rogojanu, Giovanna Bises, **Cristian Smochina** and Vasile Manta, *Segmentation of cell nuclei within complex configurations in images with colon sections*, In Proc. IEEE 6th International Conference on Intelligent Computer Communication and Processing, Cluj-Napoca, Romania, pp. 243-246, 2010 [**Rogojanu, et al., 2010**].
 - ✓ **Cristian Smochina**, Anca Serban and Vasile Manta, *Segmentation of cell nuclei within chained structures in microscopic images of colon sections*, In Proc. 27th Spring conference on Computer Graphics, Viničné, Slovak Republic, pp. 146-154, 2011 [**Smochina, et al., 2011a**].

- ✓ Paul Herghelegiu, **Cristian Smochina** and Vasile Manta, *GPU method for registering multiple MRI sequences*, In Journal Buletinul Institutului Politehnic din Iasi, Automatic Control and Computer Science, Tom LVI(LX), fasc. 4, pp. 175-183, 2010 [**Herghelegiu, et al., 2010**].
- Chapter V contains results presented in:
 - ✓ **Cristian Smochina**, Vasile Manta and Walter Kropatsch, *Semantic segmentation of microscopic images using a morphological hierarchy*, In Proc. 14th International Conference on Computer Analysis of Images and Patterns, Seville, Spain, LNCS 6854, pp. 102-109, 2011 [**Smochina, et al., 2011b**].
 - ✓ **Cristian Smochina**, Radu Rogojanu, Vasile Manta and Walter Kropatsch, *Epithelial area detection in cytokeratin microscopic images using MSER segmentation in anisotropic pyramid*, In Proc. 6th IAPR International Conference on Pattern Recognition in Bioinformatics, Delft, The Netherlands, LNBI 7036, pp. 318, 2011 [**Smochina, et al., 2011c**].
 - ✓ **Cristian Smochina**, Vasile Manta and Walter Kropatsch, *Sampling step importance in hierarchical semantic segmentation of microscopic images*, In Proc. 15th International Conference on System Theory and Control, Sinaia, Romania, pp. 570, 2011 [**Smochina, et al., 2011d**].

The conclusions and future researches can be found in Chapter VI.

II. Techniques used in microscopic images segmentation

The objective of semantic segmentation in microscopic images is to extract the cellular, nuclear or tissue components. This problem is challenging due to the large variations of features of these components (size, shape, orientation or texture). In this chapter an overview of the proposed segmentation techniques for microscopic images is presented. This is not a comprehensive study, but rather an analysis of the most used image processing methods in this particular domain. The existing techniques are grouped by their application in either cytology or histology. Beside a rough description of each method, a useful statistic and discussion about the frequency of the most used image processing methods in the problem of microscopic image segmentation is presented. This analysis is helpful for a better use of existing method and for improving their performance as well as for designing new ones.

Due to the difficulty of the segmentation task caused by high variability of the microscopic image content regarding objects as well as background, many techniques deliberately included a small amount of proactive user interaction to guide the segmentation procedure. For instance, to guarantee correct segmentation of every cell, the algorithm presented in [Baggett, *et al.*, 2005] required the user to mark two points per cell, one approximately in the centre and the other on the border. Task of automatic segmentation on microscopy images is generally ranked as a demanding one [Nattkemper, 2005]. The publications related to the image processing applied on microscopy images are wide-spread in literature, i.e. through the fields of microscopy, biomedical engineering, biomedical imaging, bioinformatics and pattern recognition.

This chapter is organized as follows. Segmentation techniques for cytological tasks are described in Section II.2 and for histological tasks in Section II.3. The obtained statistics are presented and discussed in Section II.4. Some segmentation methods used further in the proposed techniques in this thesis are detailed in II.5, while the conclusions and segmentation methods tendencies are elaborated in Section II.6.

II.1. Introduction

Image processing techniques have been widely used in the last decade in medical imaging; the microscopic field received a consistent effort from researchers. Considering the importance of the pathological results for human health and the applications difficulties, many computer aided image analysis systems have been proposed [Ta, *et al.*, 2009]. The complex diagnostic process (time consuming and tedious process) can be enhanced by providing the pathologists or the biologists with quantitative data extracted from the images.

The image processing techniques are of special interest because they allow large scale statistical evaluation in addition to classical eye screening evaluation and are used in both sections of the pathology: cytology (the study of cells) and histology (anatomical study of the microscopic structure of tissues).

Due to its importance, a great variety of segmentation algorithms have been proposed for a wide range of applications and the publications are wide-spread in literature: microscopy, biomedical engineering, biomedical imaging, bioinformatics and pattern recognition [Nattkemper, 2005].

The task of segmentation in microscopic images refers to the process of finding the boundaries of cells, cells nuclei or histological structures with an adequate accuracy from images of stained tissues with different markers. The considered papers study different image types from colon, intestinal, breast, prostate, blood, bone marrow, mammalian, thyroid, cervical, esophageal, lymphatic obtained with different markers, e.g., DAPI, immunodetection of lamin A/C, hematoxylin and eosin, Papanicolaou stain.

II.2. Segmentation techniques for cytological tasks

A classification based on the used segmentation algorithms is difficult because almost all proposed techniques combine at least two image processing methods. The techniques from this section are grouped based on the relevant/critical image processing method which makes the difference to other approaches and considerably improves the segmentation quality [Smochina, *et al.*, 2011e]. For instance, in section II.2.1 the methods which use the thresholding and/or the watershed are presented. Some papers from II.2.2 also use watershed but the key of the techniques is given by the geometrical model fitting [Cong and Parvin, 2000] or by the concavity points [Wahlby, *et al.*, 2004]. Another example refers the paper [Srinivasa, *et al.*, 2009] that uses the active-contour method (specific for papers from II.2.3) but the efficiency of the proposed technique is given by the coarse-to-fine analysis; this is way it is presented in II.2.5.

II.2.1. Thresholding and watershed

Using the classical image processing techniques, the authors obtained in [Ta, *et al.*, 2009] an accuracy of 90% for the segmentation of cell nuclei clusters from peripheral blood and bone marrow preparations. A threshold obtained with the Otsu's method is applied on the fluorescence microscopic images after a shading correction and background subtraction have been performed. The watershed algorithm is run on the inverse distance transform of the morphological gradient.

Similar images of fluorescence labelled cell nuclei like those used in [Ta, *et al.*, 2009] are also processed in [Wahlby, *et al.*, 2004]. The difference comes from the method used to obtain the watershed seeds. The seeds for object and background were obtained by combining morphological filtering on both the original image and the gradient magnitude of the image. The over-seeded situations are solved by merging two regions judging by the mean value of the border. The same percentage as [Ta, *et al.*, 2009], 90% correct segmentation has been reported.

The watershed segmentation is used to detect individual nucleus in the special problem of cell populations growing in complex clusters [Angulo, 2008]. A probabilistic algorithm counts the number of nuclei in a cluster. The separation or merging (after applying the watershed) is presented in a more complex approach in [Cheng and Rajapakse, 2009].

The adaptive thresholding and watershed is also used in [Zhou, *et al.*, 2009] for nuclei segmentation. In addition, to improve the cell identification accuracy a set of features and the context information is used in a Markov model.

Since the thresholding method is a powerful tool, a novel method to automatically determine the threshold levels (the stable count thresholding, SCT) is proposed in [Russell, *et al.*, 2009] for mammalian cell nucleus segmentation. The results show that the segmented

images with SCT algorithm are closer to the ground-truth segmentation than the Otsu's thresholding method, Isodata or mixture modelling thresholding. The adaptive thresholding is also mainly used in [Madhloom, *et al.*, 2010] to identify five types of white blood cell nucleus.

Considering the often use of thresholding combined with watershed, the authors in [Coelho, *et al.*, 2009] perform an objective evaluation of the nuclear segmentation algorithms based on these methods. They compare the segmentations with a dataset of hand-segmented fluorescence microscopy images. The following methods are used: three thresholding methods (Ridler-Calvard, Otsu and mean pixel value), two versions of seeded watershed (on blurred and gradient) and merging criteria based on shape features (fraction of area that is contained in the convex hull, roundness, eccentricity, area, perimeter, semi-major, and semi-minor axes).

II.2.2. Concavity points, polygonal approximation, geometrical model fitting

The method from [Wahlby, *et al.*, 2004] includes more knowledge about the shape and the nuclei distribution. The lamin A/C fluorescent staining is used to visualize the DNA. After detecting the clusters of cells nuclei, the significant concavity points are detected. A set of geometrical templates use these points to detect the aggregated and the overlapped nuclei configurations. Having this important information, the watershed is used to separate the nuclei based on the intensities values of the separation regions between them. The technique gives 97.47% well segmented nuclei in terms of number of nuclei, according to biological experts.

The concavity points between nuclei are also used in [Cong and Parvin, 2000] to delineate the nuclei observed with an epi-fluorescence microscope. After a thresholding, the boundaries of the detected regions are polygonal approximated. The interesting approach comes from analysing the corners of this polygonal approximation to highlight the concavity points. These points split the boundary into certain segments. A hyperquadric model is used to fit these segments such that the fitted results indicate the nuclei boundaries.

In [Angulo, 2008] *a priori* knowledge with respect to the shape of nuclei is considered. The watershed segmentation is applied on the H -minima transform with optimal h -value. Similar to [Cong and Parvin, 2000], the segmented region boundaries are improved by fitting an ellipsoidal model.

The critical problem of touching cells is addressed in [Bai, *et al.*, 2009]. After a contour detection based on morphological filtering and adaptive thresholding, the concave points are detected from the polygonal approximation. The advantages of this polygonal approximation, i.e., smoothing, reducing computation time, critical points have been also pointed out in [Cong and Parvin, 2000]. The concave points split the contours into segments. Considering the ellipse-like shape, a customized ellipse fitting is applied such that each segment of the contour has a fitted ellipse.

II.2.3. Active contours and support vector machine

Beside the mostly used techniques like thresholding and watershed, also the online support vector classifier is used. In [Wang, *et al.*, 2008] the authors pointed out the lack of global threshold to offer good results. They detect the background using estimation with cubic B-spline, differently from [Cong and Parvin, 2000], [Zhou, *et al.*, 2009] or [Bai, *et al.*, 2009] where thresholding was used. An interesting particle algorithm is used by putting one particle in a pixel; this particle is moved along the gradient vector of the pixel (gradient vector field). At the end of moving process, a thresholding is used to detect the local maxima; the cells are segmented via seeded watershed. After a huge set of features are extracted, online support vector classifier is trained to detect different evolution phases of the cell.

A new learning method based on support vector machine (SVM) is proposed in [Lebrun, *et al.*, 2007] for segmenting the cells stained with Papanicolaou stain. The authors point out the importance of classifier design when used in segmentation tasks and presented a technique to reduce the complexity of decision functions produced by SVM.

The segmentation of Papanicolaou stained cervical cell images have been also addressed in [Bamford and Lovell, 1998]. In this paper the active contours is combined with the Viterbi algorithm resulting in a 99.64% correctly segmented images.

The cells are detected in [Yang, *et al.*, 2005] using a gradient vector flow snake adapted for colour images. An interesting comparison is made with segmentation techniques based on mean-shift and watershed algorithm.

The leukocytes segmentation in images of bone marrow samples have been research in [Nilsson and Heyden, 2005]. Firstly the leukocytes are located using level set methods and the watershed. In the second part, a set of features (area, compactness, and variance) is used to validate the correct segmented objects and to assembly the over-segmented cell parts).

An improved active contour model is proposed in [Hu, *et al.*, 2004] to isolate each cell nucleus from esophageal cell images. The cell nuclei are localized using the ultimate erosion and dual thresholds.

The important role of active-contour based algorithms has been shown in many researches [Malpica and de Solorzano, 2002] and in [Dzyubachyk, *et al.*, 2008] some shortcomings have been improved for better segmentation accuracy and tracking robustness.

II.2.4. Graphs

A different fully automated approach based on graph cut model is proposed in [Danek, *et al.*, 2009] for segmenting the touching cell nuclei. The minimal geodesic length is used first to separate the background and the foreground. The individual nuclei are found by a graph cut which include image gradient information and *a priori* knowledge about the shape of the nuclei. The graph-cut is also used in [Yang and Choe, 2009] for cells segmentation for the tracking problem in microscopy images.

In [Ta, *et al.*, 2009] an interesting approach is proposed by discrete modelling the images by weighted graphs of arbitrary topology.

II.2.5. Multiresolution and clusters

The multiresolution analysis plays an important role in medical image processing. In [Colantonio, *et al.*, 2007] a coarse-to-fine approach is used for cell segmentation in lymphatic tumours. Instead of thresholding, a cluster analysis based on the fuzzy c-means algorithm is performed to provide a rough automatic segmentation of the clustered regions. For cell contour extraction an artificial neural network (ANN) is trained considering as features the colour and mean values, gradient norm and radial gradient.

The multiresolution approach combined with a k-means clustering algorithm is used in [Begelrnan, *et al.*, 2004]. After the edges have been extracted, a second-order polynomial-fitting algorithm is run. Similar to [Cong and Parvin, 2000], the fitted polynomial is analysed (concavity, convexity, zero crossing) to distinguish between different contour profiles.

Another classification used in nuclei cell segmentation based on fuzzy logic engine [Begelrnan, *et al.*, 2004] is proposed for segmenting the prostate tissue samples stained by hematoxylin and eosin (H&E). The fuzzy rules are based on shape properties, normalized cross correlation with nucleon template and colour features and a mixture of Gaussian distributions.

A more complex technique is presented in [Srinivasa, *et al.*, 2009] where some important methods are combined, i.e., the flexibility of the active-contour methods is used for foreground detection and the multiresolution approach give computation advantages by coarse-to-fine analysis. Also smoothing into this multi-scale structure and region-growing methods are used.

II.2.6. Artificial and Bayesian networks

A comprehensive study of ANN (also used in [Colantonio, *et al.*, 2007]) is presented in [Boland and Murphy, 2001]. Different sets of fluorescence images with different antibodies responses have been analysed judging their protein localizations patterns. A consistent group of features have been computed: the number of objects, the Euler number, the variance and average of pixels intensities, gradient homogeneity, edges directions, convex hull, eccentricity, Zernike and Haralick features, etc. Back-propagation neural networks (BPNNs) were implemented and trained to classify populations and individual cells.

To overcome the computational power of neural networks, the spiking neuron networks (SNNs) are used in the segmentation of the cellular microscopic images [Meftah, *et al.*, 2010]. Two different topologies are used for supervised (a reference data set of pixels from different images) and unsupervised (learning directly on the pixels of the image) learning.

A new method for leucocytes segmentation based on nuclei classification is presented in [Jeong, *et al.*, 2009]. Two configuration situations are detected based on Bayesian networks:

overlapping and isolated. The morphological features of the nuclei, such as the compactness, smoothness and moments are used and the watershed finds the proper nuclei boundaries.

A more detailed description from a machine learning perspective of the naive Bayesian classifier, neural networks and decision trees used in medicine is shown in [Kononenko, 2001].

Beside the cell nuclei segmentation, in [Yang, *et al.*, 2006] also the nuclei tracking are performed in a video sequence. The cells are segmented using a novel marker-controlled watershed. Considering the ellipse shape of the cell nuclei, the classical Gaussian kernel based mean shift have been modified by adding kernels with scale, shape, and direction adaptation. Together with Kalman filter, a 98.8% cell nuclei segmentation accuracy is achieved.

3D confocal images of normal human skin and human breast specimens are analysed in [Solorzano, *et al.*, 1999]. The automatic segmentation is performed on each slice using adaptive thresholding and morphological segmentation.

II.3. Segmentation techniques for histological tasks

Beside the nuclei segmentation attempts presented above, also the segmentation of histological structures like gland or crypt has been addressed in many studies.

In [Wu, *et al.*, 2005] the human intestinal gland images are segmented using a region growing algorithm. The seeds are identified considering the big empty area inside the intestinal glands. The regions are grown till the closed chain structured formed by epithelial nuclei is covered. Only small gaps between the neighbouring nuclei are considered.

The glands from prostate tissue images are segmented [Farjam, *et al.*, 2007] using particular texture features for the gland components (stroma, lumen, nuclei). K-means clustering is applied to group these features in three clusters corresponding to gland components.

Prostate cancer tissues is also analysed in [Naik, *et al.*, 2007]. Beside the prostate glands segmentation, the malignancy is automatically graded (Gleason system). A trained Bayesian classifier is used to detect the glands and a level-set is evolved to proper delimit the gland. Based on the found areas, morphological features are computed to characterize the glands. The SVM is used to select the corresponding Gleason grade for a certain tissue based on its morphology. In [Naik, *et al.*, 2008], beside the prostate tissues images, the breast cancer images are analysed and graded using the low-, high-level and domain-specific information.

An object-graphs approach is described in [Gunduz-Demir, *et al.*, 2010] where the primitive objects (nucleus and lumen) and the relationship between them are included into graphs. The high level information is preferred against the local one in segmenting the colon glands from H&E stained images.

The microscopic thyroid images are analysed in [Chen, *et al.*, 2008], in order to classify varying tissue types. To identify the texture types, the following image features have been used: hue, brightness, standard deviation of brightness, entropy, energy, regularity, and fractal analysis. The split/merge process is based on quad-tree based image segmentation technique.

If the methods presented in the previous chapter try to segment each cell nucleus, in [Dalle, *et al.*, 2009] the nuclear pleomorphism scoring is performed by selecting and segmenting only the critical cell nuclei within a high-resolution histopathological image. After an image enhancement, a threshold is applied to detect the critical cell nuclei, i.e. the epithelial cells. The nuclei clusters are highlighted using morphological filtering and the nuclei boundaries are found in polar space.

Considering the encountered problem in nuclei segmentation, in [Boucheron, *et al.*, 2010] the classification of H&E stained histopathology imagery of breast cancer (benign vs. malignant) is investigated using imperfectly segmented nuclei. The authors proved that using a set of object-level features and a linear classification, accuracy above 70% is obtained using imperfectly segmented nuclei.

The biological structures are processed in histology images [Mosaliganti, *et al.*, 2009] considering the density-maps. The segmentation is performed using variational level-set for density-based segmentation of the cellular structures.

In [Chen and Lee, 1997] the mammographic images are hierarchically decomposed into different resolutions and segmented by analysing the coarser resolutions while in [Roshni and Raju, 2011] the multiresolution wavelet analysis is used for texture classification.

A Gaussian multiresolution segmentation technique is combined in [Tolba, *et al.*, 2003] with the expectation maximization (EM) algorithm to overcome the drawbacks of the EM algorithm.

Considering the wide range of application in cell image analysis, the authors present in [Carpenter, *et al.*, 2006] the first open-source system designed for flexible, high-throughput cell image analysis, CellProfiler: a tool able to analyse a variety of biological samples.

II.4. Discussions

Beside a rough description of each method, a useful statistic and discussions about the frequency of the most used image processing methods in the problem of microscopic image segmentation is presented [Smochina, *et al.*, 2011e]. This analysis is helpful for a better use of existing methods, for improving their performance as well as for designing new ones. Table II.1 shows the most important image processing methods found in the studied papers and Table II.2 shows some criteria used for different tasks, e.g., merging, splitting, classifying, learning, feature extraction, etc.

| Image processing methods | Paper(s) |
|---|--|
| Threshold | [Bamford and Lovell, 1998], [Solorzano, <i>et al.</i> , 1999], [Cong and Parvin, 2000], [Boland and Murphy, 2001], [Malpica and de Solorzano, 2002], [Hu, <i>et al.</i> , 2004], [Wahlby, <i>et al.</i> , 2004], [Naik, <i>et al.</i> , 2007], [Wang, <i>et al.</i> , 2008], [Bai, <i>et al.</i> , 2009], [Coelho, <i>et al.</i> , 2009], [Dalle, <i>et al.</i> , 2009], [Russell, <i>et al.</i> , 2009], [Ta, <i>et al.</i> , 2009], [Zhou, <i>et al.</i> , 2009], [Jeong, <i>et al.</i> , 2009], [Madhloom, <i>et al.</i> , 2010], [Wei, <i>et al.</i> , 2011] |
| Watershed | [Soille, 2001], [Malpica and de Solorzano, 2002], [Wahlby, <i>et al.</i> , 2004], [Nilsson and Heyden, 2005], [Yang, <i>et al.</i> , 2005], [Yang, <i>et al.</i> , 2006], [Lebrun, <i>et al.</i> , 2007], [Angulo, 2008], [Cheng and Rajapakse, 2009], [Coelho, <i>et al.</i> , 2009], [Jeong, <i>et al.</i> , 2009], [Ta, <i>et al.</i> , 2009], [Zhou, <i>et al.</i> , 2009], [Boucheron, <i>et al.</i> , 2010], [Roshni and Raju, 2011] |
| Gradient | [Solorzano, <i>et al.</i> , 1999], [Wahlby, <i>et al.</i> , 2004], [Nilsson and Heyden, 2005], [Yang, <i>et al.</i> , 2005], [Angulo, 2008], [Wang, <i>et al.</i> , 2008], [Coelho, <i>et al.</i> , 2009], [Danek, <i>et al.</i> , 2009], [Jeong, <i>et al.</i> , 2009], [Ta, <i>et al.</i> , 2009], [Roshni and Raju, 2011] |
| Active contours (level sets and snakes) | [Bamford and Lovell, 1998], [Malpica and de Solorzano, 2002], [Hu, <i>et al.</i> , 2004], [Nilsson and Heyden, 2005], [Yang, <i>et al.</i> , 2005], [Naik, <i>et al.</i> , 2007], [Dzyubachyk, <i>et al.</i> , 2008], [Naik, <i>et al.</i> , 2008], [Cheng and Rajapakse, 2009], [Srinivasa, <i>et al.</i> , 2009], [Mosaliganti, <i>et al.</i> , 2009] |
| Morphological filtering | [Solorzano, <i>et al.</i> , 1999], [Nedzved, <i>et al.</i> , 2000], [Hu, <i>et al.</i> , 2004], [Lebrun, <i>et al.</i> , 2007], [Angulo, 2008], [Bai, <i>et al.</i> , 2009], [Dalle, <i>et al.</i> , 2009] |
| Multiresolution approach | [Chen and Lee, 1997], [Tolba, <i>et al.</i> , 2003], [Begelman, <i>et al.</i> , 2004], [Colantonio, <i>et al.</i> , 2007], [Srinivasa, <i>et al.</i> , 2009], [Roshni and Raju, 2011] |

| | |
|---|---|
| Model fitting/approximation (ellipsoidal, hyperquadric, polynomial, circle) | [Cong and Parvin, 2000], [Begelrnan, <i>et al.</i> , 2004], [Angulo, 2008], [Bai, <i>et al.</i> , 2009], [Gunduz-Demir, <i>et al.</i> , 2010] |
| Artificial neural network | [Kononenko, 2001], [Boland and Murphy, 2001], [Velliste and Murphy, 2002], [Colantonio, <i>et al.</i> , 2007], [Meftah, <i>et al.</i> , 2010] |
| Region growing | [Wu, <i>et al.</i> , 2005], [Srinivasa, <i>et al.</i> , 2009], [Gunduz-Demir, <i>et al.</i> , 2010], [Roshni and Raju, 2011] |
| Bayesian classifier | [Chen and Lee, 1997], [Kononenko, 2001], [Naik, <i>et al.</i> , 2007], [Naik, <i>et al.</i> , 2008] |
| Gaussian filter | [Solorzano, <i>et al.</i> , 1999], [Wahlby, <i>et al.</i> , 2004], [Lebrun, <i>et al.</i> , 2007] |
| Concavity points | [Cong and Parvin, 2000], [Wahlby, <i>et al.</i> , 2004], [Bai, <i>et al.</i> , 2009] |
| Markov model | [Chen and Lee, 1997], [Zhou, <i>et al.</i> , 2009], [Yang and Choe, 2009] |
| Support vector machine | [Naik, <i>et al.</i> , 2007], [Lebrun, <i>et al.</i> , 2007], [Wang, <i>et al.</i> , 2008] |
| Image enhancement | [Ta, <i>et al.</i> , 2009], [Dalle, <i>et al.</i> , 2009], [Madhloom, <i>et al.</i> , 2010] |
| K-means clustering | [Begelrnan, <i>et al.</i> , 2004], [Farjam, <i>et al.</i> , 2007] |
| Fuzzy c-means | [Chen and Lee, 1997], [Colantonio, <i>et al.</i> , 2007] |
| Graph representation | [Ta, <i>et al.</i> , 2009], [Gunduz-Demir, <i>et al.</i> , 2010] |
| Graph-cut | [Danek, <i>et al.</i> , 2009], [Yang and Choe, 2009] |
| Mean-shift | [Yang, <i>et al.</i> , 2005], [Yang, <i>et al.</i> , 2006] |
| Template matching | [Wahlby, <i>et al.</i> , 2004], [Naik, <i>et al.</i> , 2008] |
| Principal component analysis | [Wei, <i>et al.</i> , 2011] |
| Minimum filtering | [Madhloom, <i>et al.</i> , 2010] |
| B-spline | [Wang, <i>et al.</i> , 2008] |
| Particle segmentation | [Wang, <i>et al.</i> , 2008] |
| Quad-tree technique | [Chen, <i>et al.</i> , 2008] |
| Cross-correlation | [Begelrnan, <i>et al.</i> , 2004] |
| Bayesian network | [Jeong, <i>et al.</i> , 2009] |
| Fuzzy logic | [Begelrnan, <i>et al.</i> , 2004] |
| Variance filter | [Farjam, <i>et al.</i> , 2007] |
| Median filtering | [Solorzano, <i>et al.</i> , 1999] |

Table II.1 Image processing methods mostly used in microscopic images segmentation [Smochina, *et al.*, 2011e].

| Feature(s) | Paper(s) |
|--|---|
| area, perimeter, circularity | [Begelrnan, <i>et al.</i> , 2004], [Nilsson and Heyden, 2005], [Naik, <i>et al.</i> , 2007], [Coelho, <i>et al.</i> , 2009], [Naik, <i>et al.</i> , 2008], [Ta, <i>et al.</i> , 2009] |
| compactness | [Nilsson and Heyden, 2005], [Naik, <i>et al.</i> , 2007], [Naik, <i>et al.</i> , 2008], [Zhou, <i>et al.</i> , 2009], [Jeong, <i>et al.</i> , 2009] |
| shape, size and location | [Bamford and Lovell, 1998], [Yang, <i>et al.</i> , 2006], [Naik, <i>et al.</i> , 2008], [Danek, <i>et al.</i> , 2009] |
| convexity/convex hull | [Begelrnan, <i>et al.</i> , 2004], [Wahlby, <i>et al.</i> , 2004], [Coelho, <i>et al.</i> , 2009] |
| concavity, zero crossing | [Begelrnan, <i>et al.</i> , 2004], [Wahlby, <i>et al.</i> , 2004], [Boucheron, <i>et al.</i> , 2010] |
| smoothness | [Naik, <i>et al.</i> , 2007], [Naik, <i>et al.</i> , 2008], [Jeong, <i>et al.</i> , 2009] |
| variance | [Nedzved, <i>et al.</i> , 2000], [Nilsson and Heyden, 2005], [Naik, <i>et al.</i> , 2007] |
| average | [Nedzved, <i>et al.</i> , 2000], [Colantonio, <i>et al.</i> , 2007] |
| gradient norm, radial gradient | [Wahlby, <i>et al.</i> , 2004], [Colantonio, <i>et al.</i> , 2007] |
| roundness | [Farjam, <i>et al.</i> , 2007], [Coelho, <i>et al.</i> , 2009] |
| standard deviation | [Naik, <i>et al.</i> , 2007] |
| eccentricity, semi-major and -minor axes | [Coelho, <i>et al.</i> , 2009] |
| probability distribution function | [Zhou, <i>et al.</i> , 2009] |
| roughness | [Farjam, <i>et al.</i> , 2007] |
| moments | [Jeong, <i>et al.</i> , 2009] |

Table II.2 Features used for different tasks (merging, splitting, classifying, learning, feature extraction, etc) [Smochina, *et al.*, 2011e].

The thresholding (36% of the studied papers) and the watershed (30% of the studied papers) are the most used methods in processing the microscopic images from the considered papers. As pointed out in [Malpica and de Solorzano, 2002], the most widely spread segmentation method is grey level thresholding. The proposed techniques use different thresholding methods (global or adaptive) in different phase of the segmentation technique. For instance in [Cong and Parvin, 2000] it is used at the beginning for background detection, while in [Wang, *et al.*, 2008] it segments the results of the particle algorithm. The watershed diversity is given by the data used for seeds creation (original image [Angulo, 2008], gradient image [Wahlby, *et al.*, 2004] or blurred image [Coelho, *et al.*, 2009]) and by the application domain (inverse distance transform [Ta, *et al.*, 2009], gradient image, H-minima transform [Angulo, 2008]).

Beside the simple and classical methods (e.g. threshold-based, histogram characteristics, watershed), the active contours (level sets, snakes) proved to be an important technique able to provide satisfactory results [Malpica and de Solorzano, 2002]. The biggest problem in using the active contours is the initialization phase. In [Dzyubachyk, *et al.*, 2008] new approaches for algorithm initialization are proposed, but this remains a challenging problem which makes this method not suitable for many situations in which proper automatic initialization can't be achieved.

In many fields the ANN and SVM give good results only if the proper features are used. In microscopic images there are many attempts to extract the nuclear and the tissue components using different types of features; e.g. in [Boland and Murphy, 2001] a consistent group of features have been computed for protein localizations patterns. Since in microscopic field the objects of interest present a high variability of content, size, intensity distribution, position, organization, shape, it is hard to extract a suitable set of features which cover all possible situations. This step is critical and is the main reason in not using this approach on many images.

Many researches include *a priori* geometrical knowledge for the interest objects. This is the reason way many recent papers [Cloppet and Boucher, 2010], [Bai, *et al.*, 2009], [Jung and Kim, 2010] use customized shape model fitting (e.g. ellipse, circle) such that each object has a fitted model. Also particular points like the concave points from object boundaries are used in this fitting process or for objects splitting.

An interesting direction which seems to give successful results in semantic segmentation is the usage of the high-level knowledge like objects interaction or organizational properties [Smochina, *et al.*, 2011e]. Without considering the global relations between objects of interest, the low level cues will not be able to separate the regions having a particular meaning. Many approaches [Ta, *et al.*, 2009], [Gunduz-Demir, *et al.*, 2010] try to abstract the content of an image using graphs and continue the analysis process by applying different operations on these graphs. The techniques are similar with the one described in [Gunduz-Demir, *et al.*, 2010]: the image is pre-processed to extract the objects primitive (e.g. nucleus, lumen, and stroma); based on the relationship between them, a graph is build and is further used. This abstractization offers advantages because only the important components are considered and the not-useful details are ignored. In this way, the segmentation technique can tolerate the artefacts and variances from images.

Another technique used for the same reason is the multiresolution representation. In a coarse-to-fine approach only the important information is kept and the unnecessary details are removed. The role of local information (pixel grey values or gradient) is very important but not sufficient; also global information like the object's size and relation with the other object types must be used.

Table II.2 shows the criteria used for different tasks in the segmentation process like merging, splitting, classifying, learning, feature extraction, etc. The most used criteria, i.e. area, perimeter, circularity, compactness, shape, size, location, convexity, concavity are the results of using *a priori* knowledge about geometrical properties for the objects of interest.

II.5. Detailed segmentation methods

Several segmentation methods used further in the proposed techniques (IV and V) are described in more details in this section.

II.5.1. Region growing

Region growing (RG) is one of the simplest approaches from image segmentation: neighbouring pixels are grouped together to form a segmented region. The basic approach is to start from a set of seed points or regions and appending to each one the neighbouring pixels that satisfy a predefined criterion. This criterion usually refers to the colour/intensities similarity and depends on the problem and on the type of the image.

The seed creation function can provide more than one seed per image. If regions which must be detected using the RG are separated by other region types, a seed must be set for each region. In case that *a priori* information is available, the seed creation function should use it in order to provide suitable seeds for fast growing and accurate results.

The seed growing is an iterative process. At each step, the neighbouring pixels of the seed (obtained in the previous steps) are marked as seed if and only if their grey values satisfy a predefined criterion. The used criterion refers to the similarity between the values of the pixels marked as seed in previous iterations and the value of the candidate one. In the version used in the implementations from sections IV and V, the grey value of the candidate pixel is compared only with the mean value of the marked pixels from a close neighbourhood, i.e., a circle with the centre given by the candidate pixel and certain radius. A candidate pixel is marked as seed pixels if and only if the difference between its grey value and the mean value of its neighbourhood is smaller than a certain value thr_{grow} .

II.5.2. Watershed

Compared to RG method the watershed approach works per intensity layer instead of per neighbour layer. It includes topographic and hydrology concepts and is based on visualizing the grey-scale image as an altitude surface in which pixels with high intensities correspond to ridge points and those with lower intensities correspond to valley points [Pratt, 2001]. By rainfall or flooding [Pratt, 2001] this “topographic” interpretation [Gonzalez and Woods, 1992], the catchment basins or watershed (i.e., the accumulation of water in the vicinity of a local minimum) and the watershed lines (i.e., the ridges that surround a valley region) are obtained.

If watershed segmentation is applied directly to the image, it will most likely result in over-segmentation [Lopez, *et al.*, 1999]. This is way the image is carefully pre-processed before applying the watershed by imposing proper seeds which indicate where the water should accumulate. The seeds can be provided by other methods or by the extended minima transform.

The extended minima transform [Soille, 2001] is applied in order to simplify the intensity image by connecting regions of pixels with the intensity smaller than a value $hmin$, whose external boundary pixels all have a value greater than $hmin$.

II.5.3. Anisotropic diffusion

The basic idea of anisotropic filtering is to smooth the intensity image according to the local properties of the image. This nonlinear diffusion method allows anisotropic smoothing mainly along one preferred direction (along the boundaries) reducing the diffusivity over the edges areas [Weickert, 1998], [Schar and Weickert, 2000]. This process is given by an equation of type:

$$\frac{\partial I}{\partial t} = \nabla \cdot (D \cdot \nabla I), \quad D = \begin{pmatrix} a & b \\ c & d \end{pmatrix} \quad (\text{II.1})$$

where I is the evolving image, t denotes the diffusion time, ∇ denotes the gradient operator and D is the diffusion tensor of the coherence-enhancing process. Let Υ denotes the anisotropic diffusion filtering.

The preferred local orientations are obtained by computing the eigenvectors (v_1 and v_2) of the structure tensor ('second-moment matrix') J_ρ

$$J_\rho(\nabla I_\sigma) = G_\rho * (\nabla I_\sigma \cdot \nabla I_\sigma^T) = \begin{pmatrix} J_{11} & J_{12} \\ J_{21} & J_{22} \end{pmatrix} \quad (\text{II.2})$$

where G_ρ denotes a Gaussian with standard deviation ρ , I_σ is the result of the convolution between the image I and a Gaussian G_σ and "*" denotes the convolution operation.

The local contrast along these directions is given by the corresponding eigenvalues (μ_1 and μ_2). For instance, if $\mu_1 \gg \mu_2$ then the eigenvector v_1 indicates the orientation with the highest grey value fluctuations and v_2 gives the preferred blur orientation, i.e. the coherence direction. The diffusion tensor D of the coherence-enhancing diffusion uses the same eigenvectors as the structure tensor J_ρ but its eigenvalues λ_1, λ_2 are given by [Schar and Weickert, 2000]:

$$\lambda_1 = c_1$$

$$\lambda_2 = \begin{cases} c_1, & \text{if } \mu_1 = \mu_2 \\ c_1 + (1 - c_1)e^{\frac{-c_2}{(\mu_1 - \mu_2)^2}}, & \text{else} \end{cases} \quad (\text{II.3})$$

where $0 < c_1 < 1$ and $c_2 > 0$. Considering that the normalized first eigenvector can be written as $\begin{pmatrix} \cos \alpha \\ \sin \alpha \end{pmatrix}$, the entries of D are computed as follows [Schar and Weickert, 2000]:

$$\begin{cases} a = \lambda_1 \cos^2 \alpha + \lambda_2 \sin^2 \alpha \\ b = (\lambda_1 - \lambda_2) \sin \alpha \cos \alpha \\ c = \lambda_1 \sin^2 \alpha + \lambda_2 \cos^2 \alpha \end{cases} \quad (\text{II.4})$$

The nonlinear anisotropic diffusion filtering is mainly used to qualitatively improve the images and even for enhancing the edges but preserving in the same time the details and is based on nonlinear evolution partial differential equations. The anisotropic diffusion is currently one of the most powerful noise reduction techniques in the field of computer vision [Weickert, 1998].

II.5.4. Cross-correlation

Cross-correlation is a standard method of estimating the degree of similarity between two signals and it is often used in feature extraction [Gonzalez and Woods, 1992], [Brunelli and Poggio, 1993]. The normalized cross-correlation between the image I and the template t is defined by [Lewis, 1995]:

$$\gamma(u, v) = \frac{\sum_{x,y} [I(x, y) - \overline{I_{u,v}}] [t(x - u, y - v) - \bar{t}]}{\sqrt{\sum_{x,y} [I(x, y) - \overline{I_{u,v}}]^2 \sum_{x,y} [t(x - u, y - v) - \bar{t}]^2}} \quad (\text{II.5})$$

where \bar{t} is the mean of the template and $\overline{I_{u,v}}$ is the mean of the pixels from I overlapped by under the template.

The value $\gamma(u, v)$ from Eq.II.5 represents the correlation coefficient at the position (u, v) . These coefficients have high values for the pixels situated in a region with high similarity with the used template. In case of dissimilarity, the coefficients have lower or even negative values. Since the normalized cross-correlation is not invariant with respect to imaging scale and rotation, the used template should be carefully chosen.

II.5.5. Maximally stable extremal region

The maximally stable extremal region (MSER) algorithm [Matas, *et al.*, 2002] checks all thresholds and the connected components are extracted judging their area change. The MSERs are regions that are either darker (MSER-) or brighter (MSER+) than their surroundings and are stable according to a stability criterion across a range of thresholds on the intensity function.

Each threshold application on the grey-scale image I gives the binary image B_t . The regions in the binary images became smaller by ranging the threshold from 1 to 256 (for 8 bit images). Let $\Psi(R_i^t)$ defines the stability based on the area change of region R_i^t from the image B_t obtained with threshold t :

$$\Psi(R_i^t) = \frac{|R_i^{t-\Delta}| - |R_i^{t+\Delta}|}{|R_i^t|} \quad (\text{II.6})$$

where Δ is the stability range parameter and $|\cdot|$ gives the region area. The regions $R_i^{t-\Delta}$ and $R_i^{t+\Delta}$ are the ascendant and the descendent regions of R_i^t obtained by decreasing respectively increasing the threshold level and $R_i^{t-\Delta} \supset R_i^t \supset R_i^{t+\Delta}$. A region R_i^t is MSER+ if it has the following properties:

- extremal, i.e. all pixels inside the connected region are strictly brighter than the surrounding ones;
- stable, i.e. its area changes only slightly with the change of the threshold t (across $2\Delta + 1$ thresholds);
- maximally stable, i.e. $\Psi(R_i^t)$ has a local minimum at t .

The advantage of using the MSER is given by the lack of a global or adaptive threshold. All thresholds are tested and the stability of the connected components evaluated. If multiple stable thresholds exist then a set of nested regions is obtained per object. In this case the output of the MSER detector is not a binary image.

II.6. Conclusions

Since there is no universal approach for obtaining accurate image segmentations, almost all techniques combine the two main approaches: region-based schemes and edge based schemes. This is why a classification based on the criterion used by each segmentation technique is almost impossible. Instead, a list of the most used methods and how they are usually combined to achieve good segmentation results is helpful for a better use of the existing methods and for improving their performance, as well as for designing new ones.

In this chapter some representative studies in the field of microscopic image segmentation have been roughly described (II.2 and II.3) and some further used techniques (region growing, watershed, anisotropic diffusion, MSER) have been presented in more details (II.5). The studied techniques were grouped by the representative method or by the key approach which gives significant improved results, i.e., thresholding and watershed, concavity points, polygonal approximation and geometrical model fitting, active contours, graphs or multiresolution and clusters. Some techniques use only simple processing techniques but the majority combines methods without considering their complexity, e.g. threshold with particle algorithm [Wang, *et al.*, 2008] or fuzzy c-means algorithm with artificial neural network [Colantonio, *et al.*, 2007].

As a general tendency it can be concluded that the new techniques use two main directions which seem to provide stable and accurate segmentation results [Smochina, *et al.*, 2011e].

The first one tends to use the geometrical properties as *a priori* knowledge, i.e. different geometrical models fitting (ellipsoidal, hyperquadric, polynomial or circle).

When this is not possible due to weak boundaries, low inter-object contrast or high variability in shape and size, the second tendency based on objects features is considered; these features are used to train an ANN, a Bayesian networks or a SVM.

III. Segmentation evaluation methods

This chapter points out the importance of evaluation in the segmentation task and describes the concepts and the main classes of segmentation evaluation criteria. After a discussion about the existing problems of the proposed methods in the literature (III.2), a new quality measure is proposed for evaluating the performance of the segmentation algorithms (III.3). The proposed discrepancy method [Smochina, *et al.*, 2010a] is based on the comparison machine segmentation vs. ground-truth segmentation. This error measure uses the geodesic path between the segmented and the reference curve to eliminate the inconveniences that appear in the case of concave objects and adds a weighted shape fitting score to indicate the similarity between these two segmentations. The results are shown in III.4 and concluded in III.5.

III.1. Introduction

Image segmentation is one of the most critical tasks in automatic image analysis and an essential step of low-level vision. Because of its importance, a great variety of segmentation algorithms have been proposed in the last few decades but none of the developed algorithms is generally applicable [Zhang, 1996]. In general, each algorithm is specialised for a particular application. This is why it is indispensable to have a robust technique for evaluating the performance of these algorithms, to characterize and to highlight the situations in which the obtained results satisfy the requirements imposed by the field in which they are used. A rough idea about the publications of segmentation methods tendency can be found in [Zhang, 2006].

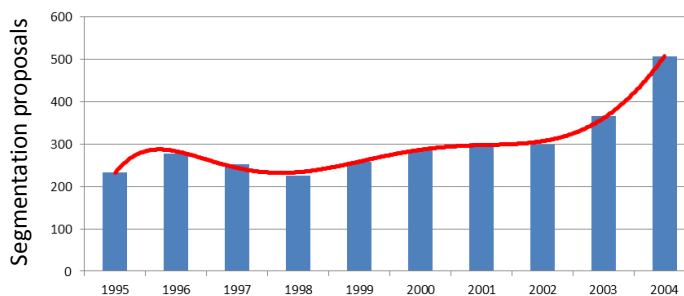


Fig.III.1 Number of records and the tendency of development in 1995-2004.

Performance evaluation is critical for all computer vision algorithms and up against segmentation, relatively fewer effort have been spent for building an evaluation method usable in any computer vision field [Zhang, 1996]. The great variety of segmentation

algorithms creates difficulties in evaluating the efficiency of a new developed algorithm [Chabrier, *et al.*, 2008].

The first extensive comprehensive study and classification of the evaluation criteria has been published in [Zhang, 1996]. The author analyses and compares the applicability of the existing methods and separates them as analytical and empirical methods [Zhang, 1996], [Zhang, 2001]:

- *Analytical methods* directly examine the principles and the properties (complexity, processing strategy, i.e. parallel, sequential, iterative or mixed, etc.) of the segmentation algorithm without applying the algorithm on images. As pointed out in [Zhang, 1996], the lack of general theory for the image segmentation task makes this approach inappropriate for many algorithms;
- *Empirical methods* determine the performance of an algorithm indirectly by judging the quality of the segmentation. These methods are split into two categories based on the criterion type used to compare the machine segmented image and the “ideal” segmentation:
 - *Unsupervised methods* (goodness methods) consist in the computation of various statistics upon the segmentation result in order to quantify the quality of the algorithm. These goodness methods are mostly based on intra-region uniformity, inter-region contrast and region shape. The quality score is based solely on the segmented image and its great advantage is the lack of comparison against a manually-segmented reference image;
 - *Supervised methods* count the differences between a machine segmented image and the reference segmentation provided by an expert. These methods aim to determine how far the segmented image is from the ground-truth image [Zhang, 2001].

A general scheme of the segmentation and evaluation processes is presented in Fig.III.2.

There are many reviews and comparative studies of the proposed methods ([Zhang, 1996], [Zhang, 1997], [Zhang, 2001], [Jiang, *et al.*, 2006], [Chabrier, *et al.*, 2004], [Chabrier, *et al.*, 2006], [Chabrier, *et al.*, 2008]) in which authors try to describe and to highlight the pros and cons of these criteria. It is generally accepted [Zhang, 1996] that the supervised methods are more effective than the unsupervised methods but they have a big disadvantage: the need of reference segmentations done by the experts. The supervised evaluation methods are further analysed since they are able to concretely and accurately evaluate the segmentations.

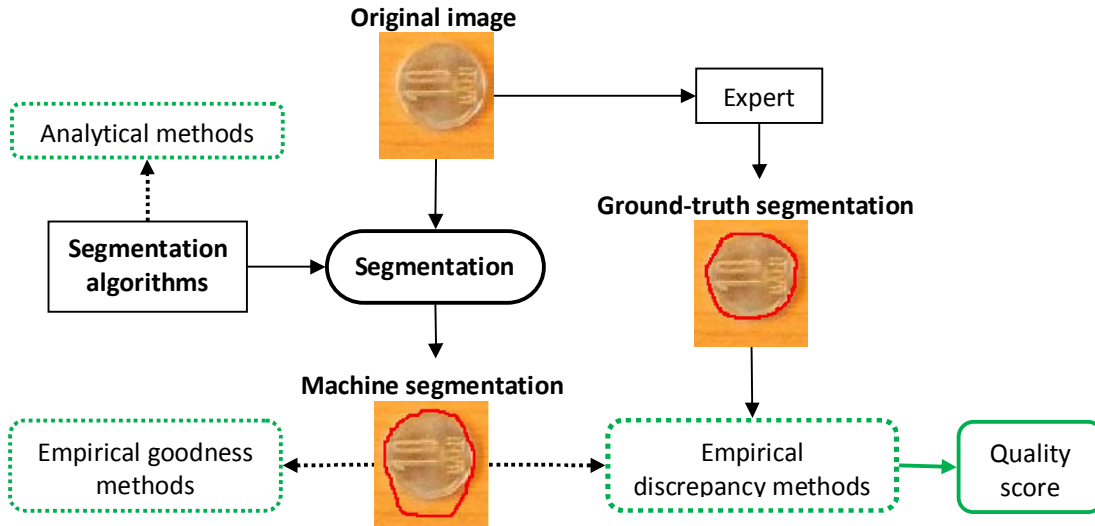


Fig.III.2. The classification of the segmentation evaluation methods.

III.1.1. Supervised evaluation criteria

In the first comprehensive study of evaluation criteria [Zhang, 1996], the discrepancy methods are grouped by the criterion used to highlight the difference between the machine segmentation and the gold-standard segmentation: discrepancy based on the number and the position of mis-segmented pixels, the number of objects in the image and the feature values of segmented objects.

Four types of regions can appear by comparing the machine and the reference segmentations [Bowyer, *et al.*, 2001], [Goumeidane, *et al.*, 2003]:

- True Positive (TP) regions which contain pixels of the reference object and the segmented object;
- False Positive (FP) regions contain pixels from the segmented object but not from the reference object;
- False Negative (FN) regions contain pixels from the reference object but not from the segmented object;
- True Negative (TN) regions contain pixels of the background from both segmented and reference images.

These four types of pixels are exemplified in Fig.III.3 using a synthetic object (green circle) and a possible segmentation (red diamond):

- the TP pixels belong both to the circle and diamond;
- the TN pixels belong to the common background;

- the FP pixels belong only to the red diamond (the segmentation); also referred as over-segmented pixels;
- the FN pixels belong only to the green circle (the reference); also referred as under-segmented pixels.

The terms “segmented curve” and “reference curve” (ground-truth curve) are used to denote the boundaries of the regions segmented by the segmentation algorithm (i.e., the boundaries of the machine segmentation) and by the human expert (i.e., the boundaries of the ground-truth segmentation). In this context:

- the over-segmented curve points belong to the segmented curve and the boundaries of FP regions (e.g., points from segments [BC] and [CD] in Fig.III.3);
- the under-segmented curve points belong to the reference curve and the boundaries of FN regions (e.g., points from circular arc segment AB in Fig.III.3).

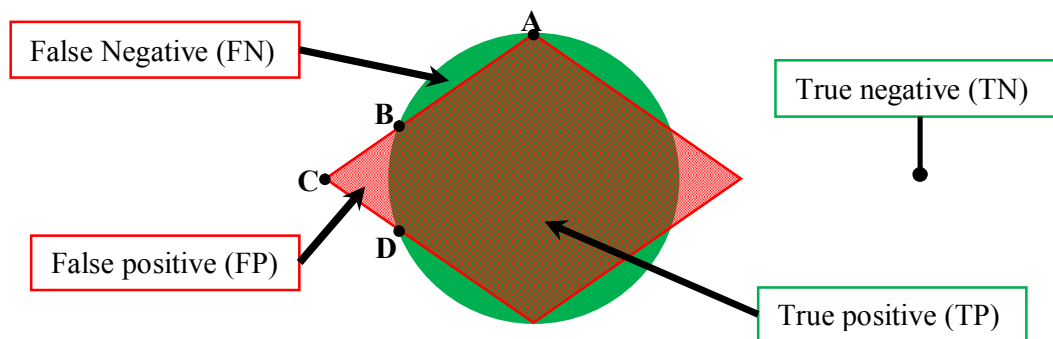


Fig.III.3 The round green object is miss-segmented as a diamond (red).

The newly proposed methods treat also additional problems from segmentation evaluation beside those considered in [Zhang, 1996]. In [Chalana and Kim, 1997] the medical image segmentation algorithms are evaluated. A procedure to compute the gold-standard segmentation from multiple reference segmentation is proposed. This is useful when more than one human expert exists and an average curve is needed.

A hybrid method of empirical discrepancy (pixel-by-pixel objective discrepancy) and empirical goodness is described in [Roman-Roldan, *et al.*, 2001]. The authors claim that this is the type of measure best suited to the general problem of segmentation evaluation. Still, the simple and intuitive mathematical expression should be applied only in cases where the machine segmentation edges are pretty close to the theoretical ones.

The edge detectors are evaluated in [Bowyer, *et al.*, 2001] using the receiver operating characteristic (ROC) curves. Each parameter setting generates a point in the ROC space, i.e. the point (TP, FP) and the ideal one is (TP, FP) = (0, 0). Rules for interpreting the meaning of different points on the ROC curves are presented.

The performance evaluation of region-based segmentation algorithms is approached in [Pinheiro and Facon, 2005]. A general metric qualifies the segmentation method using four “scenarios” which occur in a segmentation process (correct-, over-, under- and mis-segmentation). The results showed that the new measure is more sensitive than the traditional discrepancy evaluation criteria.

The same problem of evaluating the region-based segmentation algorithms is considered in [Jiang, *et al.*, 2006] as one of data clustering. Many interesting performance measures (also metrics) have been obtained by using measures for comparing clusters developed in statistics and machine learning.

A very interesting approach is described in [Cavallaro, *et al.*, 2002]. If in [Roman-Roldan, *et al.*, 2001] the empirical discrepancy is combined with empirical goodness, here the authors add beside the discrepancy measure also the visual relevance of the human perception, i.e. the surprise effect and the fatigue effect.

The method from [Everingham, *et al.*, 2002] uses the Pareto front and different cost functions like pixel- or object-wise potential accuracy and region-wise information content.

The problem of multiple objects in an image is addressed in [Polak, *et al.*, 2009]. The object-level consistency error (OCE) is proposed and takes into account the existence, size, shape, and position of each object and penalizes both over-segmentation and under-segmentation.

In pattern recognition the following measures are widely used to characterize the agreement between the region boundaries of two segmentations: precision (P), recall (R) and accuracy (A) [Rijsbergen, 1979]. They are sensitive to over- and under-segmentation and are defined as follows [Rijsbergen, 1979]:

$$\begin{aligned}
 P &= \frac{TP}{TP + FP} \\
 R &= \frac{TP}{TP + FN} \\
 A &= \frac{TP + TN}{TP + TN + FP + FN}
 \end{aligned}
 \tag{III.1}$$

In information retrieval, the precision represents the fraction of correctly retrieved instances, while recall is the fraction of relevant instances that are retrieved. In pattern recognition, a low recall and high precision indicate an over segmentation tendency.

Beside these measures, two ratios are also used [Smochina, *et al.*, 2011a]: the true positive ratio (TPR) and the mis-segmented ratio (MSR). The TPR represents the correctly identified regions versus the total number of regions from the ground-truth image. The MSR represents the number of mis-segmented regions versus the total number of automatically segmented regions.

III.1.2. Considered criteria

The existing evaluation criteria have many different approaches. The most important categories are those based on the number and the position of mis-segmented pixels, the number of the objects in the image, the features values of the segmented objects and miscellaneous quantities [Zhang, 1996].

Among all the methods proposed in the literature, four evaluation criteria (also used in [Chabrier, *et al.*, 2004], [Chabrier, *et al.*, 2008]) were analysed and tested on a set of trivial images that contain coins and synthetic images:

- Pratt's Figure of Merit (FOM) [Goumeidane, *et al.*, 2003]:

$$\text{FOM} = \frac{1}{\max\{\text{card}(R), \text{card}(S)\}} \sum_{i=1}^{\text{card}(S)} \frac{1}{1 + \alpha \cdot d_E^2(i, S)} \quad (\text{III.2})$$

where R and S represent the reference and the segmented curves, $\text{card}(\cdot)$ represents the cardinality of a set, $d_E(i, S)$ denotes the Euclidean distance between the i th detected curve point and the curve S and α is a scaling parameter.

- Hausdorff distance [Beauchemin, *et al.*, 1998] defines the distance between two curves A and B:

$$d_H(A, B) = \max\left(\max_{a \in A} d_E(a, B), \max_{b \in B} d_E(b, A)\right) \quad (\text{III.3})$$

where $d_E(a, B) = \min_{b \in B} \|a - b\|$ represents the distance from the point a (belonging to curve A) to the closest point on curve B and $d_E(a, b) = \|a - b\|$ is the Euclidean distance. In the segmentation evaluation context, the curves A and B could refer to the segmented and the reference curve.

- Odet's criteria (ODI, UDI) [Odet, *et al.*, 2002] for over- and under-segmented pixels:

$$\begin{aligned} \text{ODI} &= \frac{1}{N_o} \sum_{i=1}^{N_o} \left(\frac{d_o(i)}{d_{TH}} \right)^n \\ \text{UDI} &= \frac{1}{N_u} \sum_{i=1}^{N_u} \left(\frac{d_u(i)}{d_{TH}} \right)^n \end{aligned} \quad (\text{III.4})$$

where N_o and N_u are the number of over- respectively under- detected curve points, $d_o(i)$ is the distance between the point i of the segmented curve and the reference curve, $d_u(i)$ is

the distance between a non-detected point i of the reference curve and the segmented curve. The saturation distance d_{TH} indicates that the segmented points far away from the reference curve (distance bigger than d_{TH}) should receive the same error; the discrepancy is individually computed for the points on a distance smaller than d_{TH} (closer to the reference curve).

For the FOM criterion the higher values indicate a better segmentation result, while for the Hausdorff, ODI and UDI criteria the lower values are better.

III.2. Discussions about the existing problems

The surveys of the proposed criteria have revealed the shortcoming of currently developed measures and point out their critical deficiencies [Roman-Roldan, *et al.*, 2001]. Most of the methods use the distance between the segmented and the reference curves. They compute this distance by extending the Euclidean distance between two points. This approach gives satisfactory results for convex objects but for complex concave shapes the Euclidean-based distance might provide inconsistent results.

Let's consider a synthetic object with a shape similar to letter C (green object in Fig.III.4) and two possible segmentations: S1 and S2. In this situation, the considered approaches will compute erroneously the distance to the reference curve by tracking the distance towards the wrong side of the object, through the segmented object body.

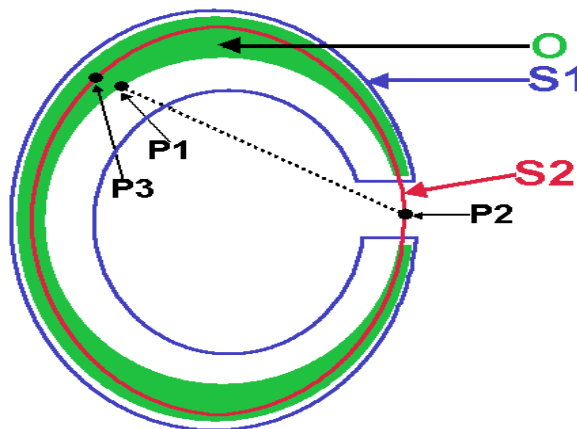


Fig.III.4 Object O (green object with shape similar to letter C) is mis-segmented as S1 and S2. Point P1 is located on the contour of the object O and the points P2 and P3 on the segmented curve S2.

[Smochina, *et al.*, 2010a]

If the Euclidian distance between the segmented and reference curves are used for computing the quality score, the segmentations S1 and S2 produce the same score when compared against ground-truth object O, although S1 is clearly a better approximate of the

object than S2. This is happening because the shortest path from point P1 to the segmentation S2 is going through object O. The closest point from S2 to point P1 should be P2, not P3.

To solve the problems pointed out in the previous situations, a new supervised evaluation method is proposed in III.3.

III.3. Discrepancy measure based on geodesic path and curves similarity

A new quality measure is proposed to evaluate the performance of segmentation algorithms [Smochina, *et al.*, 2010a]. This discrepancy method is based on the comparison: machine segmentation vs. ground-truth segmentation. The proposed error measure offers two main advantages compared to other quality measures.

The first one is the use of an alternative method in computing the distance from the segmented to the reference curve. This method takes into consideration the interior of the object and eliminates the inconveniences that appear in the case of concave objects.

The second improvement comes from adding a weighted shape fitting score. The quality score of the segmented curve is enhanced by a factor which indicates the similarity between these two segmentations.

III.3.1. Preliminaries

Let R represents the reference curve with N_R pixels and S represents the segmented curve with N_S pixels. The reference curve is obtained as an average of curves [Chalana and Kim, 1997] drawn by three human experts.

There are methods which offer two separate errors for the FP respectively FN regions, but this method doesn't make any difference between them, i.e., the error for each mis-segmented region (FP or FN) is computed in the same way. The final error is given by a weighted mean of these scores (Eq.III.9).

As an example, in Fig.III.7 the synthetic green object O is considered and the red closed curve is the border of a possible segmentation (segmented curve). The region $FN1$ with FN pixels and the two regions FPI and $FP2$ with FP pixels are obtained and scored independently in two phases. Firstly the error from the segmented (S) to the reference curve (R) is computed, and secondly the error from the reference to the segmented curve. The segmentation error for each fragment takes into consideration the maximum of the two scores, as they might be different (Eq.III.8). An overview scheme of the proposed technique is shown in Fig.III.5.

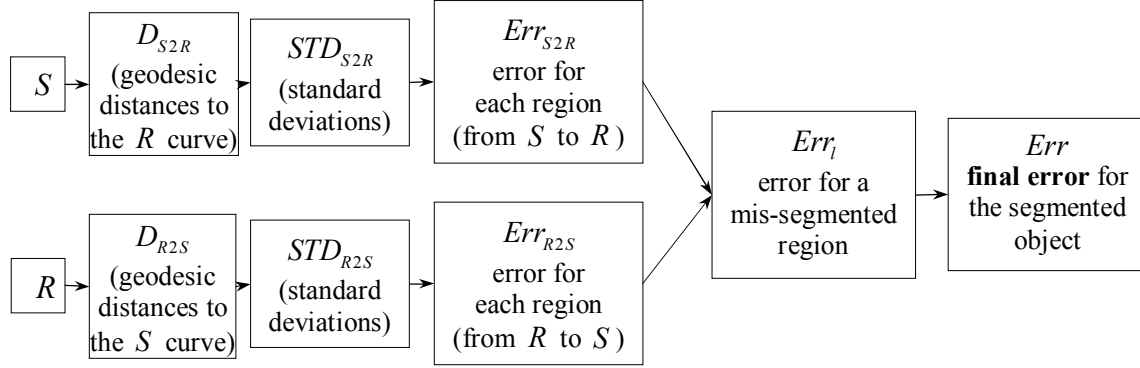


Fig.III.5. Overview scheme of the proposed evaluation technique.

III.3.2. Distance between segmentations curves

Most of the developed methods ([Pratt, *et al.*, 1978], [Dubuisson and Jain, 1994], [Cavallaro, *et al.*, 2002], [Odet, *et al.*, 2002], [Goumeidane, *et al.*, 2003]) use the Euclidean distance between a pixel of the segmented curve and the reference curve to penalize the segmentation. This gives good results for convex objects but might produce significant mistakes even for simple concave objects.

One of the first improvements in the score calculation is obtained by changing the manner of computing the distance between segmentations: full objects are considered and not only their boundaries. This Opaque Object Approach (OOA) tries to avoid measuring paths that go through the correctly segmented areas.

Only the mis-segmented regions (FP and FN) are considered while the TP and TN regions behave like opaque areas in the process of computing distances between the reference and segmented curves. The shortest path between pixels of the two curves is not allowed to pass through correct areas (TP or TN). This condition leads us to the geodesic path.

III.3.2.1. Geodesic path

Instead of computing the distance between pixels using the Euclidean distance, the geodesic path is used. The term geodesic refers in the geodesy to the shortest path between two points on the Earth's surface. In the discrete and computational geometry it is defined as the shortest path between points in a space.

In the particular case of segmentation evaluation, the space (2D discrete) is represented by the FP and FN pixels. Let's name it M . The number of connected components M_c , $i = \overline{1, n_c}$ in M is equal to the number of FP and FN regions, i.e., n_c . The geodesic path between two pixels x_a and x_b of a connected component M_c from M is the shortest path (minimal length) connecting x_a and x_b in M_c .

If $d_G(x_a, x_b) = \{p_1, p_2, \dots, p_n\}$ is a geodesic path between $x_a, x_b \in M_c$, then $p_i \in M_c$, $i = \overline{1, n}$ and its length n is minim. Note that p_i and p_{i+1} are connected neighbours for $i = \overline{1, n-1}$. The same concept received a more intuitive name in [Ling and Jacobs, 2007]: “inner distance”.

In Fig.III.3 the FP and FN regions are delimited by a portion of the reference curve (green) and a portion of the segmented curve (red). Since the distance is computed between pixels which belong to a certain curve portion, we impose that x_a and x_b belong to the boundary of a connected component ($x_a, x_b \in \partial M_c$), i.e., to one of the reference or segmented curve.

This approach solves the problem highlighted in Fig.III.6 where the closest point from the reference object (round blue object) to the point A from the segmented object (red arrow) is correctly computed by geodesic approach (green path AB) instead of the Euclidean distance AC.

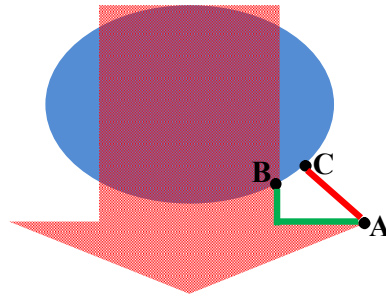


Fig.III.6 The round blue object is mis-segmented as a red arrow. The Euclidean distance between the point A and the blue object (red line AC) and the geodesic path (green path AB).

III.3.3. Curves similarity measure

The shape fidelity of the segmented object is very important in many industrial and research fields [Correia and Pereira, 2000]. The usual features like area, perimeter, bending energy, eccentricity or sphericity, make the criteria suitable only for simple objects.

The second proposed improvement in the score calculation, named Shape Fitting Error (SFE), includes a factor which indicates the degree of affinity between the segmented and the reference curves.

III.3.3.1. The error from the segmented to the reference curve

In the first phase, the error for each mis-segmented region (FN and FP) is computed starting from the points of the segmented curve S to the reference one R [Smochina, *et al.*, 2010a].

For each point $s_i \in S$, the shortest geodesic path d_i to the reference curve is computed as explained in III.3.2.1. Considering all pixels from the S curve, an array of distances D_{S2R} with length N_S is obtained. $D_{S2R}(i)$ represents the minimum geodesic distance to the points of the reference curve R . These values can be considered as forming signal which indicates the deviation of each segmented point to the reference curve, or “how far it is from the ideal position”.

This signal has small variations/noise caused by the ground-truth segmentations drawn by experts. This is eliminated by applying a low-pass filter (Gaussian filter with standard deviation 10) in the frequency domain after a Fourier transformation. After this filtration the signal will have only the lower frequencies, i.e., only the main changes of the values from the D_{S2R} vector.

Based on the array D_{S2R} , another array STD_{S2R} with the same length is created. The value $STD_{S2R}(i)$ of the i th point represents the standard deviation computed in a neighbourhood of ε pixels of point i from D_{S2R} . The $STD_{S2R}(i)$ is given by [Smochina, *et al.*, 2010a]:

$$STD_{S2R}(i) = \begin{cases} \text{std}\left(\left[D_{S2R}\left((N_S + i - \varepsilon) : N_S\right), D_{S2R}\left(1 : (i + \varepsilon)\right)\right]\right), & i \leq \varepsilon \\ \text{std}\left(D_{S2R}\left((i - \varepsilon) : (i + \varepsilon)\right)\right), & i \in (\varepsilon, N_S - \varepsilon) \\ \text{std}\left(\left[D_{S2R}\left((i - \varepsilon) : N_S\right), D_{S2R}\left(1 : (\varepsilon + i - N_S)\right)\right]\right), & i \geq N_S - \varepsilon \end{cases} \quad (\text{III.5})$$

where $\text{std}(D)$ is the standard deviation of the set of values D .

Each element of the vector STD_{S2R} indicates the degree of similarity between portions of these two curves. A high value of $STD_{S2R}(i)$ indicates that the neighbourhood of point i is in a portion of the segmented curve with strong deviation from the reference curve.

Considering this similarity indicator and the distances between pixels of these two curves, the following error for each region (from S to R) is proposed [Smochina, *et al.*, 2010a]:

$$Err_{S2R} = \frac{1}{N_S} \sum_{i=1}^{N_S} D_{S2R}(i) \cdot [1 + \eta \cdot STD_{S2R}(i)] \quad (\text{III.6})$$

This error is the sum of the errors of each pixel from the segmented curve divided by the number of pixels. The error for each pixel is given by the geodesic distance $D_{S2R}(i)$ to the ideal curve weighted by a factor $\varphi = 1 + \eta \cdot STD_{S2R}(i)$. This factor indicates the degree of affinity between the neighbourhood of the point i with the corresponding portion from the

reference curve. φ is 1 for a perfect similarity and grows according to the fluctuation of the curve segment.

Depending on the field in which this method is applied, the η parameter can be changed by giving different weights to the shape fidelity. η will receive a small value (e.g. 0.25, 0.1) for situations when the shape accuracy is not so important and values bigger than 1 when shape is of interest.

Different ways to weight the distance for one segmented pixel can be found in [Cavallaro, *et al.*, 2002] and [Mezaris, *et al.*, 2003]. In [Cavallaro, *et al.*, 2002] a logarithmic function is used for FP pixels and a linear function for FN pixels; in [Mezaris, *et al.*, 2003] two linear functions are used to weight both FP and FN pixels.

III.3.3.2. The error from the reference to the segmented curve

In the second phase the previously described process is repeated but considering the geodesic paths from the reference curve R to the segmented curve S .

In the obtained array D_{R2S} (length N_R), the $D_{R2S}(j)$ represents the minimum geodesic distance from the point $r_j \in R$ to the segmented curve S . In this case, the error for a region is given by (similar to Eq.III.6) [Smochina, *et al.*, 2010a]:

$$Err_{R2S} = \frac{1}{N_R} \sum_{j=1}^{N_R} D_{R2S}(j) \cdot [1 + \eta \cdot STD_{R2S}(j)] \quad (III.7)$$

III.3.4. Segmentation error

Since the two phases might provide different results, the error for a mis-segmented region is set using the maximum of these two errors Err_{S2R} and Err_{R2S} [Smochina, *et al.*, 2010a]:

$$Err_l = 1 - \frac{1}{1 + \kappa \cdot \max\{Err_{R2S}, Err_{S2R}\}} \quad (III.8)$$

where κ is a positive factor used to control the accuracy of the error scale. The error is 0 for a perfect segmentation and it grows asymptotically to 1 for worst segmentations.

The final error for the segmented object is given by a weighted mean of the errors obtained for each mis-segmented region [Smochina, *et al.*, 2010a]:

$$Err = \frac{\sum_{l=1}^{n_c} Err_l \cdot A_l}{\sum_{l=1}^{n_c} A_l} \quad (III.9)$$

where n_c is the number of mis-segmented regions, Err_l denotes the error for region l (Eq.III.8) and A_l the area of the region l .

III.3.5. Particular example

The modality of applying the new criterion is exemplified in details using a simple object O (green) and a possible segmentation S depicted as red in Fig.III.7.

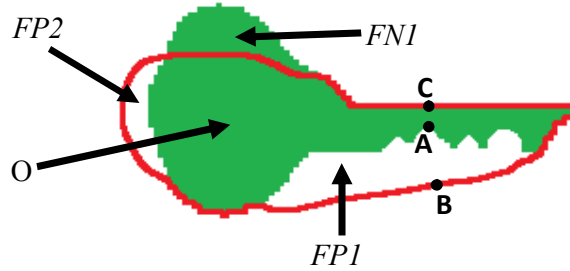


Fig.III.7 The intersection between the reference object O and the border of a segmentation S [Smochina, *et al.*, 2010a].

In Fig.III.7, region FNI contains false negative pixels, while regions $FP1$ and $FP2$ contain false positive pixels.

The point B is the closest point on the segmented curve to the point A (on the reference curve) and it is correctly computed using OOA described in III.3.2. Other methods ([Beauchemin, *et al.*, 1998], [Correia and Pereira, 2000], [Cavallaro, *et al.*, 2002], [Goumeidane, *et al.*, 2003]) find the point C, instead of B, because these methods use only the object contours without considering the interiors of the correctly segmented regions.

The arrays of the distances and the arrays of the standard deviations for regions $FP1$ and $FP2$ with are drawn in Fig.III.8.

For region $FP1$ the maximum error is obtained when computing the error from the reference curve to the segmented curve, i.e., Err_{R2S} . The array of distances D_{R2S} for region $FP1$ has 179 elements and is plotted in Fig.III.8a after applying the low-pass filter.

For region $FP2$ the maximum error is obtained when computing the error from the segmented curve to the reference curve, i.e., Err_{S2R} and the distances array with 80 elements is plotted in Fig.III.8c.

Each element of the standard deviations vector indicates the degree of similarity between portions of these two curves.

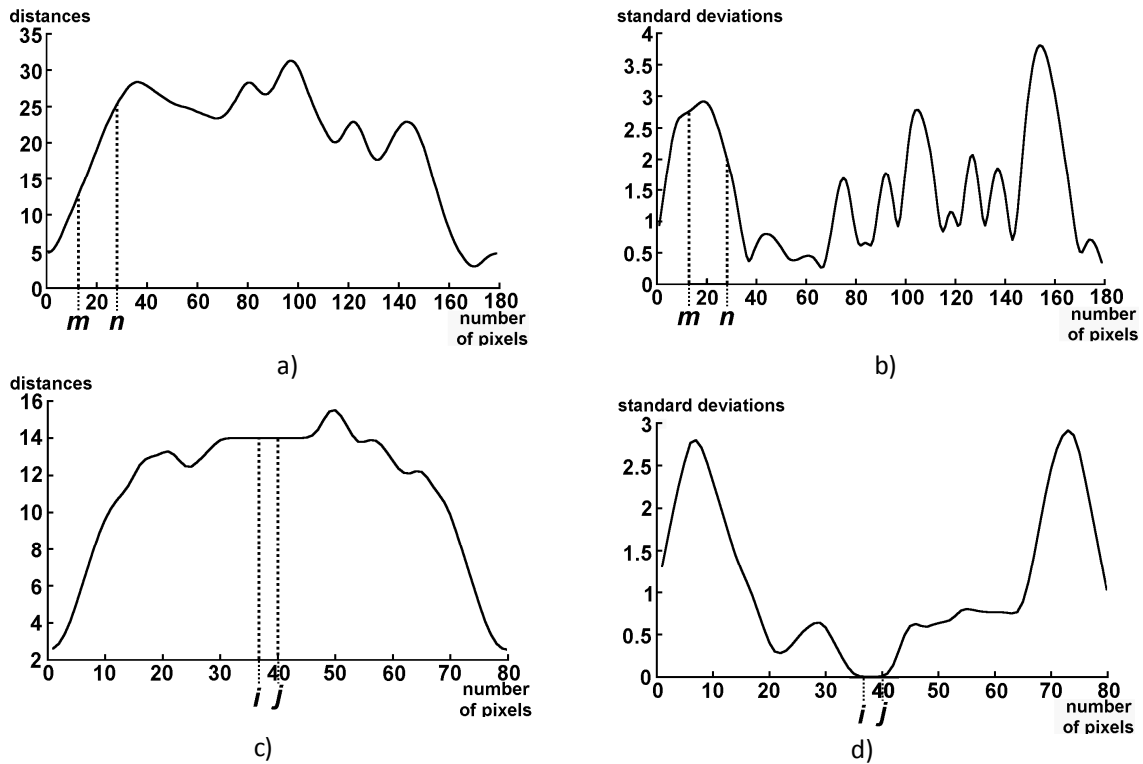


Fig.III.8 The distances arrays for the regions FP1 (a) and FP2 (c). The vectors of the standard deviations for the regions FP1 (b) and FP2 (d). [Smochina, *et al.*, 2010a]

For instance, the segmented pixels between indexes i and j of the region $FP2$ (Fig.III.8c) are in a portion of the segmented curve similar to the corresponding portion from the reference curve; the distances of these pixels will have a zero standard deviation (Fig.III.8d). In this case, the factor φ will be 1 and these pixels will receive only the error given by their distances to the correct positions.

On the contrary, the pixels between indexes m and n of the region $FP1$ (Fig.III.8a) are in a region where the reference and the segmented curves have few similarities. In this situation the error of these pixels will be given by their distances weighted by the factor φ bigger than 1 due to shape mismatch.

III.4. Results

Opaque Shape Fitting Error (OSFE) includes both proposed improvements: OOA (III.3.2) and SFE (III.3.3). We used real and synthetic images to illustrate its behaviour. Situations in which the segmented object includes a concave object can be found in different industrial (inspection systems, cell detection) and research fields. In these situations the distances are calculated correctly using the OOA method which considers also the interior of the objects. The OSFE method is tested on synthetic (III.4.1) and real (III.4.2) objects with different possible segmentations and the results are compared with the other considered criteria.

III.4.1. Synthetic test images

Fig.III.9 shows different segmentations (depicted as red) for the green concave object. The segmentations are evaluated using the proposed method OSFE and the considered ones: ODI, UDI, FOM and Hausdorff (Table III.1).

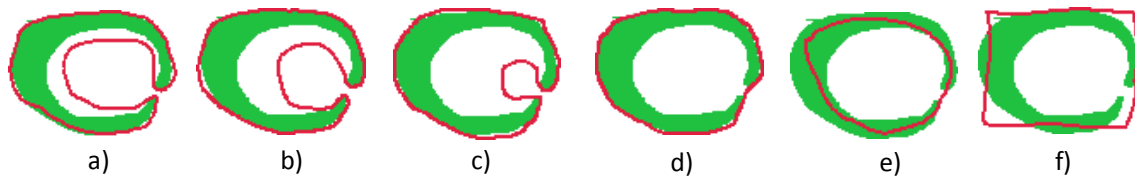


Fig.III.9 Different segmentations (with red) for the green synthetic object [Smochina, *et al.*, 2010a].

| Fig.III.9 | OSFE* $\eta = 1$ | ODI* | UDI* | FOM** | Hausdorff* |
|-----------|---------------------|--------|--------|---------|------------|
| a | 0.2310 | 0.3360 | 0.3605 | 21.778 | 12.2066 |
| b | 0.3958 | 0.4478 | 0.5778 | 24.1193 | 23.8537 |
| c | 0.6180 | 0.3875 | 0.5881 | 27.1516 | 24.0416 |
| d | 0.7131 | 0.1462 | 0.6160 | 34.675 | 20.2237 |
| e | 0.7666 | 0.3450 | 0.4578 | 41.2301 | 13.8924 |
| f | 0.8024 | 0.3955 | 0.6165 | 29.5016 | 18.0278 |

Table III.1 Evaluation results of the segmentations from Fig.III.9 [Smochina, *et al.*, 2010a].

We use * to indicate that the lower values are related to a good segmentation result, and ** to indicate that the higher values are related to a good segmentation result.

A major difference between the scores is visible when comparing results for Fig.III.9b and d. As a general opinion, b) is a better segmentation than d). ODI, FOM and Hausdorff wrongly indicate d) as better. UDI fails when comparing e) and c), wrongly preferring segmentation e). The proposed OSFE score correctly identifies the increasing order of

segmentation quality from a) (best) to f) (worst), while the other scores fail in ordering b), c), d) and e) segmentations.

The synthetic images from Fig.III.10 are used to illustrate the importance of the curves similarity measure. The green curve delimitates the reference object and the red ones are possible results of segmentation algorithms.

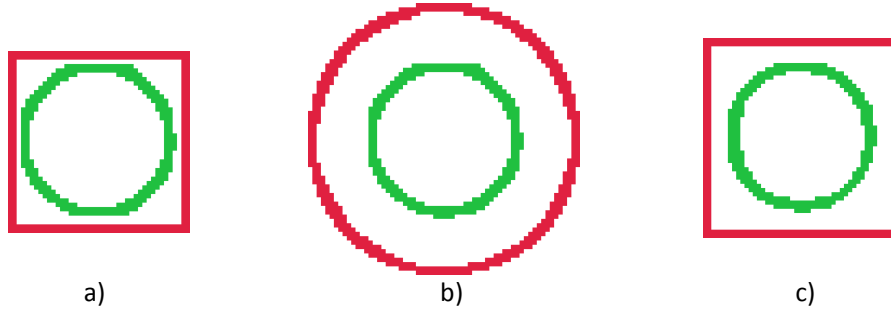


Fig.III.10 Synthetic images to illustrate the curves similarity measure [Smochina, *et al.*, 2010a].

These three segmentations are evaluated using the OSFE method with two different values for the parameter η which controls the fidelity shape relevance. Table III.2 shows the evaluation results.

| Fig.III.10 | OSFE* $\eta = 1$ | OSFE* $\eta = 0.25$ | ODI* | UDI* | FOM** | Hausdorff* |
|------------|---------------------|------------------------|--------|--------|---------|------------|
| a | 0.46 | 0.29 | 0.4665 | 0.3963 | 63.18 | 10.63 |
| b | 0.56 | 0.45 | 1.2217 | 1.2150 | 42.1101 | 13 |
| c | 0.60 | 0.41 | 0.8067 | 0.6963 | 54.57 | 14.86 |

Table III.2 Evaluation results of the segmentations from Fig.III.10 [Smochina, *et al.*, 2010a].

With $\eta = 1$, the segmentation from Fig.III.10b received a smaller error because it has the same shape like the reference object. The errors for the other two segmentations are given by the high standard deviation of the distances.

By setting the value of η to 0.25 the order is changed because the error is mainly given by the distances. In this case the errors for Fig.III.10a and Fig.III.10c are smaller because the segmentations are closer to the reference than Fig.III.10b, even though they do not have the same shape.

III.4.2. Real test images

A simple threshold segmentation algorithm is used to segment a coin (Fig.III.11). Because of the non-uniform brightness and a wrong threshold selection, the segmentations from Fig.III.11 ordered by their quality were obtained, with the corresponding evaluation results on Table III.3.

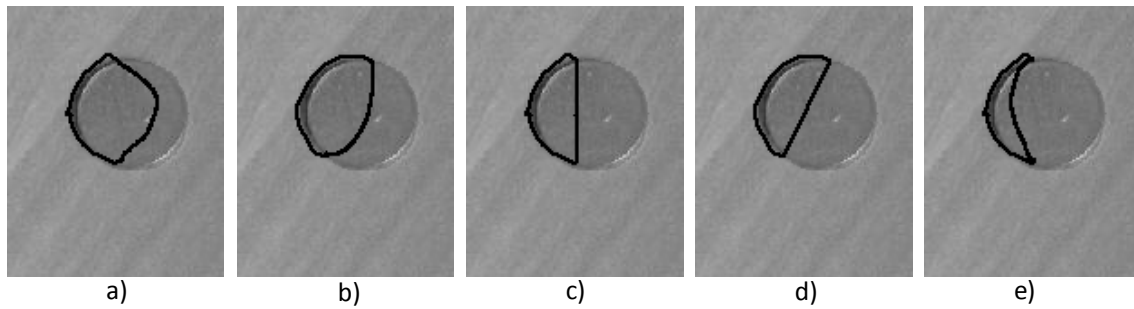


Fig.III.11 Different segmentations for a coin [Smochina, *et al.*, 2010a].

| Fig.III.11 | OSFE * $\eta = 1$ | ODI* | UDI* | FOM** | Hausdorff* |
|------------|----------------------|--------|--------|---------|------------|
| a | 0.5830 | 0.7684 | 0.9173 | 97.0844 | 20.2485 |
| b | 0.6646 | 0.8638 | 1.2307 | 97.1112 | 28.6356 |
| c | 0.7129 | 0.7205 | 1.6318 | 97.2328 | 40 |
| d | 0.7427 | 0.6647 | 1.6205 | 97.2355 | 40.2492 |
| e | 0.78 | 0.4470 | 1.7861 | 97.17 | 48.2597 |

Table III.3 Evaluation results of the segmentations from Fig.III.11 [Smochina, *et al.*, 2010a].

In Fig.III.11, the best segmentation is the one from a) and the worst is in e). The OSFE method provides correct results (i.e., small error for Fig.III.11a and high error for Fig.III.11e) regarding the right order given by the segmentations quality (Fig.III.11 a, b, c, d, e). Beside OSFE criteria, only the Hausdorff method gives correct results, but there are situations when it produces relevant mistakes as shown in [Chalana and Kim, 1997]; it also wrongly consider the Fig.III.9d segmentation better than Fig.III.9b.

For another images with coins five segmentation algorithms were implemented. In order to obtain results with high diversity, segmentation algorithms based on different approaches are used: Sobel gradient (SG), morphological gradient (MG), morphological gradient with adaptive threshold on blocks (MGB), K-means clustering (KM) and region growing (RG).

The evaluation results of the segmentation algorithms applied on the images Fig.III.12 and Fig.III.13 are shown in Table III.4 and Table III.5.

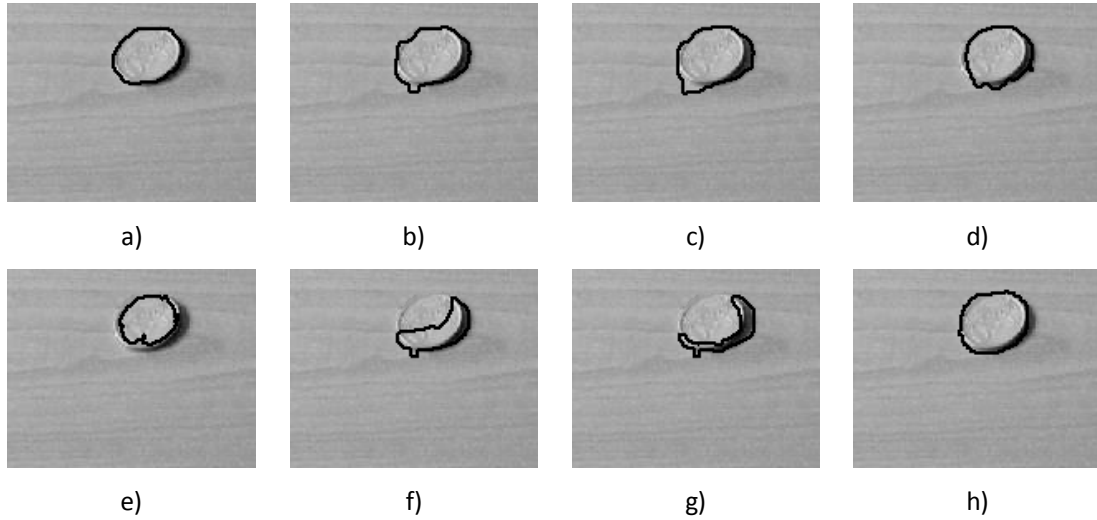


Fig.III.12 The segmentations obtained using the algorithms KM a), RG b), MG c), MGB d), SG e), MG with threshold value 0.117 f), MG with threshold value 0.118 g) and the gold standard segmentation h) [Smochina, *et al.*, 2010a].

| Fig.III.12 | OSFE* $\eta = 1$ | ODI* | UDI* | FOM** | Hausdorff* |
|-------------------|----------------------------|-------------|-------------|--------------|-------------------|
| a | 0.0998 | 0.14468 | 0.14793 | 150.616 | 3 |
| b | 0.1644 | 0.18558 | 0.17017 | 149.494 | 4.1231 |
| c | 0.1665 | 0.23079 | 0.19782 | 142.328 | 5.8309 |
| d | 0.1786 | 0.20707 | 0.22461 | 132.781 | 6.7082 |
| e | 0.3733 | 0.42109 | 0.38621 | 150.509 | 11 |
| f | 0.5538 | 0.43437 | 0.60070 | 150.556 | 21.0238 |
| g | 0.6532 | 0.27231 | 0.66976 | 130.698 | 23.0217 |

Table III.4 The evaluation results of the segmentations from Fig.III.12 [Smochina, *et al.*, 2010a].

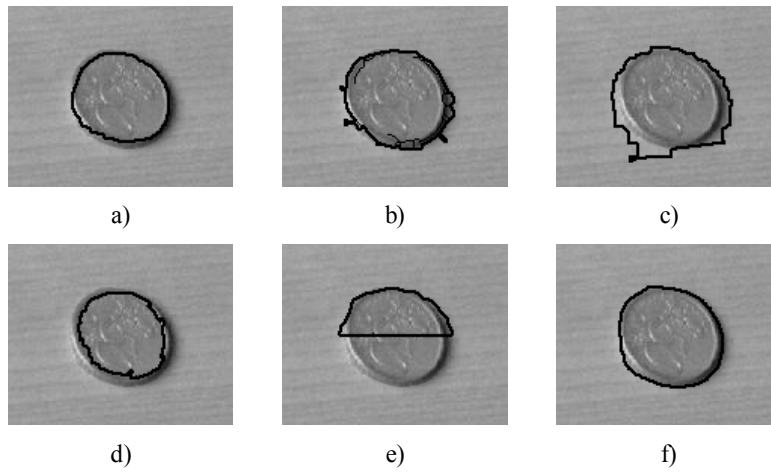


Fig.III.13. The segmentations obtained using the algorithms KM a), SG b), MG c), RG d), MGB e) and the gold standard segmentation f) [Smochina, *et al.*, 2010a].

| Fig.III.13 | OSFE* $\eta = 1$ | ODI* | UDI* | FOM** | Hausdorff* |
|-------------------|----------------------------|-------------|-------------|--------------|-------------------|
| a | 0.1577 | 0.315983 | 0.314107 | 91.0758 | 5.38516 |
| b | 0.1847 | 0.235585 | 0.153127 | 52.6698 | 7.61577 |
| c | 0.2286 | 0.427909 | 0.313212 | 68.7195 | 16.1245 |
| d | 0.3724 | 0.550001 | 0.530483 | 90.9639 | 10.7703 |
| e | 0.6948 | 0.848687 | 1.4111 | 91.2574 | 34 |

Table III.5. The evaluation results of the segmentations from Fig.III.13 [Smochina, *et al.*, 2010a].

III.5. Conclusions

In this chapter a description of the segmentation evaluation criteria and the terminology used in the evaluation process have been provided and a new approach for evaluating the performance of segmentation algorithms was proposed.

A great variety of segmentation algorithms have been proposed in the literature. The evaluation criteria aim to quantify the performance of these algorithms by different approaches. Beside the analytical or empirical unsupervised methods, only the supervised evaluation methods are analysed since they are able to concretely and accurately evaluate the segmentations. The existing supervised criteria are mostly based on the number and the position of mis-segmented pixels, the number of objects in the image, the features values of the segmented objects and miscellaneous quantities.

The proposed evaluation technique OSFE is based on the comparison: machine segmentation vs. ground-truth segmentation.

In the first phase the error measure uses the geodesic path between the segmented and the reference curve to eliminate the inconveniences that appear in the case of concave objects. The results confirmed that this approach is able to provide correct results in cases where the considered methods fail.

In the second phase, a weighted shape fitting score is computed using the previous distances to indicate the similarity between the reference and the segmentation curve. This approach allows an easy control of the method sensibility regarding the object curves similarity by setting different values to a customizable factor (η). In this way, the importance of the shape accuracy can be managed according to the field in which the method is used.

The proposed error measure was tested on segmentations of synthetic and real images and revealed itself as being the most effective in comparison with the other considered methods. The OSFE method has been applied on the comparative study of different image segmentation algorithms to demonstrate its applicability in a broad range of tasks of segmentation performance evaluation.

Only objects with Euler number 1 are considered in experiments; objects with Euler number bigger than 1 will be treated in the next studies, as well as a higher diversity of images and segmentation methods. The evaluation and comparison remains a challenging task in segmentation evaluation due to the multitude and the diversity of the applications of segmentation algorithms.

IV. Segmentation techniques for cytometry

In this chapter we address the problem of automatic segmentation for cell nuclei detection. The proposed techniques use new approaches for segmenting nuclei in images taken from tissues with colon carcinoma (Fig.IV.1) and solve the segmentation problems encountered in these images and described in I.2.1.

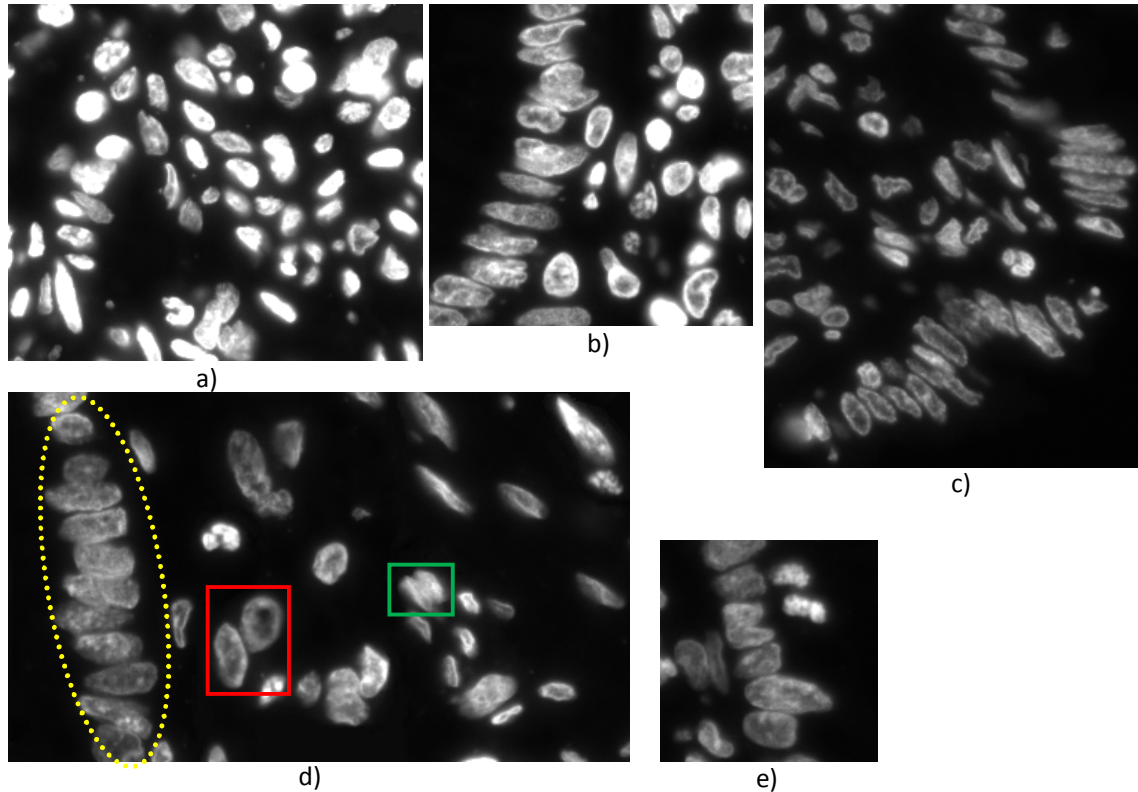


Fig.IV.1 Fluorescence image with cell nuclei from colon tissue section.

IV.1. Introduction

The critical problem in microscopic images is the touching nuclei (Fig.IV.1). There are often situations in which the separation between two nuclei has a width of only one pixel. Specific methods to detect these critical regions must be applied. Usually the separation between touching nuclei has a width of 3-4 pixels and the neighbouring pixels have higher values since they belong to the nucleus boundary.

Three segmentation techniques are presented in this section: one for the particular chained configurations (IV.3) and two for the clustered/touching cell nuclei (IV.4 and IV.5). Fig.IV.2 presents a rough scheme of the proposed segmentation techniques.

For all methods the background segmentation is the first step. Accurate background detection is obtained using two approaches: one based on region growing (IV.2.1) and the second one based on morphological reconstruction and hysteresis thresholding (IV.2.2).

The segmentation problem of specific chained configurations is addressed in IV.3 using the points with high concavity [Smochina, *et al.*, 2011a]. A set of templates and rules is used to validate and to pair the concave points so that their connecting lines indicate the separation regions between nuclei.

The clustered/touching cell nuclei within complex structures are separated using the shape of the section profile (IV.4) [Smochina, *et al.*, 2010b] or cross-correlation with a template specific to the separation areas (IV.5) [Rogojanu, *et al.*, 2010].

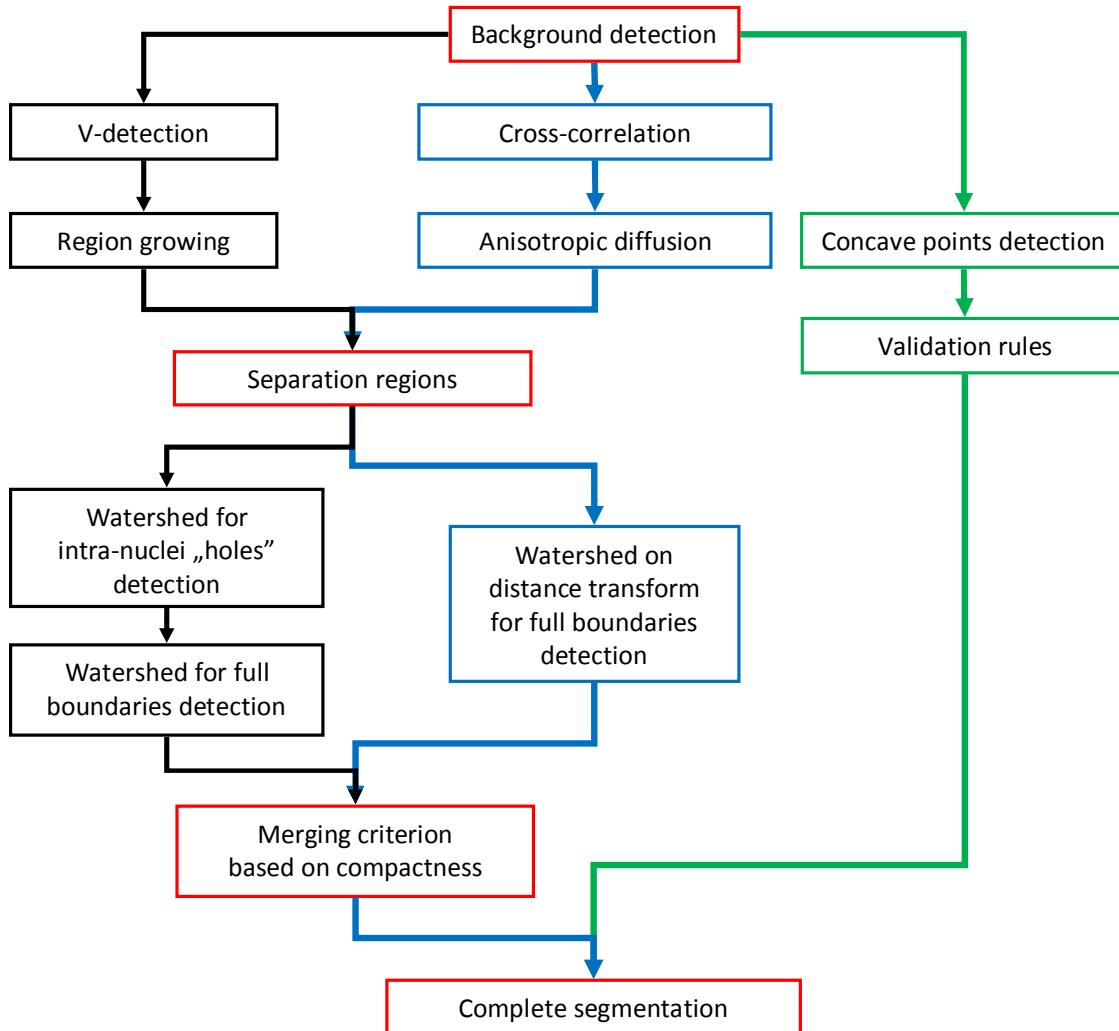


Fig.IV.2 Segmentation algorithms outline. The green flow indicates the technique used to segment the specific chained configurations (IV.3) using the points with high concavity. The black flow indicates the technique used to segment the clustered/touching cell nuclei using the shape of the section profile (IV.4) and the blue flow the approach based on cross-correlation (IV.5). The red boxes are common steps for the segmentation techniques.

IV.2. Background detection

Background segmentation is the first step for all techniques. Accurate background detection is obtained using two approaches: one based on region growing (IV.2.1) [Smochina, *et al.*, 2010b], [Rogojanu, *et al.*, 2010] and the second one based on morphological reconstruction and hysteresis thresholding (IV.2.2) [Smochina, *et al.*, 2011a].

IV.2.1. Detection using region growing

Although many existing methods use a selected threshold value to separate the objects of interest and the background [Cong and Parvin, 2000], [Laurain, *et al.*, 2005], this method is based on similarity between neighbouring pixels in the original intensity image.

Non-uniform illumination determines different grey values for the background in different regions of the image, especially near the nuclei. Also the out-of-focus nuclei increase the amount of noise which makes the correct delimitation of the background more difficult. Because of non-uniform illumination, defining the border between cell nucleus and background by a single threshold value in the image intensity is very unlikely to provide acceptable results.

Many techniques use the region growing algorithm (RG) for objects delimitation but we will use this method to detect the background with a higher accuracy (the used RG is described in II.5.1). The central idea of this method is to let the regions grow from predefined small regions, known as seeds. The regions grow by connecting non-processed neighbouring pixels which satisfy an established criterion.

This method can be used also for cell nuclei segmentation if a seed is placed within each nucleus. The difficulty caused by designing such a seeding method makes this approach inappropriate in many situations, for instance in the case of clustered and/or touching nuclei.

The seeding method for RG can give more seeds. A single seed is enough for background extraction in images with isolated nuclei. Additional seeds are needed for the background surrounded by nuclei within small ring arrangements (region R1 in Fig.IV.3b). The seeds are obtained by global thresholding the intensity image with a low threshold such that no nuclei areas are selected as seed (e.g. $thr_{\min} = 10$ for 8 bit images) [Rogojanu, *et al.*, 2010]. The seeds are depicted as blue in Fig.IV.3 (for images Fig.IV.1) and the growth of these seeds as described in II.5.1 is depicted as green.

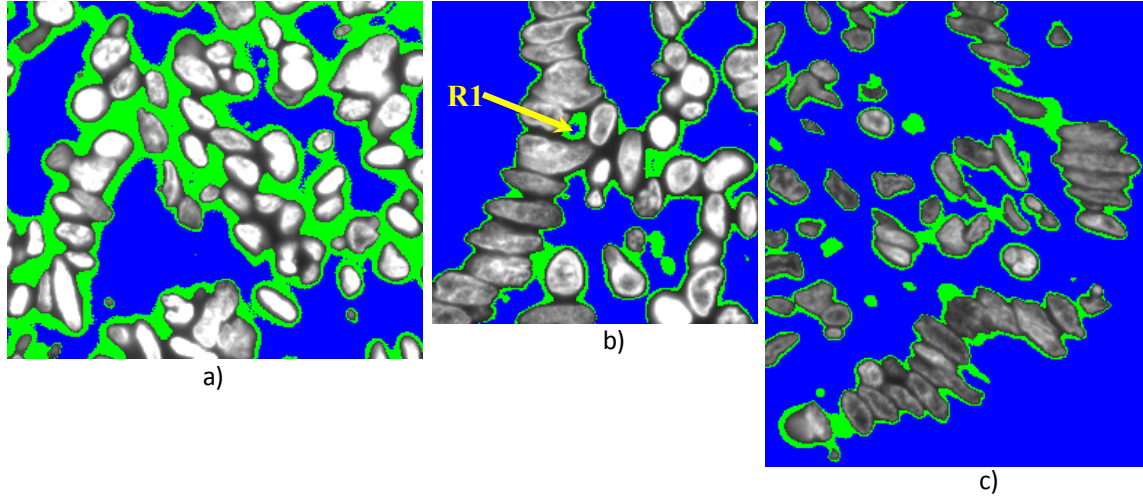


Fig.IV.3 Background detection results. The result of the initial global thresholding is depicted as blue and the growth of these seeds using region growing is drawn with green. [Smochina, *et al.*, 2010b]

IV.2.2. Detection using image reconstruction and hysteresis thresholding

The second proposed method for accurate background detection involves the anisotropic diffusion and morphological reconstruction [Smochina, *et al.*, 2011a].

The anisotropic diffusion is firstly used for noise reduction and weak boundaries enhancement. The advantages of using this nonlinear filtering method in order to significantly improve the image quality have been pointed out in II.5.3.

In order to emphasize the border between the nuclei and the background, the fast hybrid grey-scale morphological reconstruction algorithm [Vincent, 1993] is used. The morphological reconstruction processes the image marker I_{mark} based on the characteristics of the image mask I_{mask} (in our case the anisotropic filtered image: $I_{mask} = \Upsilon(I)$, where I is the input grey-scale image). The I_{mark} is given by $I_{mark} = c \cdot I_{mask}$ where $0 < c < 1$. The morphological reconstruction spreads out (dilates) the peaks from I_{mark} by forcing them to fit within the I_{mask} profile. The result of this reconstruction (I_{rec}) is further used to accurately determine the nuclei area.

By setting the coefficient c to a small value (the value 0.5 gives the best results in our experiments) this method offers the following main advantages:

- many isolated regions and artefacts originate from out-of-focus nuclei are eliminated by halving the intensities from I_{mask} ($c = 0.5$);
- the reconstruction will homogenize the I_{mark} by 'flood filling' the local minima (which appear very often within the nuclei) and by cutting off the local maxima (from the nuclei borders);

- the regions which make the ‘transition’ from background to nuclei boundaries will be suppressed.

After these improvements, the background segmentation is done by employing a hysteresis thresholding [Canny, 1986] on the reconstructed image I_{rec} . The background detected with this method is depicted as blue in Fig.IV.8a for the image Fig.IV.1e. The blue curves from Fig.IV.4a represent the background boundaries for the image Fig.IV.1d.

IV.3. Nuclei segmentation within chained configurations

In this section the particular chained structures are processed. The epithelial nuclei from these configurations are arranged like ‘beads strung on thread’ (the dashed yellow line in Fig.IV.1d delimits a chained structure).

The proposed technique for segmenting these particular configurations uses *a priori* information about the general structure and the relationship between epithelial cells nuclei and encapsulates the human behaviour on the critical regions between nuclei [Smochina, *et al.*, 2011a]. After the background detection is performed, the points with high concavity from the boundaries of the nuclei structures are detected. A set of templates and rules are established by analysing the inter-nuclei regions. These rules are used to validate and to pair the concave points so that their connecting lines to indicate the separation regions between nuclei. The evaluation of the proposed method is made with precision, recall and accuracy measures.

IV.3.1. Concave points detection

The nuclei of the chained epithelial cells have particular and similar shapes near the points of high concavity. The contours of the nuclei areas are processed to identify the concave points which represent the entry points into the separation region between touching nuclei. Usually these separation regions have a width of 2-4 pixels (Fig.IV.1d red box), but there are many situations in which there is no intensities variations to indicate such a separation region (Fig.IV.1d green box).

Let ζ^r denotes the contour of a region M_r ($\zeta^r = \partial M_r$) and ζ_i^r the i th point of the contour. Using the step ε , for each point ζ_i^r , the two neighbourhoods $N_{i-} = [\zeta_{i-\varepsilon}^r, \zeta_i^r]$ and $N_{i+} = [\zeta_i^r, \zeta_{i+\varepsilon}^r]$ are considered. Let $S_{i-\varepsilon,i}$ and $S_{i,i+\varepsilon}$ be the two segments determined by the points $\zeta_{i-\varepsilon}^r$ and ζ_i^r respectively ζ_i^r and $\zeta_{i+\varepsilon}^r$.

The ζ_i^r is further checked only if these two segments proper approximate the two neighbourhoods. The neighbourhood N_i is properly approximated by the segment S_i if the

Hausdorff distance (discussed in III.1.2) between the two corresponding set of points (points from the segment and from the curve) is smaller than η [Smochina, *et al.*, 2011a]:

$$d_H(N_{i-}, S_{i-\varepsilon,i}) < \eta \quad \text{and} \quad d_H(N_{i+}, S_{i,i+\varepsilon}) < \eta \quad (\text{IV.1})$$

This is done in order to eliminate the possible points caused by noisy boundaries or artefacts.

After ζ_i^r has been validated, the angle α between the segments $S_{i-\varepsilon,i}$ and $S_{i,i+\varepsilon}$ is computed. If $\alpha < \alpha_{\max}$ then the point ζ_i^r is marked as a concave point.

The detected concave points from Fig.IV.1d are shown in Fig.IV.4. Beside the TP results (filled red squares), the method produce FP results (empty red square) but they are eliminated by a set of ruled in IV.3.2.2.

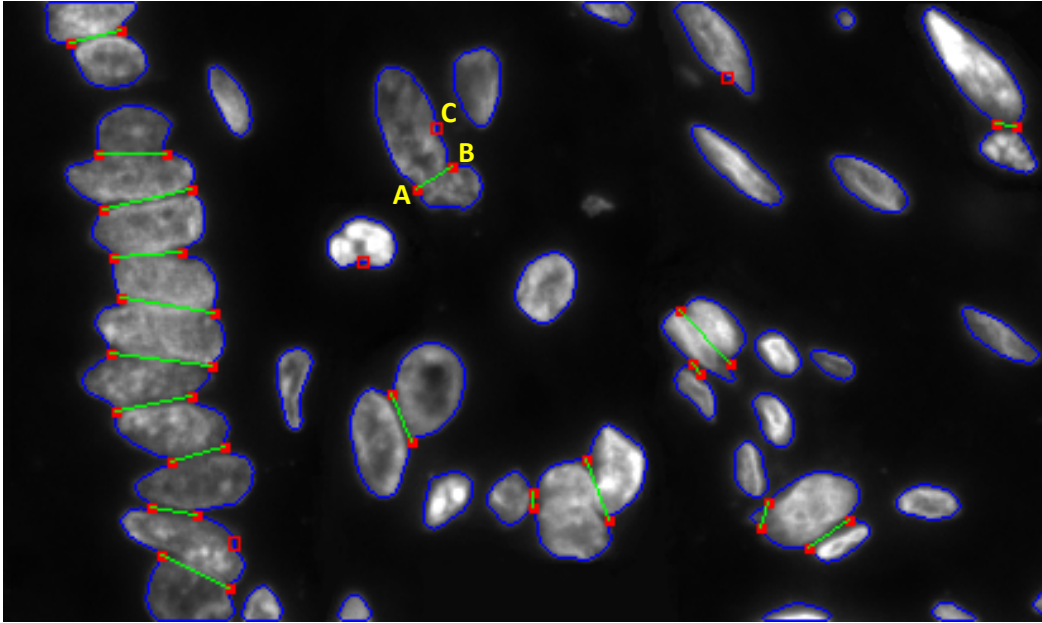


Fig.IV.4. The TP concave points (red filled squares) and the FP concave points (empty red square) on the nuclei area boundaries (blue curves). The inter-nuclei separation lines are drawn with green.

[Smochina, *et al.*, 2011a]

IV.3.2. Separation segments validation using geometrical information

A set of templates is used to detect the separation line between the chained nuclei [Smochina, *et al.*, 2011a]. These templates are created using geometric information regarding the patterns by which two nuclei are aggregating and the nuclei ellipse-like boundaries. Templates and rules of high biological plausibility are established by observing a high number of touching and chained nuclei.

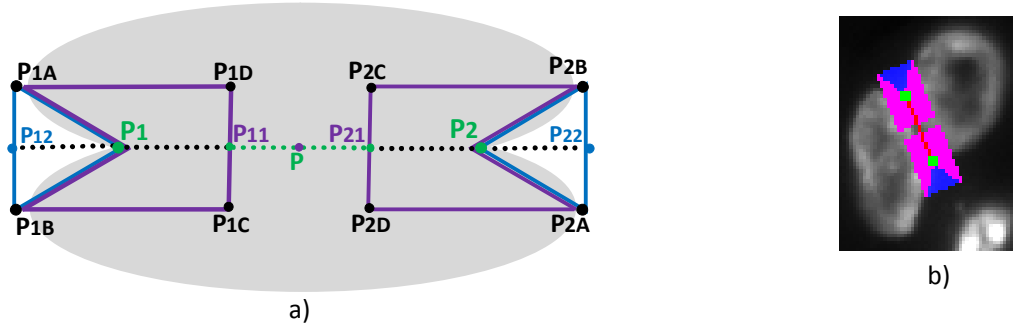


Fig.IV.5 a) The ideal situation of two touching nuclei and the analyzed areas used to design the templates. b) Two touching nuclei (red box from Fig.IV.1d) from real fluorescence image and the applied templates (blue and purple) to validate the inter-nuclei separation line (red line). [Smochina, *et al.*, 2011a]

IV.3.2.1. Geometrical templates for touching nuclei

In Fig.IV.5a the points P_1 and P_2 are the concave points detected using the method previously described in section IV.3.1. The situation presented in Fig.IV.5a is the ideal one in which the touching nuclei (with ellipse-like boundaries) delimit two symmetric regions with the centres of gravity in the points P_1 and P_2 . We approximate these regions with two rectangles $R_1(P_{1A}, P_{1B}, P_{1C}, P_{1D})$ and $R_2(P_{2A}, P_{2B}, P_{2C}, P_{2D})$ such that the points P_1 and P_2 represent the intersection of the diagonals.

Two region types can be delimited in each rectangle R . The first one contains the background and can be approximated by a triangle T (drawn with blue) with the apex in the concave point and the base given by the rectangle side from the background area. The second one, K (drawn with purple) is the region containing nuclei pixels. It represents the area left after subtracting the triangle T from the rectangle R .

For the two rectangles R_1 and R_2 (R_2 can be seen as the mirroring of R_1 from point $P \in [P_1, P_2]$) we obtained the triangles $T_1(P_1 P_{1A} P_{1B})$ and $T_2(P_2 P_{2A} P_{2B})$ respectively the regions $K_1(P_1 P_{1B} P_{1C} P_{1D} P_{1A})$ and $K_2(P_2 P_{2B} P_{2C} P_{2D} P_{2A})$. The points P_1 and P_2 are considered the apexes of these triangles and the bases are perpendicular on the line (P_1, P_2) [Smochina, *et al.*, 2011a].

$$P_{1A}P_{1B} \perp (P_1P_2), P_{1B}P_{1C} \perp (P_1P_2) \quad (IV.2)$$

This geometric representation is an approximation of an ideal situation. In real images strong variations can appear but all have in common the structure of this model: two symmetric rectangles, each one containing a triangle with the apex in the concave point

mostly covering the background and the rest of the rectangle mostly covering the nuclei areas; we define ‘mostly’ by overlapping percentages.

IV.3.2.2. Validation rules

Let B represent the detected background, N the nuclei area, and two concave points P_i and P_j with their associated templates T_i, K_i respectively T_j, K_j . Since the method used to detect the concave points can provide FP results the following validation rules from Table IV.1 are used [Smochina, *et al.*, 2011a]:

| Overlapped areas | Rules |
|-------------------------------------|--|
| $o_{T_i} = \text{card}(B \cap T_i)$ | $r_1 = o_{T_i} > c_T \cdot \text{card}(T_i)$ |
| $o_{T_j} = \text{card}(B \cap T_j)$ | $r_2 = o_{T_j} > c_T \cdot \text{card}(T_j)$ |
| $o_{K_i} = \text{card}(N \cap K_i)$ | $r_3 = o_{K_i} > c_K \cdot \text{card}(K_i)$ |
| $o_{K_j} = \text{card}(N \cap K_j)$ | $r_4 = o_{K_j} > c_K \cdot \text{card}(K_j)$ |

Table IV.1 Validation rules [Smochina, *et al.*, 2011a].

The concave point P_i is valid if the expressions r_1 and r_3 are true, i.e., $r_{13} = r_1 \wedge r_3$ must be true. The point P_j is valid if $r_{24} = r_2 \wedge r_4$ is true.

The path between P_i and P_j is valid if $r = (r_1 \wedge r_3) \wedge (r_2 \wedge r_4)$ is evaluated as true. An additional rule r_a is added to avoid checking all pairs of points and improve computation time: two points can be associated only if $d_E(P_i, P_j) < d_{\max}$, i.e. the Euclidean distance between points must be smaller than the maximum possible length of a separation region between two cells nuclei. The value for d_{\max} is established according to the nuclei size. If a pair of points is validated with rule r , then the corresponding segment $[P_i P_j]$ receives the following weight [Smochina, *et al.*, 2011a]

$$w_{ij} = \alpha(o_{T_i} + o_{T_j}) + \beta(o_{K_i} + o_{K_j}) \quad (\text{IV.3})$$

A higher importance was given for the triangles matching by setting $\alpha = 3$ and $\beta = 1$. A normalization of this weight is not necessary because the maximum weight will be considered in the rule w_{is} (Eq.IV.4).

The rule r_{13} (or r_{24}) checks if a concave point is in an area with the same structure as the ideal one (Fig.IV.5a), i.e., a rectangle with two areas: a triangle containing the background

and a region that overlaps the nuclei areas. The rule r is valid for two points (validated before by rule r_{13} or r_{24}) only if these points indicate the entrance within a separation region between two nuclei (true separation segment). If rule r_{13} (and r_{24}) marks the correct concave points, the rule r associates two points so that the line connecting the points coincides with the nuclei separation line. After this checking is done, not every point must be associated to another one; the single remaining points are FP results and they appear due to the nuclei irregular shape.

In this validation process the following situation can appear: by checking a concave point P_i with all others points from a region's boundary (except those from a distance bigger than d_{\max}), more than one point can be associated with point P_i , i.e. more than one pairs validate the rule r . If Γ is the set of these points, the selected point P_s for the current point P_i is chosen such that the weight of this pair to be maximum (rule r_w).

$$w_{is} = \max \{w_{ik}, P_k \in \Gamma\} \quad (\text{IV.4})$$

IV.3.3. Results

In Fig.IV.4 and Fig.IV.8b the results of separation lines detection from Fig.IV.1d and Fig.IV.1e are shown. The blue curve represents the boundaries of the detected background and the red points (the filled ones and those indicated by empty squares) represent the concave points. The green lines are determined only by pairs of points which validate the r rule (and r_w in cases of multiple validated lines for the same point). The points which do not validate rule r_{13} (or r_{24}), rule r or r_w are marked with empty squared. For instance, the rule r_w was used to choose path AB instead of AC for point A in Fig.IV.4. BC does not validate rule r .

Fig.IV.6 presents touching nuclei with high intensity variations within nuclei. In Fig.IV.6a the pixels from the nucleus's interior have lower grey values than those from the boundaries. In Fig.IV.6c, e and g the nuclei have a non-uniform distribution of the material inside which determine the 'channels' with low intensities. The concave points and the inter-nuclei separation lines are shown in Fig.IV.6b, d, f and h.

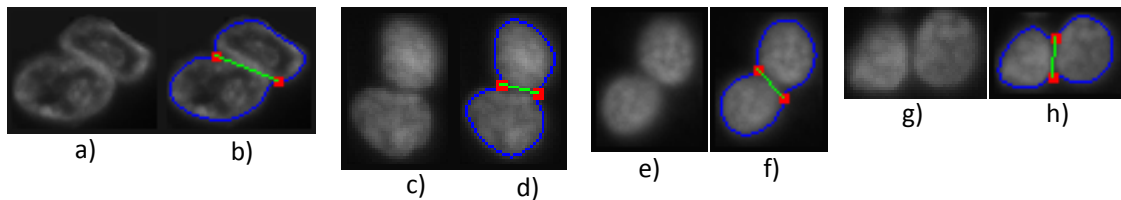


Fig.IV.6 a, c, e, g) Touching nuclei. b, d, f, h) The true concave points delimiting the inter-nuclei separation lines. [Smochina, *et al.*, 2011a]

In Fig.IV.1d the green box highlights a special case of two touching nuclei without significant intensities variation on the separation region. This lack of information for the touched nuclei boundaries can also be seen in the chained structure. Any method that does not take into consideration geometrical knowledge will fail in separating these nuclei.

The proper detection of the concave points is achieved due to accurately background extraction. The points are validated and paired by the set of rules. The complete nuclei boundaries are depicted with red in Fig.IV.7.

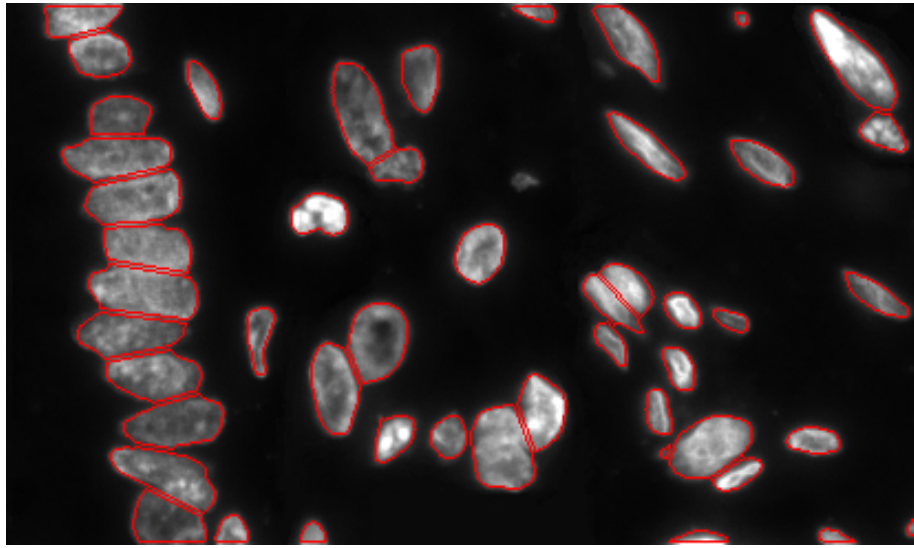


Fig.IV.7 Nuclei boundaries [Smochina, *et al.*, 2011a].

Fig.IV.1e shows another chained structure with a few stroma cells and the full boundaries are depicted as red in Fig.IV.8c.

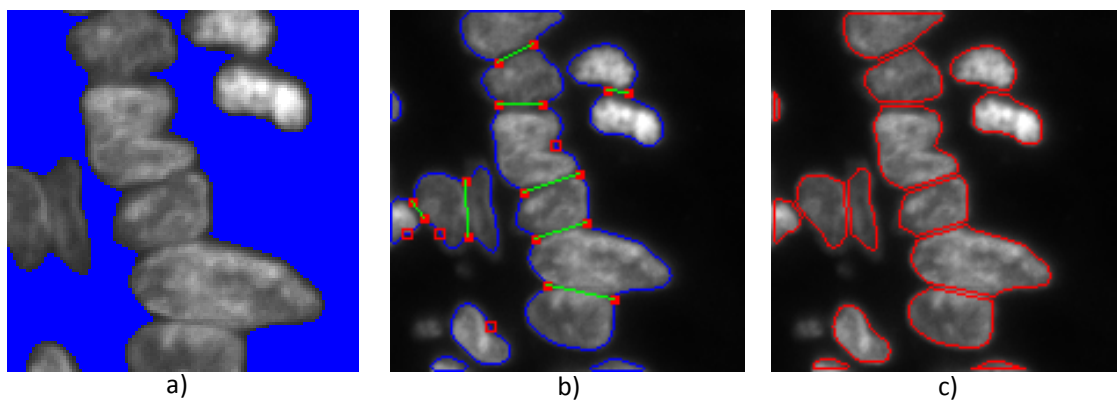


Fig.IV.8 a) The background of the image Fig.IV.1e is depicted as blue. b) The TP concave points (red filled squares) and the FP concave points (empty red square) on the nuclei area boundaries (blue curves). c) Nuclei boundaries. [Smochina, *et al.*, 2011a]

IV.3.3.1. Evaluation

The proposed segmentation technique was tested on different datasets of images from tissues labelled with DAPI and compared against ground-truth segmentations. The images contain chained nuclei into long structures but also nuclei from stroma areas (isolated and touching). The results confirmed that the proposed method could efficiently segment isolated and chained cell nuclei with a high degree of accuracy. Beside visual inspection a more rigorous evaluation is done by comparing against the ground truth segmentations. The performance of the algorithm is established by determining how far the obtained segmentation is from the gold standard segmentation (the average of curves [Chalana and Kim, 1997] drawn by three human experts). Using the precision, recall and accuracy measures described in III.1.1, the evaluation results from Table IV.2 are obtained.

| Image | P | R | A |
|-----------|-------|-------|-------|
| Fig.IV.4 | 0.927 | 0.930 | 0.965 |
| Fig.IV.8c | 0.926 | 0.925 | 0.948 |
| Fig.IV.6b | 0.990 | 0.870 | 0.939 |
| Fig.IV.6d | 0.991 | 0.880 | 0.936 |
| Fig.IV.6f | 0.986 | 0.874 | 0.921 |
| Fig.IV.6h | 0.984 | 0.889 | 0.937 |
| averages | 0.967 | 0.895 | 0.941 |

Table IV.2 Segmentations evaluation results [Smochina, *et al.*, 2011a].

The accuracy obtained on the entire images set is 0.913 and low recall and high precision indicate an over segmentation tendency. Since the technique is designed to solve the problems in chained structure with low information about the separation regions, the accuracy can decrease with 5% due to unexpected organizations in stroma regions.

The used set of rules guaranties the detection of the considered situations and do not produce FP results in situations not covered by the used templates. This allows the use (in other fields or with different input images) of this method in combination with techniques designed for other particular situations.

IV.4. Touching nuclei detection using profile shape

The key of the technique proposed in this section is given by the sequence of filters applied in order to highlight the separation lines between touching/clustered cell nuclei [Smochina, *et al.*, 2010b]. These filters are designed according to the shape of separation regions profile (IV.4.1). The full nuclei boundaries are obtained using the watershed algorithm and considering as seeds the detected background and the separation lines (IV.4.2). Since the watershed usually produces over-segmented results, an adequate merging region criterion is used to correctly identify the nuclei (IV.4.2.1).

IV.4.1. V-shape detection

The pixels from the separation regions/lines have the property that their grey values are smaller than the grey values of the neighbouring pixels from both the right and left side. We can imagine that these pixels are in a valley (the separation line) with low intensities and the neighbouring pixels with higher values form two hills on the left and the right side. The profile of these sections has a V shape, thus the name of the proposed method.

For each candidate pixel, the pixels within a 2D kernel/rectangle Q with the centre given by the candidate pixel are considered. We mark a pixel as belonging to a separation region if the majority of the neighbouring pixels from a specific orientation can be considered as belonging to a separation line. We use the abbreviation SRP to indicate a point belonging to a separation region (SR).

Each pixel from the centre column of the kernel is compared with the convolutions results between the left and the right line and a 1D Gaussian kernel. If the pixel's grey value plus a value $nMinOffset$ is smaller than both convolutions results then it is marked as SRP.

After checking each pixel from the centre column, the following rule is applied: if the number of marked pixels from the centre column is bigger than a value $nMinVpixels$, the centre of the kernel is marked as belonging to a separation line since it is surrounded by possible pixels belonging to separation lines [Smochina, *et al.*, 2010b].

As we do not know the orientation of the possible separation line which contains the candidate pixel, the process described above will be repeated by rotating the kernel Q with 45, 90 and 135 degrees. In this way the pixels from all separation lines will be found.

IV.4.1.1. Particular example

For a better understanding let's consider a possible kernel Q with the following sizes $nKernelWidth = 9$, $nKernelHeight = 3$ and a 1D Gaussian kernel Q_G with the standard deviation 1, $Q_G = [0.1345 \ 0.3655 \ 0.3655 \ 0.1345]$.

The number of values from Q_G is $(nKernelWidth - 1)/2$, where $nKernelWidth$ is an odd number. The kernels used to process each pixel from the centre column are shown in Fig.IV.9.

| | | | | | | | | | | | | | | | | | | |
|------------------|--------|--------|--------|--------|--------|--------|--------|--------|------------------|--------|--------|--------|--------|--------|--------|--------|---|---|
| K_line1_L | | | | | | | | | K_line2_L | | | | | | | | | |
| 0.1345 | 0.3655 | 0.3655 | 0.1345 | 0 | 0 | 0 | 0 | 0 | 0 | 0 | 0 | 0 | 0 | 0 | 0 | 0 | 0 | 0 |
| 0 | 0 | 0 | 0 | 0 | 0 | 0 | 0 | 0 | 0.1345 | 0.3655 | 0.3655 | 0.1345 | 0 | 0 | 0 | 0 | 0 | |
| 0 | 0 | 0 | 0 | 0 | 0 | 0 | 0 | 0 | 0 | 0 | 0 | 0 | 0 | 0 | 0 | 0 | 0 | |
| K_line1_C | | | | | | | | | K_line2_C | | | | | | | | | |
| 0 | 0 | 0 | 0 | 1 | 0 | 0 | 0 | 0 | 0 | 0 | 0 | 0 | 0 | 0 | 0 | 0 | 0 | |
| 0 | 0 | 0 | 0 | 0 | 0 | 0 | 0 | 0 | 0 | 0 | 0 | 0 | 1 | 0 | 0 | 0 | 0 | |
| 0 | 0 | 0 | 0 | 0 | 0 | 0 | 0 | 0 | 0 | 0 | 0 | 0 | 0 | 0 | 0 | 0 | 0 | |
| K_line1_R | | | | | | | | | K_line2_R | | | | | | | | | |
| 0 | 0 | 0 | 0 | 0.1345 | 0.3655 | 0.3655 | 0.1345 | 0 | 0 | 0 | 0 | 0 | 0 | 0 | 0 | 0 | 0 | |
| 0 | 0 | 0 | 0 | 0 | 0 | 0 | 0 | 0 | 0 | 0 | 0 | 0 | 0.1345 | 0.3655 | 0.3655 | 0.1345 | 0 | |
| 0 | 0 | 0 | 0 | 0 | 0 | 0 | 0 | 0 | 0 | 0 | 0 | 0 | 0 | 0 | 0 | 0 | 0 | |
| a) | | | | | | | | | b) | | | | | | | | | |
| K_line3_L | | | | | | | | | K_line3_C | | | | | | | | | |
| 0 | 0 | 0 | 0 | 0 | 0 | 0 | 0 | 0 | 0 | 0 | 0 | 0 | 0 | 0 | 0 | 0 | 0 | |
| 0 | 0 | 0 | 0 | 0 | 0 | 0 | 0 | 0 | 0.1345 | 0.3655 | 0.3655 | 0.1345 | 0 | 0 | 0 | 0 | 0 | |
| 0 | 0 | 0 | 0 | 0 | 0 | 0 | 0 | 0 | 0 | 0 | 0 | 0 | 0 | 0 | 0 | 0 | 0 | |
| 0 | 0 | 0 | 0 | 0 | 0 | 0 | 0 | 0 | 0 | 0 | 0 | 0 | 1 | 0 | 0 | 0 | 0 | |
| K_line3_R | | | | | | | | | K_line3_C | | | | | | | | | |
| 0 | 0 | 0 | 0 | 0 | 0 | 0 | 0 | 0 | 0 | 0 | 0 | 0 | 0 | 0 | 0 | 0 | 0 | |
| 0 | 0 | 0 | 0 | 0 | 0 | 0 | 0 | 0 | 0 | 0 | 0 | 0 | 0 | 0 | 0 | 0 | 0 | |
| 0 | 0 | 0 | 0 | 0 | 0.1345 | 0.3655 | 0.3655 | 0.1345 | 0 | 0 | 0 | 0 | 0 | 0 | 0 | 0 | 0 | |
| c) | | | | | | | | | | | | | | | | | | |

Fig.IV.9 Kernels used to detect the points from the separation regions for each line of the kernel Q [Smochina, *et al.*, 2010b].

The convolutions “*” between the intensity image I and kernels from Fig.IV.9a in order to obtain the value from the centred column, first row for orientation 0 are given by Eq.IV.5 [Smochina, *et al.*, 2010b]:

$$\text{lineV0_c1} = \left[(I * K_line1_C + nMinOffset) < (I * K_line1_L) \right] \wedge \left[(I * K_line1_C + nMinOffset) < (I * K_line1_R) \right] \quad (IV.5)$$

For the second (lineV0_c2) and third row (lineV0_c3) from the example, the convolutions are similar to Eq.IV.5 but the kernels from Fig.IV.9b respectively Fig.IV.9c are used. These three results are concatenated in Eq.IV.6.

$$\text{lineV0} = \text{lineV0_c1} + \text{lineV0_c2} + \text{lineV0_c3} \quad (IV.6)$$

The pixels values from the first intermediate result lineV0 represent the number of possible pixels (from the centre column of the kernel Q) belonging to a separation line with orientation 0.

To obtain the possible pixels situated on the separation lines with orientation of 45, 90 and 135 degrees (lineV45, lineV90 respectively lineV135), the previous process is repeated for all rotations of the kernels from Fig.IV.9 with 45, 90 and 135 degrees.

A pixel is marked as belonging to a separation line if its value is higher than $nMinVpixels$, i.e., the number of possible pixels from the centre column of the kernel Q is bigger than $nMinVpixels$. This rule is applied for the results corresponding to each orientation. The final result is given by a binary ‘OR’ (\vee) operation between all intermediate results [Smochina, *et al.*, 2010b]:

$$\begin{aligned} \text{lineV} = & (\text{lineV}0 > nMinVpixels) \vee (\text{lineV}45 > nMinVpixels) \vee \\ & (\text{lineV}90 > nMinVpixels) \vee (\text{lineV}135 > nMinVpixels) \end{aligned} \quad (\text{IV.7})$$

The SRPs are marked with true in the binary image lineV and are depicted with green and red in Fig.IV.10a.

IV.4.1.2. Validation the separation regions

This approach produces FP results in case of the nuclei with lower intensities inside than on the boundaries. These regions with lower intensities will be considered by the ‘V-detection’ method as separation lines since they are expected to appear between nuclei.

The FP results are ignored by judging their position. The TP results founded between the nuclei have the property that ‘touch’ the background, i.e., regions drawn with green in Fig.IV.10a, Fig.IV.11a and Fig.IV.12a. The wrong separation lines founded within nuclei are ignored since they cannot ‘touch’ the background, i.e., regions drawn with red in Fig.IV.10a, Fig.IV.11a and Fig.IV.12a. The nuclei boundaries have high intensities and act as a wall between the background and the FP results within the nuclei.

IV.4.1.3. Region growing for more accurately separation regions

In case of clustered nuclei, the ‘V-detection’ will highlight the separation lines. There are situations in which a ring or a group of touched nuclei surrounds a small background are not found by the background extraction approach (e.g., region R1 in Fig.IV.11a).

The region growing algorithm is applied using as seeds the selected separation lines (from IV.4.1.2) with a smaller value for the growing parameter thr_{grow} (II.5.1). After this growing, the selected separation regions became more obviously and the small areas between grouped nuclei are filled, i.e., marked as separation regions. This growth is depicted as blue in Fig.IV.10a, Fig.IV.11a and Fig.IV.12a.

IV.4.2. Watershed for detecting boundaries of full nuclei

To detect the nuclei boundaries, the watershed algorithm (II.5.2) is applied in two phases. The structure of the nuclei with high intensity variations within the nuclei causes difficulties in boundaries detection. Because of the internal DNA distribution, some nuclei have the ring-shape pattern with lower intensities in the centre of the nucleus. The first application of the watershed algorithm tries to detect these regions.

The watershed algorithm is applied considering as seeds the detected background, the reached separation lines and the results offered by the extended minima transform. In this case, the watershed basins will grow in regions within the nuclei and they will fill each area with low intensities founded in the interior of the nuclei. For the nuclei without low intensities in interior there will be no catchment basins created. Imposing as seeds the local minima makes the watershed lines to appear within the nucleus (for the nuclei with low intensities in interior) but do not coincide with nucleus boundaries.

In another category of nuclei are those with higher intensity values in the interior of the nucleus than on the boundaries, cone-shaped nuclei. To detect these cell nuclei the watershed algorithm should be applied on the reversed intensity image. If the images contain only nuclei with higher intensity values in the interior, by reversing the intensity image these nuclei will form the proper basins in which the water can accumulate.

Since the images contain both types of nuclei (with higher and lower intensities within nucleus), the result of the first watershed run is used on the reversed intensity image. By reversing the nuclei with lower intensities in interior, the nucleus boundaries will surround regions with high intensities. The watershed lines founded on the first watershed run delimit these regions with high intensities from the reversed intensity image. If the regions founded by the first watershed run are imposed as seeds in the reversed image, the problems related to the nuclei with lower intensities within nucleus are eliminated. Also the background and the reached separation lines are used as seeds. The second watershed run detects the nuclei in the reversed intensity image. The obtained regions are shown in Fig.IV.10b, Fig.IV.12b and Fig.IV.11b.

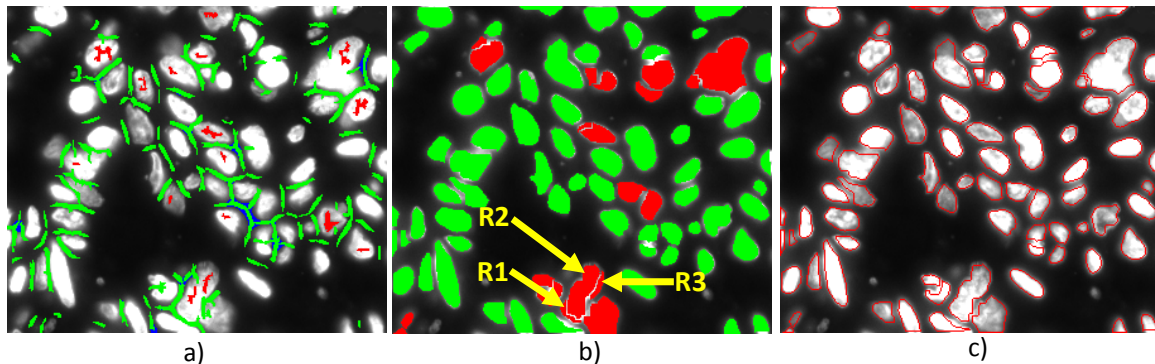


Fig.IV.10 Intermediate results of the segmentation process for the image Fig.IV.1a.

a) The regions with red represent the results of the “V-detection” method (FP results) ignored because they are within the nuclei. The selected separation lines are depicted as green and the

growth of these lines with blue. b) The result of the watershed algorithm: the isolated regions are depicted as green and the regions to be verified for merging with red. c) The boundaries of the final detected regions after merging. [Smochina, *et al.*, 2010b]

IV.4.2.1. Merging regions

Even if the seeded watershed is used, the over-segmented results are likely to occur. We compute a region adjacencies graph of the labelled image after applying the watershed. The relationship between regions is given by the watershed lines. Two regions are considered neighbours if they are separated by a watershed line. In Fig.IV.10b the isolated nuclei are depicted as green and the regions to be verified for merging with red.

A shape descriptor widely used in pattern recognition tasks is used as merging criterion: shape compactness. The shape compactness of a region is given by $C = 4\pi A/P^2$ where P is the region perimeter and A is the region area; $C = 1$ for a circle and decreases according to the shape changes [Montero, 2009], [Nixon and Aguado, 2002].

Two adjacent regions are merged if the compactness of the unified region is bigger than the minimum compactness of these two regions [Smochina, *et al.*, 2010b]. E.g., for two neighbouring regions R_1 and R_2 , the condition $C(R_{12}) > \min(C(R_1), C(R_2))$ is evaluated where R_{12} is the union of these two. For instance, the regions R_1 , R_2 and R_3 from Fig.IV.10b or regions R_2 and R_3 from Fig.IV.11b have been merged based on this criterion.

IV.4.3. Results

The proposed segmentation technique was tested on different datasets of images of cell nuclei labelled with DAPI and compared against ground-truth segmentations. In all the datasets the algorithm gave comparable results even if there were some significant differences between the datasets. In some images the nuclei were distributed sparsely throughout the image while in some others they were grouped together. The results confirmed that the proposed method could efficiently segment isolated and touching cell nuclei. Fig.IV.1a, b, c show some of the representative images and Fig.IV.10c, Fig.IV.11c and Fig.IV.12c present the segmentation results as a red border around the nuclei.

The selected threshold for background extraction thr_{min} and the value thr_{grow} used in region growing algorithm in case of Fig.IV.1a could be higher because the image is slightly over-exposed. Bigger values for these parameters determine quick and accurate background detection. But for Fig.IV.1b these highly values will produce FP results by marking as background also parts of cell nuclei with low intensities. The applied region growing method cannot mark as background the separation region between cell nuclei: it can only delimit the clustered or touching nuclei (for instance region R_1 from Fig.IV.12a). The proposed method

succeeds to detect the separation regions in these situations and can also be applied on images from other application areas.

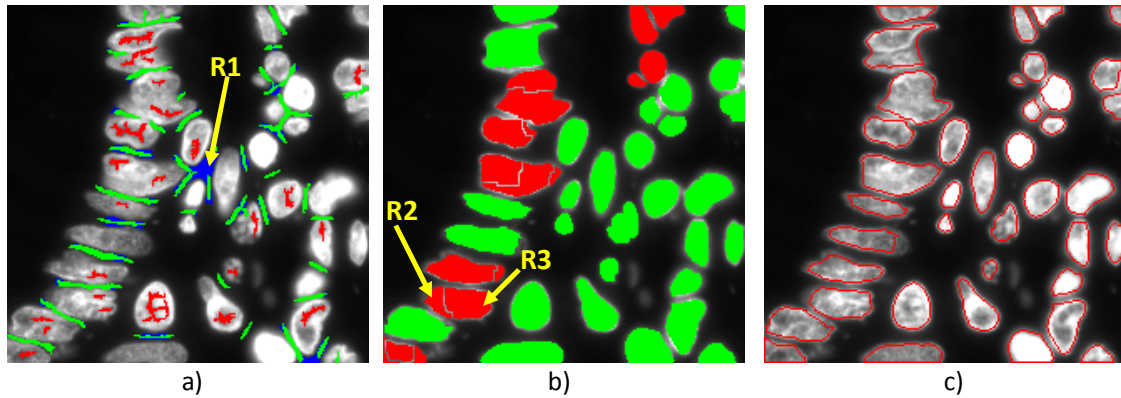


Fig.IV.11 The intermediate and the final results of the segmentation applied on the image from Fig.IV.1b [Smochina, *et al.*, 2010b].

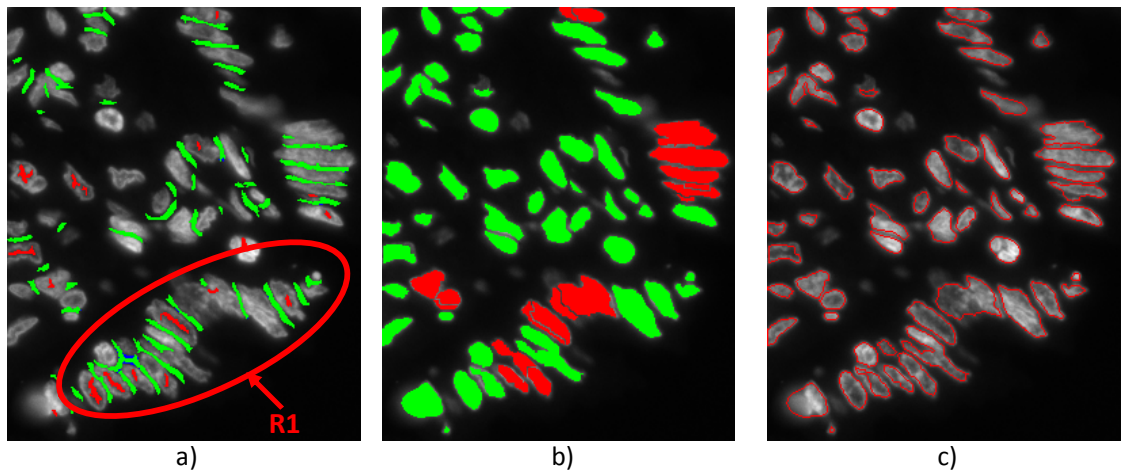


Fig.IV.12 The intermediate and the final results of the segmentation applied on the image from Fig.IV.1c [Smochina, *et al.*, 2010b].

IV.5. Touching nuclei detection using cross-correlation

The second technique proposed for segmenting the critical arrangements of touching/clustered nuclei uses the cross-correlation to highlight the regions between the cell nuclei (IV.5.1) [Rogojanu, *et al.*, 2010]. The detected separation regions between grouped cell nuclei are validated based on their link with the background (IV.5.2). Then, the nuclei boundaries are identified by applying the watershed algorithm on the complemented distance transform of the binary image containing the selected separation lines (IV.5.3).

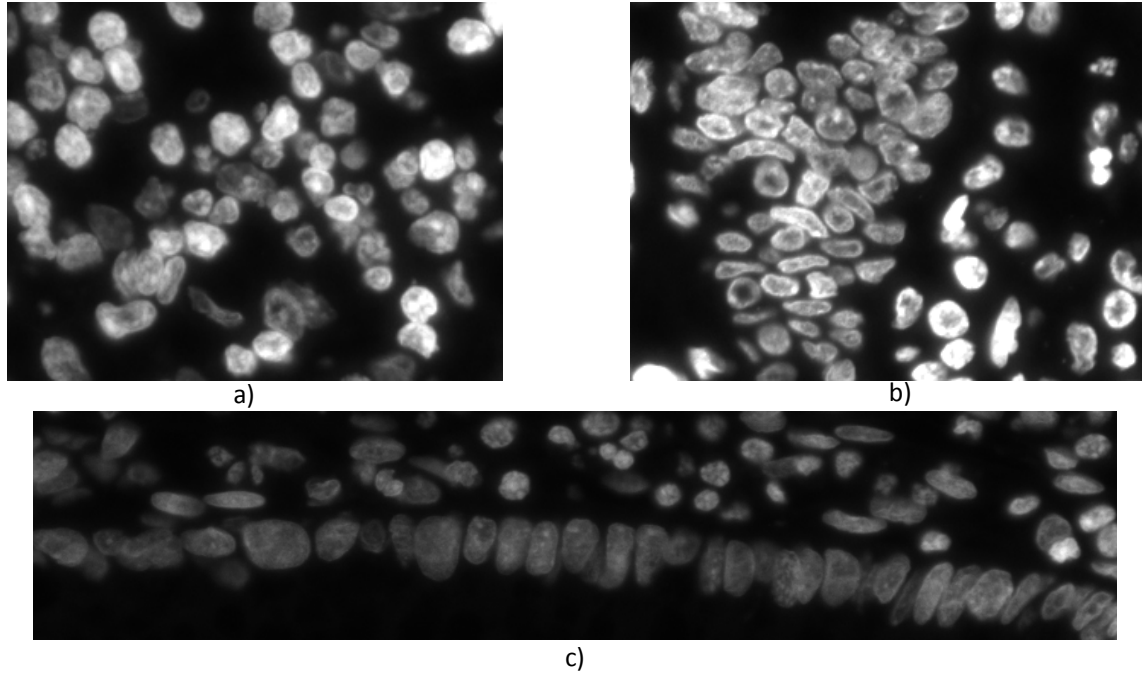


Fig.IV.13 Cell nuclei in colon tissue sections [Rogojanu, *et al.*, 2010].

The background detection results performed on the images from Fig.IV.13 using the technique based on region growing (IV.2.1) are shown in Fig.IV.14.

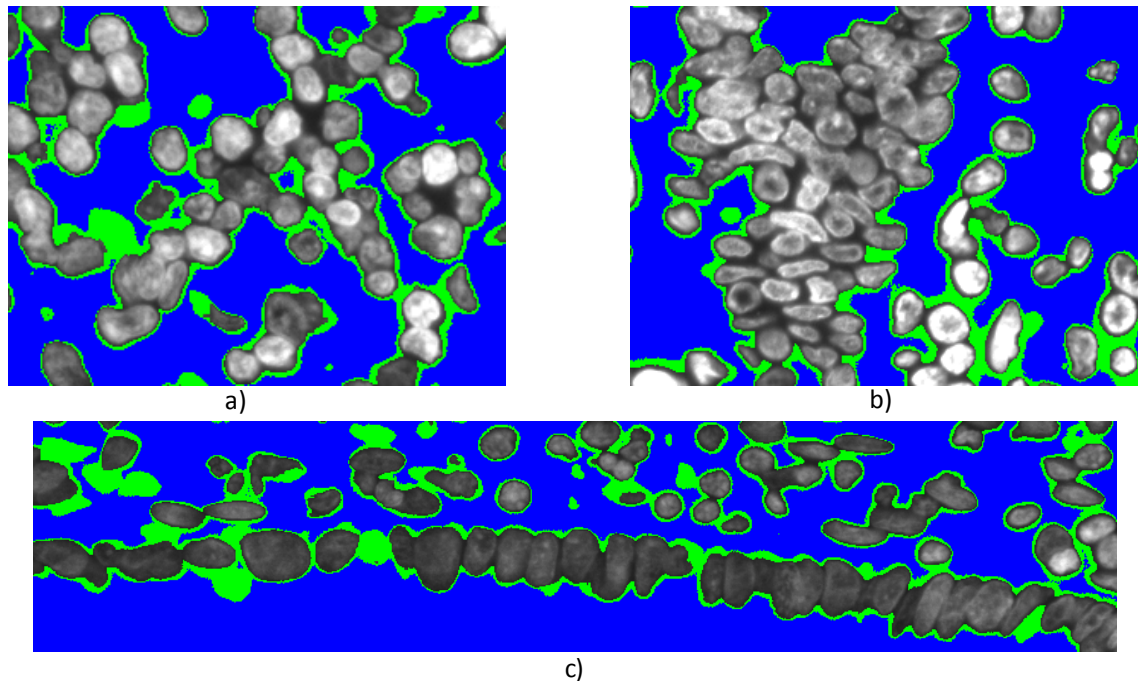


Fig.IV.14 Background detection for the images from Fig.IV.13. The growth of the initial thresholding (blue) using region growing is depicted as green. [Rogojanu, *et al.*, 2010]

IV.5.1. Cross-correlation with a Gaussian-complement

The cross-correlation can be used to detect the cell nuclei by defining a set of templates which covers all for nucleus types. This is hard to achieve since the used images contain nuclei whose features (like shape and/or size and/or orientation) have considerable variations. In addition, the high variations of pixel intensities within the nucleus make this approach inadequate.

Instead, the cross-correlation is used to highlight the regions between the cell nuclei. Defining a template able to characterize the whole separation region between two or more nuclei is also not a trivial task. We simplify the problem by focusing only on the properties of the pixels from the separation regions. An important property of these pixels has been exploited: their grey values are smaller than the grey values of the neighbouring pixels. This is the reason why the complement of a 2D Gaussian kernel (GKT) with a small size 3×3 was used as template. Instead of searching regions that fit a certain template, we highlight the pixels within a small area which have high similarity with the small template. The cross-correlation between the intensity image and the template GKT gives correlation coefficients with high values for the pixels from the separation regions.

This approach produces FP results in case of the nuclei with lower intensities inside than on the boundaries. These regions with lower intensities will be also considered as SR. For this type of nuclei (with low intensities within the nucleus), the boundaries have low correlation coefficients (often negative values) since the corresponding pixels have intensities

higher than their neighbours. The negative correlation coefficients are ignored and only the positive coefficients corresponding to separation regions must be considered.

IV.5.1.1. Separation regions enhancement using the anisotropic diffusion

Since this approach is based on pixel highlighting/classification, the separation regions might have different coefficients. In many situations they are similar (or even smaller) with these offered by the intra-nucleus regions with lower intensities. A filter must be applied to homogenize the regions with high correlation coefficients and enhance the contrast with regions having lower coefficients.

The anisotropic diffusion filtering on the cross-correlation result improves the selection of the correct pixels from the separation regions and ignoring those within the nucleus. Using the anisotropic diffusion filtering, minor gaps in the separation lines are filled.

IV.5.2. Detecting the separation regions

The nuclei boundaries should offer very small correlation coefficients (ideally negative) since their intensities are higher than those from the separation regions. After improving the contrast between the high and low coefficients offered by cross-correlation, only the correct separation regions must be selected. The method must select the weak separation regions which produced very low correlation coefficients and must ignore the regions with high correlation coefficients founded within the nuclei. Because of these high variations, the thresholding of the cross-correlation result is very unlikely to provide acceptable results.

The pixels on these separation lines have the property that their grey values are smaller than the grey values of the neighbouring pixels both from the right and the left side. But in the filtered and enhanced cross-correlation result, these pixels receive higher values. We can imagine that these pixels are on a hill (the separation line with high cross-correlation coefficients) with high values and the neighbouring pixels with lower values form two valleys one on the left and another on the right side. The profile of the section has an inverse V shape (Λ).

This judgement helps us to use in a complemented way the “V-shape” method proposed in IV.4.1. The applying process is the same excepting the Eq.IV.7 replaced by Eq.IV.8 [Rogojanu, *et al.*, 2010]:

$$\text{line}\Lambda = (\text{line}\Lambda 0 < n\text{Min}\Lambda\text{pixels}) \vee (\text{line}\Lambda 45 < n\text{Min}\Lambda\text{pixels}) \vee (\text{line}\Lambda 90 < n\text{Min}\Lambda\text{pixels}) \vee (\text{line}\Lambda 135 < n\text{Min}\Lambda\text{pixels}) \quad (\text{IV.8})$$

For the particular example IV.4.1.1, the Eq.IV.5 becomes [Rogojanu, *et al.*, 2010]:

$$\text{line}\Lambda 0_c1 = \left[(I * K_line1_C + nMinOffset) > (I * K_line1_L) \right] \wedge \left[(I * K_line1_C + nMinOffset) > (I * K_line1_R) \right] \quad (\text{IV.9})$$

The FP results are ignored using the same role from IV.4.1.2, by judging their position. The wrong separation regions founded within nuclei are ignored since they cannot ‘touch’ the background, i.e., regions drawn with red in Fig.IV.15 and the TP results are depicted as green.

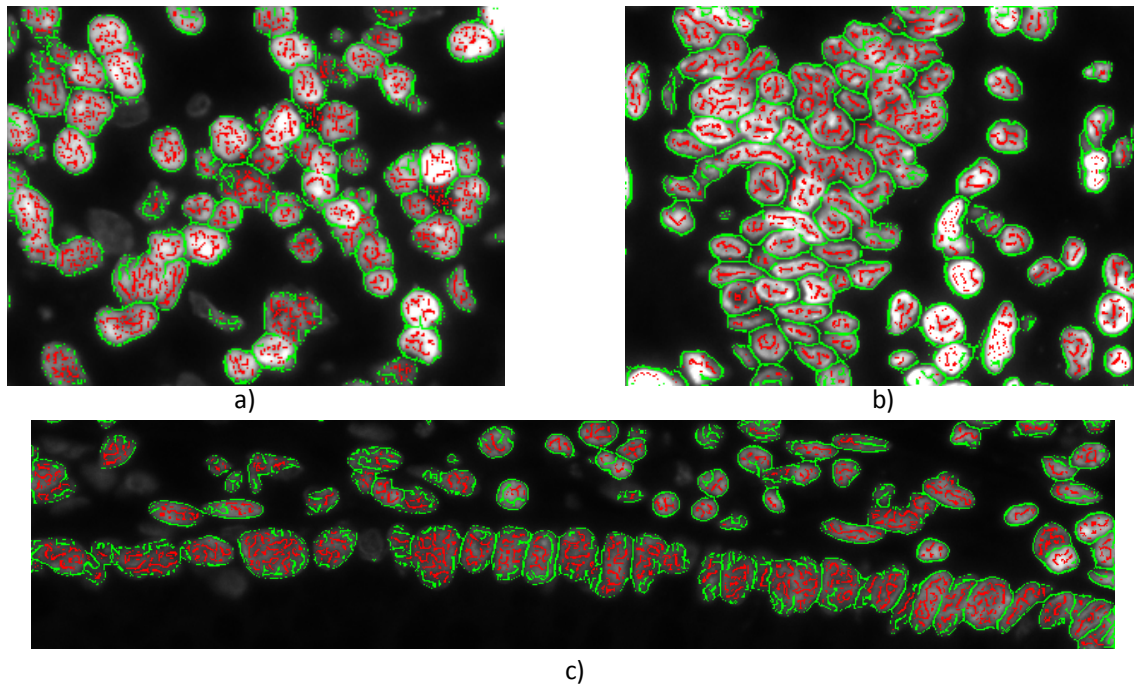


Fig.IV.15 The TP results (drawn with green) are selected based on their link with the background. The FP results (red) within nuclei are ignored since they cannot ‘touch’ the background. [Rogojanu, *et al.*, 2010]

IV.5.3. Watershed on distance transform

In the previous step the inter-nuclei regions that touch the background were selected. In many cases the selected regions surround the nucleus only partially.

To detect the whole nuclei boundaries, the watershed algorithm is applied on the complemented result of the distance transform of a binary image that contains the selected filtered cross-correlation results. A distance transform (or distance map) assigns for each pixel of the image a value which represents the distance to the nearest obstacle pixel (pixel with value ‘1’ from the binary image) [Breu, *et al.*, 1995]. We use the Euclidean distance transform [Danielsson, 1980]. The distance transform will assign big values for the pixels

near the nucleus centre. By complementing the results we will obtain the proper watershed basins which will grow in regions that contain the nuclei.

The watershed algorithm is applied considering as seeds the detected background and the results offered by the extended minima transform. The obtained watershed lines connect the reached repartition lines and delimit regions with only one nucleus. The obtained region contours for the images from Fig.IV.13 are shown with red in Fig.IV.16.

IV.5.4. Results

The proposed segmentation technique was tested on different images of cell nuclei labelled with DAPI from paraffin sections from 8 colorectal G2 tumours with adjacent mucosae out of which four patients had already developed liver metastasis. In some images the nuclei were distributed sparsely throughout the image while in some others they were grouped together.

The obtained region contours for the images from Fig.IV.13 and Fig.IV.17a, b are shown with red in Fig.IV.16 and Fig.IV.17c, d.

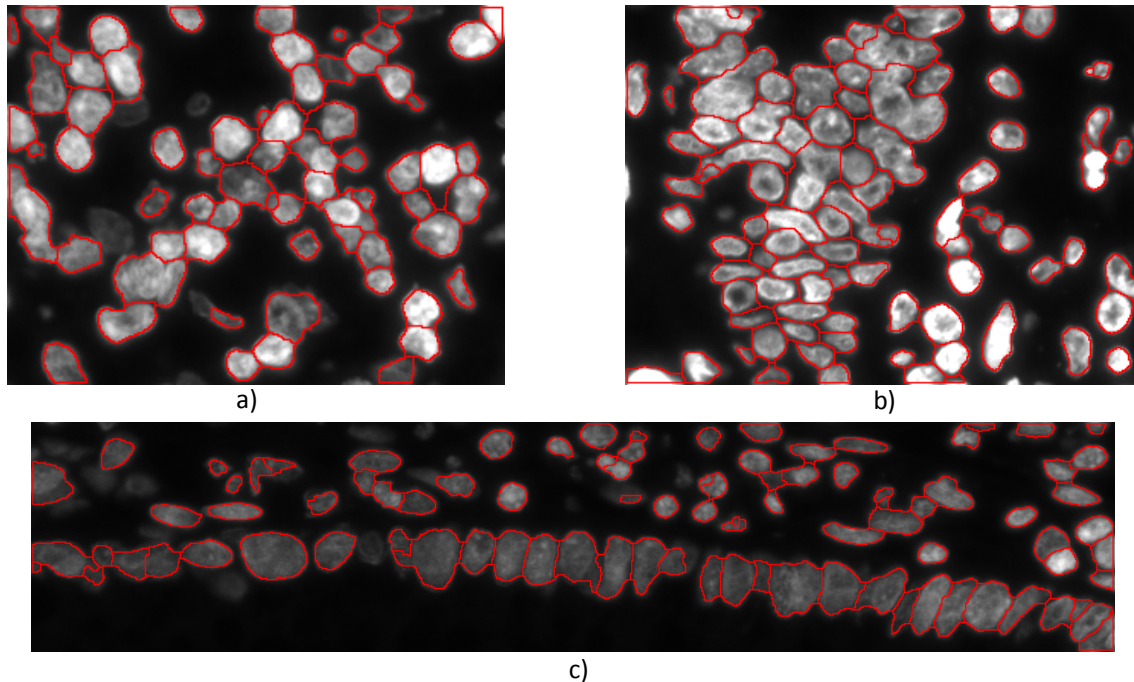


Fig.IV.16 The nuclei boundaries obtained for the images from Fig.IV.13 [Rogojanu, *et al.*, 2010].

IV.5.4.1. Evaluation

The performance of the method was measured by computing the true positive ratio (TPR) and the mis-segmented ratio (MSR) without making any difference between the over- and under-segmented nuclei (III.1.1). We compared the results against ground-truth

segmentations generated by averaging the manual segmentation provided by three human experts in colon cancer sections.

The inspection gave a mean value of 88.37% for the TPR and 12.71% for MSR. These percentages were obtained for 16 selected images containing most complex formations from our database. Over a second set of 40 images with different nuclei configurations we checked the automatic results without making manually the full contours, but by simple cell counting. The percentages found were 91.24% for TPR and 10.18% for MSR.

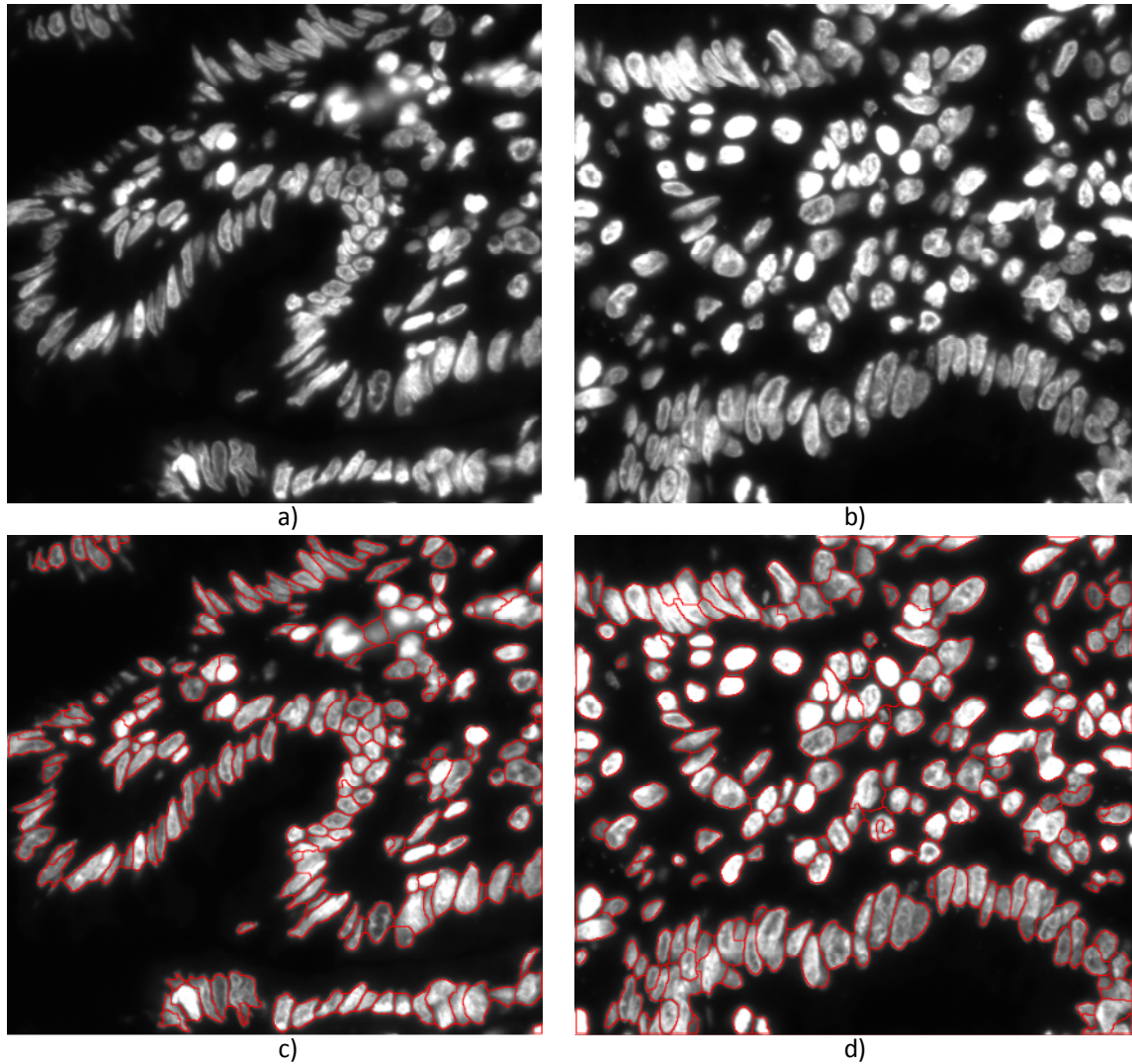


Fig.IV.17 Complex nuclei configurations in tissue sections with colorectal cancer (a, b) and their automatically detected boundaries (c, d) [Rogojanu, *et al.*, 2010].

IV.6. Conclusion

This chapter approaches the segmentation problem of the cell nuclei in colon tissue stained with DAPI in isolated, chained and clustered configurations. The automatic proposed techniques are based on methods which firstly detect the background and then highlight the separation regions between nuclei in order to obtain the complete nuclei boundaries. The segmentation problems encountered in the used images (Fig.IV.1, Fig.IV.13 or Fig.IV.17) were described in I.2.1 and carefully considered in the designing process of the segmentation techniques.

The first common phase for all the methods is the background detection. The two proposed approaches (IV.2), based on thresholding and regions growing, respectively anisotropic diffusion, morphological reconstruction and hysteresis thresholding, provide accurate results and properly deal with the different grey values for the background caused by the non-uniform illumination.

The first method [Smochina, *et al.*, 2010b], [Rogojanu, *et al.*, 2010] grows the regions obtained by thresholding the input image with a small threshold. The thresholding could provide more than one seed to detect the background and the low threshold does not allow the nuclei areas to be selected as seeds.

The second proposed method [Smochina, *et al.*, 2011a] firstly enhances the weak boundaries and reduces the noise by using the anisotropic diffusion. The morphological reconstruction algorithm emphasizes the border between the nuclei and the background, removes many isolated regions/artefacts and homogenizes the grey-scale image. After these pre-processing steps, the hysteresis thresholding easily segments the background.

Three segmentation techniques were presented in this section: one for the particular chained configurations (IV.3) and two for the clustered/touching cell nuclei (IV.4 and IV.5).

The geometrical information was used as *a priori* knowledge to define a set of rules able to highlight the separation regions between chained nuclei (IV.3) [Smochina, *et al.*, 2011a]. This method gives good segmentation results even in situations without any visible clues about the separation regions. The robustness is given by the anisotropic filtering used for noise reduction and boundaries enhancement. The points with high concavity are detected by properly treat the irregular, noise and fluctuating nuclei boundaries. Secondly, a set of rules is used to validate and to pair points so that they indicate the separation regions between cells nuclei. The used set of rules guaranties the detection of the considered situations and do not produce FP results in situations not covered by the used templates. This allows the use (in other fields or with different input images) of this method in combination with techniques designed for other particular situations.

The two techniques proposed for the segmentation of the touching nuclei (IV.4 and IV.5) use two different approaches based on grey level criterion to highlight the separation lines between touching/clustered cell nuclei. The method from IV.4 [Smochina, *et al.*, 2010b] uses a sequence of filters to detect the V shape-like regions; these filters were created considering the profile of the separation sections. The method from IV.5 [Rogojanu, *et al.*, 2010] also considers the pixels intensities distribution within the separation regions but defines a template to characterize small areas from the separation regions; the cross-correlation was used to check the similarity between the template and the image.

Usually these methods produce many FP results due to nuclei with low intensities inside. They are detected and removed by verifying their connectivity with the background detected in the previous phase. The nuclei boundaries with higher intensities “block” the FP regions inside the nuclei to touch the background.

After detecting the separation regions between nuclei using the V-shape method (IV.4), the watershed algorithm is used in two phases; first it is used to ‘fill’ the regions with low intensities within the nuclei and second it detects the nuclei boundaries applied on the reverse image. The compactness descriptor used as merging criterion offers good results but many other more complex criteria can be used. The watershed is also used in IV.5 on the complemented result of the distance transform to obtain the full nuclei boundaries.

The proposed techniques can be extended to any image with human body cells from different tissues types but also in any other field in which the object of interest has the features considered in designing these approaches.

V. Segmentation techniques for histometry

The objective of semantic segmentation in microscopic images is to extract the cellular, nuclear or tissue components. This problem is challenging due to the large variations of these components features (size, shape, orientation or texture).

In this chapter two automatic techniques to robustly identify the epithelial layer (crypts) against interstitial nuclei in microscopic images taken from colon tissues are presented. The relationship between the histological structures (epithelial layer/nuclei, lumen and stroma) and the ring like shape of the crypt are considered.

The same biological data (epithelial layer) is segmented from two different image types taken from the same tissue sample but using different markers. In V.1 and V.2 the DAPI channel is used to detect the epithelial nuclei and in V.3 the cytokeratin-8 highlights the crypts to be segmented. Both proposed methods use the hierarchical approach:

- morphological hierarchy (V.1) [Smochina, *et al.*, 2011b] and its improved version based on morphological pyramid (V.2) [Smochina, *et al.*, 2011d] and
- anisotropic pyramid (V.3) [Smochina, *et al.*, 2011c].

In V.2 the sampling step importance is analysed and a comparison between the hierarchy (without sampling) and the pyramid (with sampling) is presented.

V.1. Epithelial layer segmentation in DAPI stained nuclei images

The crypt inner boundary (the lumen area) is detected using a closing morphological hierarchy and its associated binary hierarchy (V.1.1). The outer border is determined by the epithelial nuclei, overlapped by the maximal isoline of the inner boundary (V.1.2). The evaluation of the proposed method is made by computing the percentage of the mis-segmented nuclei against epithelial nuclei per crypt. The results are discussed and concluded in section V.1.3. An overview scheme of the proposed technique is shown in Fig.V.2 [Smochina, *et al.*, 2011b].

In [Gunduz-Demir, *et al.*, 2010] also the high level information is preferred against the local one but their approach uses different images type (hematoxylin and eosin stained images). These images provide more biological details (also cell cytoplasm is available) than the DAPI stained nuclei images used in this study (e.g. Fig.V.1a).

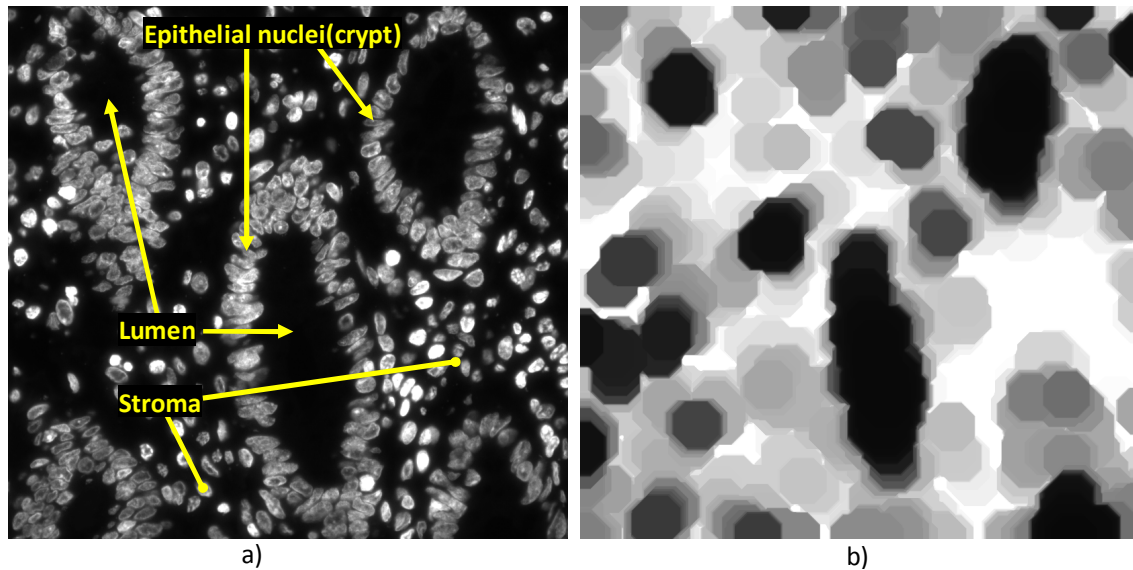


Fig.V.1. a) Fluorescence image with crypts from a colon tissue section. b) The image from the top level of the morphological hierarchy. The black regions indicate the lumen. [Smochina, *et al.*, 2011b]

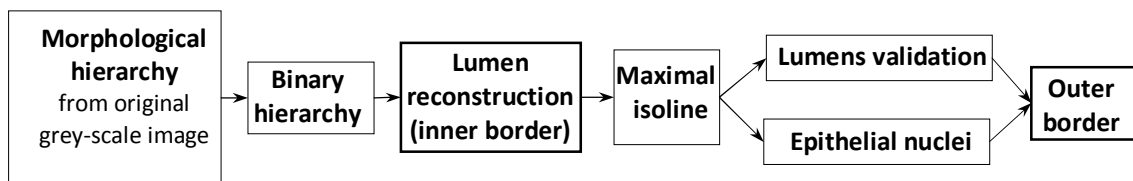


Fig.V.2. Overview scheme of the proposed technique [Smochina, *et al.*, 2011b].

V.1.1. Lumens segmentation using the morphological hierarchy

Without considering the relations between the crypt components (epithelial layer and lumen), the stroma and the background, the low level cues will not be able to separate the regions having a particular meaning [Kropatsch, *et al.*, 2007]. A way must be found to keep only the important information and to remove the unnecessary details. In order to detect these regions, the role of local information (pixel grey values or gradient) is very important but not sufficient; also global information like the region's size and relation with the other region types must be included [Kropatsch, *et al.*, 2007].

A rough assumption about the nuclei distribution over different region types can be made. The lumen does not contain nuclei and appears like a big round black area surrounded by a 'ring' with variable thickness. This ring contains a high density of touched/chained epithelial cells. The exceptional cases appear when the lumen gets to be in touch with the stroma area due to missing cells that 'break' this ring.

By applying the morphological closing operation [Gonzalez and Woods, 1992] on the grey image, the nuclei closer than the size of the structure element (SE) will be connected. The epithelial nuclei and those from the stroma area can be connected by relating the SE's

size to the size of the lumen region (the connection should not pass over the lumen). For that we build the hierarchical image decomposition similar to the morphological pyramid [Haralick, *et al.*, 1987]: the upper levels are obtained by applying a morphological operator on the base image. The difference consists in lack of sub-sampling step [Haralick, *et al.*, 1989].

V.1.1.1. Building the morphological hierarchy

Let I denote the input grey-scale image and “ \bullet ” denote the morphological closing operation. The SE ψ_k is a two-dimensional disk of diameter $2k+1$. The hierarchical morphological representation H_\bullet consists of L levels. The first one is the original grey-scale image $H_\bullet^1 = I$ and each level $\ell > 0$ is given by [Smochina, *et al.*, 2011b]

$$H_\bullet^\ell = H_\bullet^1 \bullet \psi_{2^\ell}, \quad \ell = \overline{1, L} \quad (\text{V.1})$$

The closing operation smoothes the objects’ boundary and removes the dark holes smaller than the SE. Since the size of the SE increases according to the level of the hierarchy, in the lower levels only the small gaps will be filled, while the bigger ones will be closed in the upper levels. To prevent the SE from growing too large, the maximum number of levels is established by limiting the SE’s size so that it covers maximally 2-3 nuclei (in our experiments the SE ψ_{50} gives 25 levels). The lumens should ‘survive’ till the top level (Fig.V.1b) and should be easier highlighted; also the gaps from the crypts (do not exceed the size of 1-2 nuclei) should be filled.

V.1.1.2. Lumen reconstruction

The proper reconstruction of each lumen based on the found regions from the top level must be done by analysing the lower levels of the hierarchy where more details are present. A binary hierarchy H_{bw} is built in which each level represents the result of the thresholding applied on the corresponding level from H_\bullet . The hierarchy H_{bw} consists also of L levels and each level l is given by [Smochina, *et al.*, 2011b]

$$H_{bw}^l = H_\bullet^l < c \cdot thr_{\text{Otsu}}(H_\bullet^l), \quad l = \overline{1, L} \quad (\text{V.2})$$

where $thr_{\text{Otsu}}(\cdot)$ computes the threshold for an image using the Otsu’s method [Otsu, 1979] and $0 < c \leq 1$ (the value 0.5 gives the best results in our experiments).

Our goal is to find for each partition (ancestor) from the top of H_{bw} , the corresponding partition (descendent) from a bottom level which properly identifies the lumen. Each level l

of the H_{bw} contains np_l unconnected regions $H_{bw}^l = \{P_1^l, P_2^l, P_3^l, \dots, P_{np_l}^l\}$. A vertical relation between partitions of successive levels can be established: each partition of a level is included in a partition from the below level (Eq.V.3) [Smochina, *et al.*, 2011b].

$$\forall P_p^l \ (2 \leq l \leq L, 1 \leq p \leq np_l), \ \exists p' \ (1 \leq p' \leq np_{l-1}), \ \text{such that } P_p^l \subset P_{p'}^{l-1} \quad (\text{V.3})$$

This inclusion is valid due to the reduction of the black regions caused by increasing the SE's size used in the closing operation. According to Eq.V.3, for each partition of any level of H_{bw} , the corresponding partition from the base level can be found so that the inclusion rule is validated.

The base level H_{bw}^1 will not give for sure the proper regions because the global threshold is applied on the original image where the main structures are not properly highlighted. For each partition of the top level P_r^L , $1 \leq r \leq np_L$, the corresponding descendent from the base level P_r^1 is obtained. By bottom-up analysing level by level, a certain level l_r is chosen such that the ancestor region ($P_r^{l_r}$) of P_r^1 from level l_r (having as ancestor the P_r^L) checks the following rules [Smochina, *et al.*, 2011b]:

- $\text{solid}(P_r^{l_r}) > \text{min_solidity}$;

The function $\text{solid}(\cdot)$ computes the proportion of the pixels from the convex hull that are also in the region; $\text{min_solidity} = 0.8$ in our experiments.

- $d_E(\text{centroid}(P_r^{l_r}), \text{centroid}(P_r^{l_r-1})) < \text{max_dist}$.

The function $\text{centroid}(\cdot)$ returns the centroid of a region and the $d_E(\cdot)$ computes the Euclidean distance between these two centroids. This rule ensures stability by checking the distance between the regions centroids from two successive levels.

The border of the found lumens actually describes the inner border of the crypt (Fig.V.3a). FP results are eliminated by a validation rule in V.1.2.1.

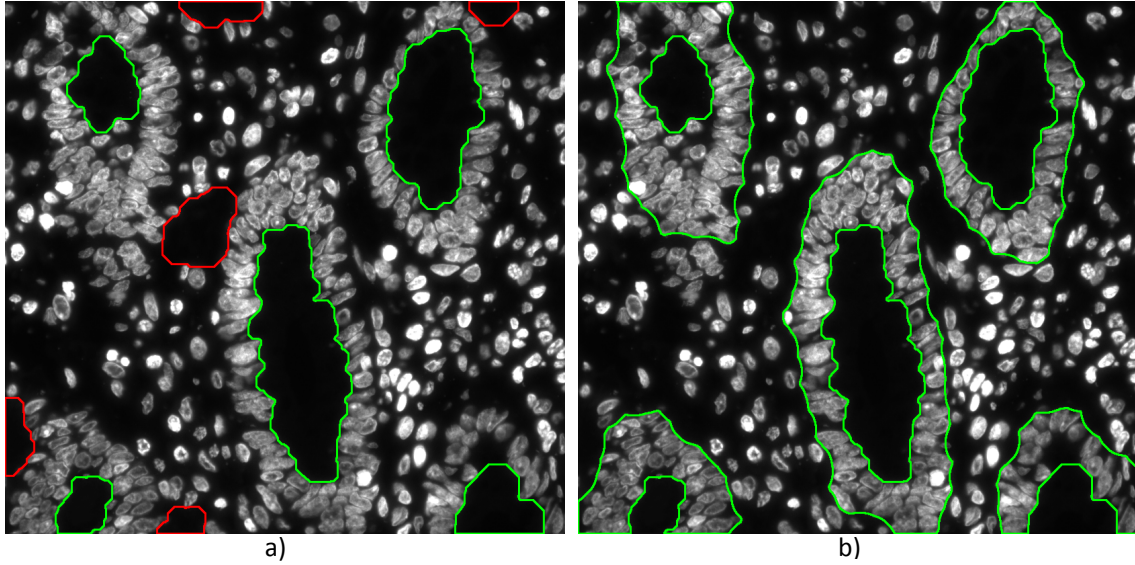


Fig.V.3. a) The TP (green curves) and the FP (red curves) lumen boundaries. b) The green curves indicate the inner and the outer boundaries of the crypts. [Smochina, *et al.*, 2011b]

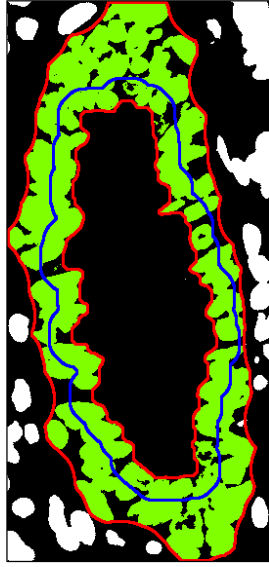
V.1.2. Crypt's outer border

The epithelial layer is differentiated from the stroma areas by considering the nuclei distribution: the crypt's nuclei are packed tightly together while those from the stroma areas are wide spread with considerable distances between them. The isolines of the inner boundary are used to eliminate the FP lumens and to detect the outer border which delineates the epithelial nuclei. Each isoline contains pixels situated on the same distance from the inner boundary.

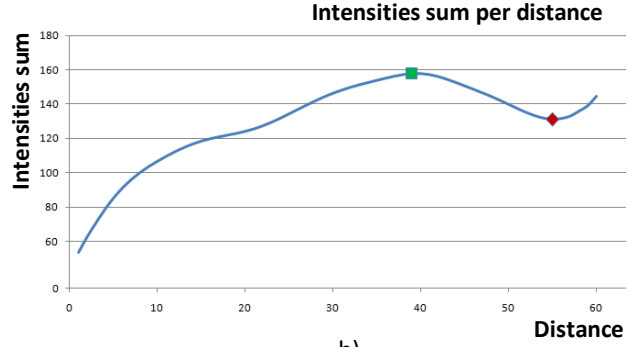
The maximum distance d_{\max} is related to the average width of the epithelial layer (i.e., $d_{\max} = 60$ considering the approximate size of two nuclei). Fig.V.4b displays the smoothed signal containing the intensities sum for each isoline. The maximum value (green square) indicates the isoline which gives the maximum sum of pixels intensities. This maximal isoline (depicted as blue in Fig.V.4a) is used for two purposes: to validate the detected lumens and to mark the epithelial nuclei (used to get the outer boundary).

V.1.2.1. Lumen validation

The area covered by nuclei can be identified by subtracting a highly blurred version from the original image [Smochina, *et al.*, 2011b]: $N_{bw} = (I - G * I) > 0$, where G is a big Gaussian filter (201 by 201 in our experiments). Considering the high nuclei concentration around the lumen, there should be only few situations in which the maximal isoline crosses over the background in N_{bw} (Fig.V.4a), i.e., situations of big distances between epithelial nuclei or in case of crypt breaks.



a)



b)

Fig.V.4. a) The boundaries (red curves) of the crypt from the middle of Fig.V.1a and its maximal isoline (blue curve) which gives the maximum sum of the pixels intensities. b) The smoothed signal containing the intensities sum for each isoline. [Smochina, *et al.*, 2011b]

Based on this, the following rule (Eq.V.4) is proposed to validate the lumen results from V.1.1.2: if the portions of the maximal isoline overlapping the background in N_{bw} are not considerable high compared to those overlapping the nuclei than the found boundary does not delimit a lumen area [Smochina, *et al.*, 2011b].

$$r = \frac{\text{card}(MI \cap \sim N_{bw})}{\text{card}(MI \cap N_{bw})} \quad (\text{V.4})$$

The binary image MI contains the maximal isoline and “ \sim ” gives the complement of a binary image. The FP boundaries ($r > r_{\min}$) are depicted as red in Fig.V.3a and the TP inner boundaries ($r \leq r_{\min}$) with green ($r_{\min} = 0.3$ in our experiments).

V.1.2.2. Outer border detection

A region from N_{bw} is marked as part of a crypt if and only if it is overlapped by the band formed by the inner boundary and the maximal isoline. The epithelial nuclei are depicted as green in Fig.V.4a. The outer border of the crypt (Fig.V.4a the red curve outward) represents the exterior perimeter of the morphological closing applied on the found epithelial nuclei with a SE covering 2-3 nuclei.

V.1.3. Results

The proposed segmentation technique has been tested on different datasets of images from tissues labelled with DAPI; some results are shown in Fig.V.3b and Fig.V.5. The results confirmed that the proposed method could efficiently segment the crypts with a high degree of accuracy.

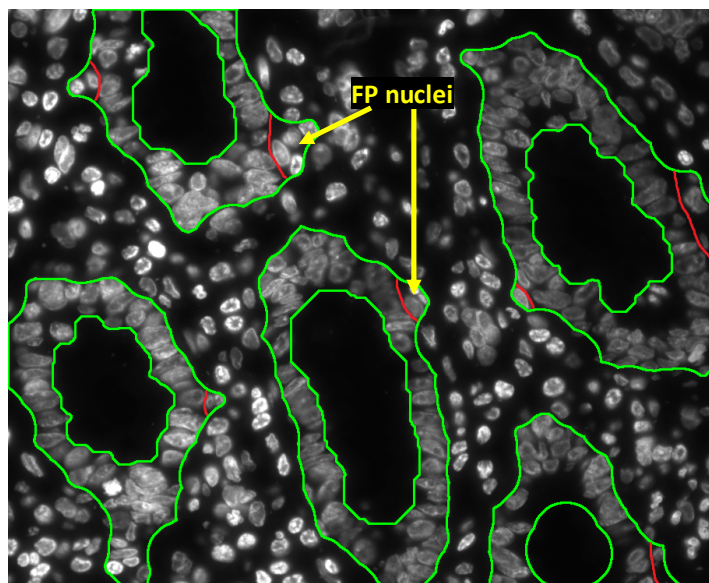


Fig.V.5. The green curves indicate the inner and the outer crypt boundaries. The red portions delimit the FP nuclei. [Smochina, *et al.*, 2011b]

A more rigorous evaluation must be done by comparing the results against the ground truth segmentations. Since a database with reference segmentations for this type of images does not yet exist, a pathologist has been asked to validate a set of results. The segmentation quality is established by visually inspecting the number of the mis-segmented nuclei per crypt. A number of 87 crypts have been analyzed resulting in 284 over-segmented nuclei. Considering an average of 55 nuclei per crypt, the over-segmented nuclei represent 5.93% from the total crypt's nuclei (an average accuracy of 94.07% per crypt).

V.2. Sampling step importance in hierarchical semantic segmentation

In this section the technique presented in V.1 is rigorously analysed in order to find possible points that can be enhanced. The previous technique used to identify the epithelial nuclei (crypt) against interstitial nuclei in microscopic images taken from colon tissues is improved by changing the approach used to detect the crypt inner boundaries. The closing morphological pyramid is used instead of morphological hierarchy. The use of sampling in building the pyramid offers computational efficiency, reduces the amount of used memory, increases the robustness and preserves the quality results. An analysis of the two approaches is

performed considering the number of pixels processed to create each level. Also the relation between the levels of the hierarchical structures is established.

V.2.1. Motivation

In chapter V.1.1.1 the morphologic closing operator was applied on the original image to obtain each level of the hierarchy. Since the closing is an idempotent operation (its reapplication produces no further changes to the previously result) [Haralick, *et al.*, 1989], the size of the SE grows according to the hierarchy levels so that the bigger gaps to be filled in the higher levels. The partitions obtained by thresholding the top level are analysed and reconstructed to obtain the lumens regions using the more detailed information from the lower levels (V.1.1.2).

The previous technique provides stable results [Smochina, *et al.*, 2011b] but presents some solvable problems (p1, p2 and p3). It makes use of a high number of levels (25); each level is actually an image with the same size as the original one. The used memory linearly increases by adding levels to the hierarchy (p1). The closing operator applied with increasing SE increases the computation time for each level as moving to the top of the hierarchy (p2). The top level 25 takes the longest time to be created since the maximum SE (101x101) is used.

A number of N_H^l pixels are accessed and processed to create the level $l > 1$ and N_H pixels to compute the hierarchy H_\bullet with L_H levels [Smochina, *et al.*, 2011d]:

$$N_H^l = w \times h \times (4l)^2 \quad (V.5)$$

$$N_H = \sum_{l=2}^{L_H} N_H^l = 16 \times w \times h \times \left[\frac{L_H(L_H+1)(2L_H+1)}{6} - 1 \right] \quad (V.6)$$

where w and h represent the width and the height of the image ($w = 1392$ and $h = 1024$ in the used images). More than 14.5 trillion pixels are processed to obtain the image from the top level of the hierarchy. In case the size of the images increases, also the computation time needed to obtain each level will increase, especially in the higher levels (p3).

Considering these problems (p1, p2 and p3) another approach must be found to deal more easily with a big amount of data, to reduce the computation time and the used memory but in the same time to preserve or even enhance the quality of the results.

In building the morphological hierarchy, the image size remains constant and the SE's size is increasing. A constant SE can be used on the sub-sampled image to reduce the computation time. This problem gives the suggestion of applying the closing operation in a multiresolution scheme and has been also raised in [Nattkemper, 2005]: "Are the operations

equivalent if we decrease the size of the image or if we increase the size of the structuring element ?”.

A representation structure in which the image size is reduced is the pyramid. The pyramid of an image describes its content at multiple levels of resolution [Kropatsch, *et al.*, 2007]. The type of the pyramid to be chosen is very important for the stability of the final results and must be done according to the application, the type of the image, the properties and relations between images’ regions.

The multiresolution representation has been used with success in image processing and proved their computational efficiency in data representations and processing ([Chen and Lee, 1997], [Tolba, *et al.*, 2003], [Roshni and Raju, 2011]). This stack of images with exponentially decreasing resolutions allows easy access to different resolutions of an image making this a good reason to be used in processing high amount of data.

V.2.2. Lumens segmentation using the morphological pyramid

In building a regular pyramid on an image, the reduction factor r determines the rate by which the number of cells decreases from level to level and the reduction window associates to a pixel from a higher level a set of pixels from the level directly below. E.g., in a 2x2/4 pyramid, the number of cells decreases from level to level by a factor of 4 with a window of 2x2.

Due to the advantages of the morphological closing (V.1.1), the pyramid is generated using this operator. One level of the morphological pyramid (a non-linear multiresolution) [Haralick, *et al.*, 1989] is obtained in two steps: the current level is first morphologically filtered with the SE ψ_{Π} , second the result is sub-sampled to obtain the next level. The input image represents the first level. The morphological pyramid Π_{\bullet} consists of L_{Π} levels and each level $\ell > 0$ is given by [Smochina, *et al.*, 2011d]:

$$\begin{aligned} \Pi_{\bullet}^1 &= I \\ \Pi_{\bullet}^{\ell} &= \left(\Pi_{\bullet}^{\ell-1} \bullet \psi_{\Pi} \right) \downarrow_4, \quad \ell = \overline{2, L_{\Pi}} \end{aligned} \tag{V.7}$$

The \downarrow_4 denotes the sub-sampling process which reduce the image size by four times (halving the w and h). A number of N_{Π}^{ℓ} pixels are accessed to create the level ℓ of the pyramid. To compute the entire pyramid (L_{Π} levels), N_{Π} pixels are accessed. These numbers are computed using the following two equations [Smochina, *et al.*, 2011d]:

$$N_{\Pi}^l = \frac{w}{2^{l-1}} \times \frac{h}{2^{l-1}} \times d^2 \quad (\text{V.8})$$

$$N_{\Pi} = \sum_{l=2}^{L_{\Pi}} N_{\Pi}^l = w \times h \times d^2 \times \left(\frac{1}{2^2} + \frac{1}{2^{2^2}} + \dots + \frac{1}{2^{L_{\Pi}^2}} \right) \quad (\text{V.9})$$

The first levels of the morphological pyramid built on top of the image Fig.V.1a are shown in Fig. V.6.

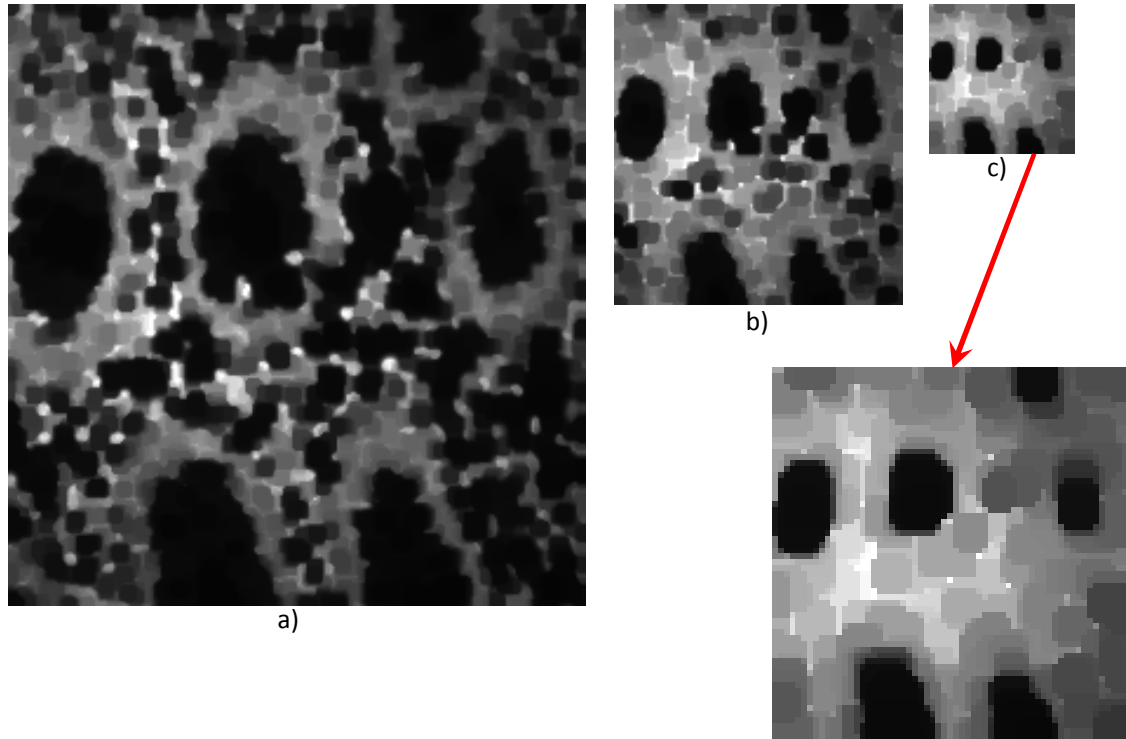


Fig.V.6. The images from the third (a), fourth (b) and fifth (c) level of the morphological pyramid built on top of the image Fig.V.1a. [Smochina, *et al.*, 2011d]

V.2.2.1. Moving from un-sampled to sampled domain

Fig.V.7. shows the difference between the numbers of accessed pixels (NAP) for building the two morphological structures. The NAP decreases exponentially as going to the top levels in the pyramid's case, while for the hierarchy the NAP increases based on a quadratic polynomial.

In this case it is a question if by using this computation efficiency, the quality of the results are the same or even similar with the results offered by [Smochina, *et al.*, 2011b].

The 25th level of the morphological hierarchy gives the proper partitions from which the lumens are reconstructed. Also in case of the pyramid, a suitable resolution level must be

selected. From experimental tests resulted that the 5th level ($w = 87$, $h = 64$) (critical level) is the maximum level of the pyramid which offers the minimum details to extract relevant information.

In order to make the relationship between the morphological closing operation in the sampled (pyramid Π_{\bullet}) and in the un-sampled (hierarchy H_{\bullet}) domain, the level H_{\bullet}^{25} (Fig.V.1b) of the hierarchy must be related with the level Π_{\bullet}^5 (Fig.V.6c) from pyramid; this implies the relation between the SEs ψ_{50} and ψ_{Π} . The unknown ψ_{Π} is obtained by solving the following equation [Smochina, *et al.*, 2011d]:

$$H_{\bullet}^{25} \downarrow_{4^4} \approx \Pi_{\bullet}^5 \rightarrow (H_{\bullet}^1 \bullet \psi_{50}) \downarrow_{4^4} \approx (\Pi_{\bullet}^4 \bullet \psi_{\Pi}) \downarrow_{4^4} \quad (V.10)$$

The SE ψ_{50} was chosen so that it covers maximally 2-3 nuclei. The same rule must be applied for the 5th level of the pyramid so that it provides the proper partitions from which the lumens are reconstructed. Since the image Π_{\bullet}^4 is 4^3 times smaller than the original one, also the size of the SE should be reduced to cover 2-3 ‘smaller’ nuclei.

$$\psi_{\Pi} = \psi_{50} \downarrow_{4^3} = \psi_{50} / 2^3 \approx \psi_7 \quad (V.11)$$

From Eq.V.10 and Eq.V.11 and we derive Eq.V.12 which relate the level l_H of the hierarchy with the level $l+1$ of the pyramid [Smochina, *et al.*, 2011d]:

$$(H_{\bullet}^1 \bullet \psi_{l_H}) \downarrow_{4^l} \approx \left(\Pi_{\bullet}^l \bullet \psi_{\frac{l_H}{2^{l-1}}} \right) \downarrow_{4^l} \quad (V.12)$$

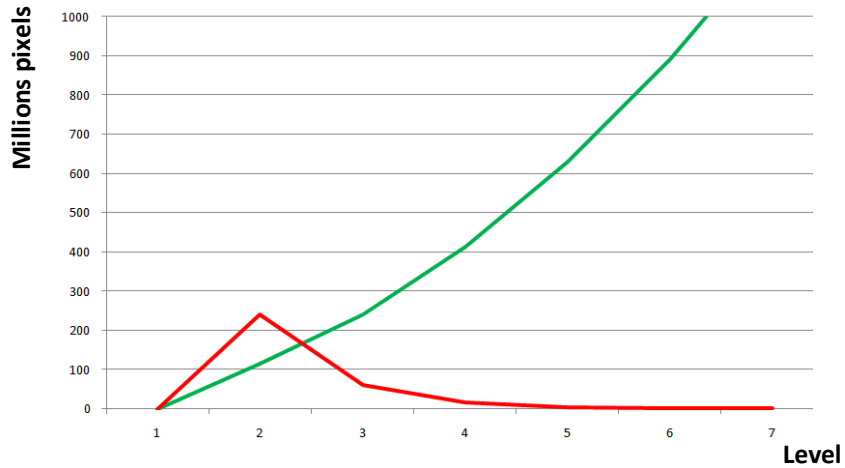


Fig.V.7. The number of pixels accessed per level to compute the morphological pyramid (red) and the morphological hierarchy (green). [Smochina, *et al.*, 2011d]

V.2.2.2. Lumen reconstruction

Similar to V.1.1.2, a binary pyramid Π_{bw} is built in which each level represents the result of the thresholding applied on the corresponding level from Π_{\bullet} . [Smochina, *et al.*, 2011d]:

$$\Pi_{bw}^l = \Pi_{\bullet}^l < c \cdot thr_{Otsu}(\Pi_{\bullet}^l), \quad l = \overline{1, L_{\Pi}} \quad (V.13)$$

In V.1.1.2 for each partition from H_{bw}^{25} the proper lower level must be found so that the corresponding descendent partition properly identifies the lumen. When using the pyramid, the descendent partitions of the Π_{bw}^5 from the level Π_{bw}^3 properly identify the lumens. The FP results are eliminated by a validation rule in V.1.2.1.

V.2.3. Filtering and sampling vs. sampling and filtering

A new level of the pyramid can be obtained using the following two possibilities [Smochina, *et al.*, 2011d]:

- In pyramid Π_1 , the current image is filtered with the SE ψ' and then sub-sampled (used in Eq.V.7)

$$\Pi_1^{l+1} = (\Pi_1^l \bullet \psi') \downarrow_4 \quad (V.14)$$

- In pyramid Π_2 , the current image is sub-sampled before filtering with the SE ψ'' :

$$\Pi_2^{l+1} = (\Pi_2^l \downarrow_4) \bullet \psi'' \quad (V.15)$$

Two questions arise: how different are the two pyramids (Π_1, Π_2) created using the two possibilities if $\psi' = \psi''$ and, if they are different what should be the relation between ψ' and ψ'' such that $\Pi_1^l \approx \Pi_2^l, \forall l$.

The SE ψ' gives the critical level l_c in the case of using Eq.V.14. Considering the case Eq.V.15 and $\psi' = \psi''$, at the level l_c of Π_2 the SE covers 4-5 nuclei instead 2-3 nuclei (in the first case) since ψ'' is applied on the sub-sampled image. This results in over-filling the important regions, e.g., lumens. The ψ'' is applied (in the second case) on an image 4 times smaller than the corresponding image from the first case:

$$\Pi_1^{l-1} \uparrow^4 \approx \Pi_2^l \quad (\text{V.16})$$

If $\Pi_1^l \approx \Pi_2^l$ is desired, then also the size of SE must be reduced, i.e. $\psi'' = \psi' \downarrow_4$ [Smochina, *et al.*, 2011d]. In this case, the SE ψ'' will cover the same area as the SE ψ' .

V.2.4. Results

In Fig.V.8 and Fig.V.9 the inner boundaries from both approaches are drawn: the green interior curves are obtained using the hierarchical morphological approach (detailed in V.1.1), the red interior curves are obtained using the morphological pyramid (V.2.2) and the yellow portions represents the parts where these two results are identical.

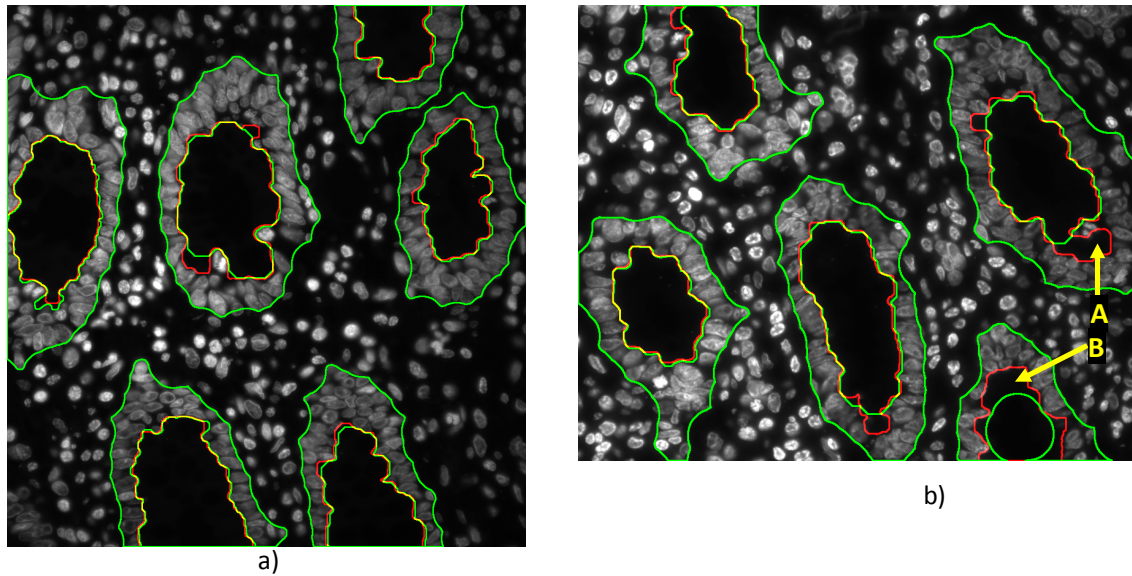


Fig.V.8. The interior boundaries obtained using the morphological hierarchy (green curves) and the pyramid (red curves); the results are identical on the yellow portions. The outer borders are depicted as green. [Smochina, *et al.*, 2011d]

We tested the proposed segmentation techniques on different datasets of images from tissues labelled with DAPI. The results confirmed that the proposed methods could efficiently segment the crypts with a high degree of accuracy.

Even that the computation time and the used memory have been considerably reduced in the proposed approach based on pyramids, the quality of the results has been preserved, i.e. in Fig.V.9 they differ only by a few non-significant pixels. More than that, in many cases the pyramid approach provides even better results, for instance in Fig.V.8b the red curves delimit with higher accuracy the lumens (regions A and B).

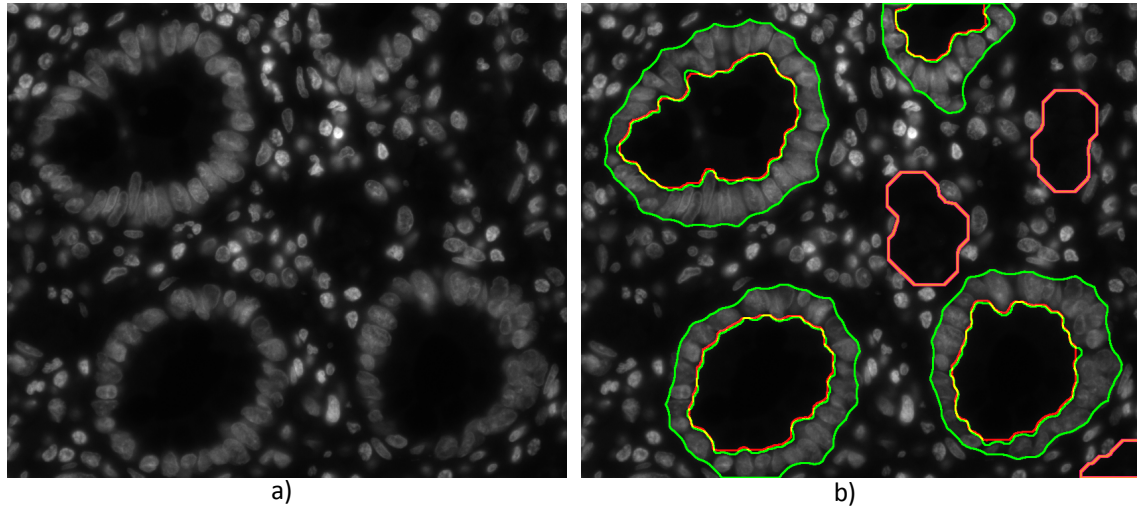


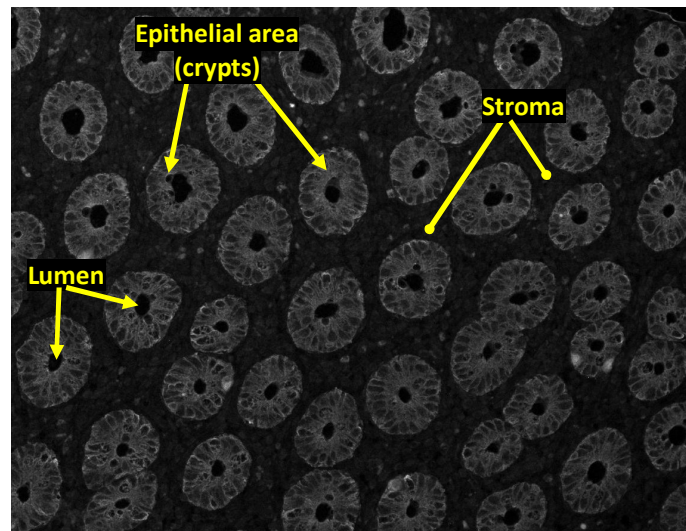
Fig.V.9. The interior boundaries obtained using the morphological hierarchy (green curves) and the pyramid (red curves); the results are identical on the yellow portions. The outer borders are depicted as green. The FP boundaries are depicted as orange. [Smochina, *et al.*, 2011d]

The stability of the segmentation technique has been also improved by eliminating the parameters *min_solidy* and *max_dist* and the two stability rules from V.1.1.2 [Smochina, *et al.*, 2011d]. In V.2.2.2 the lumens are reconstructed by considering the descendent partitions from the third level without any addition analysis and computation time.

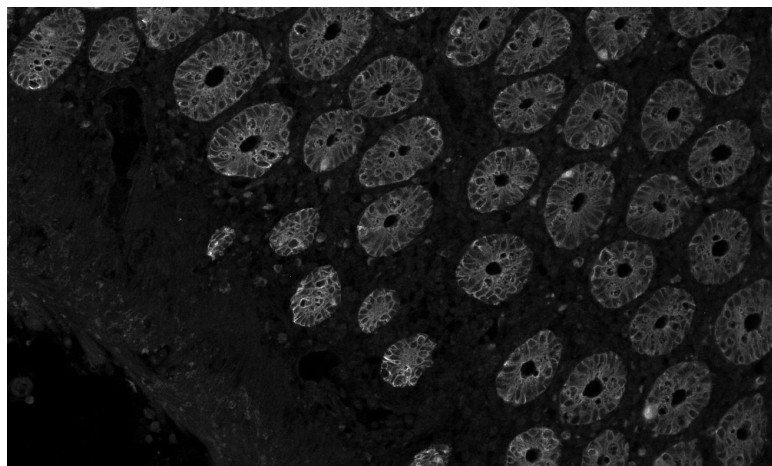
The over-segmented nuclei are the only type of miss-segmented nuclei. They are produced by the approach used to detect the outer-border which wrongly considered the interstitial nuclei as epithelial nuclei. Since the differences between the inner boundaries from the two results do not include miss-segmented nuclei, the outer border detection and the accuracy presented in V.1.3 (i.e., an average accuracy of 94.07% per crypt) are not influenced by the new results.

V.3. Epithelial area detection in cytokeratin microscopic images

In this chapter we describe an automatic technique which robustly delimits the epithelial area (i.e., crypts) in microscopic images taken from colon tissues sections marked with CK-8 (Fig.V.10). An overview scheme of the proposed technique is presented in Fig.V.11. The epithelial area is highlighted using the anisotropic diffusion pyramid (V.3.2.1) and segmented using the MSER+. The crypts separation (V.3.3.1) and lumen detection (V.3.3.2) is performed by imposing topological constraints about the epithelial layer distribution within tissue and the round-like shape of the crypt. The evaluation of the proposed method is made by comparing the results with ground-truth segmentations (V.3.4).



a)



b)

Fig.V.10. Fluorescence grey-scale image showing crypts stained with anti-cytokeratin 8 from colon tissue section.

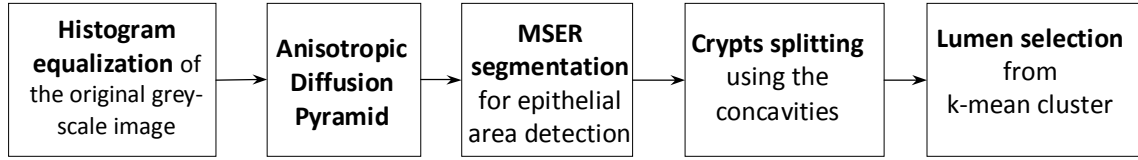


Fig.V.11. Overview scheme of the proposed technique [Smochina, *et al.*, 2011c].

V.3.1. Image enhancement

The CK-8 images are slightly underexposed due to tissue variability and local weak binding of the fluorescence marker. The image contrast can be enhanced such that the separation between the crypts and the stroma is better highlighted. The histogram equalization [Gonzalez and Woods, 1992] is used because it maximizes the image contrast by transforming the values in an intensity image so that the intensities are better distributed on the image histogram.

There are many situations in which some image portions don't contain useful information (Fig.V.10b), i.e. they have low intensities due to the lack of CK-8 signal. Only the set of pixels with higher intensities than a certain threshold are considered in the histogram enhancement process, since they are the result of binding between the CK-8 and epithelial cells. If I denotes the input grey-scale image, the enhanced image is given by [Smochina, *et al.*, 2011c]

$$I_{enh} = \begin{cases} 0, & \text{if } I \leq c \cdot thr_{Otsu}(I) \\ \text{hist_enh}(I | I > c \cdot thr_{Otsu}(I)), & \text{else} \end{cases} \quad (\text{V.17})$$

where c is fixed to 0.5 in our experiments and the function $\text{hist_enh}(\cdot)$ performs the histogram equalization. This technique allows the enhancement of the objects of interest, but keeps the low intensity levels for the background (Fig.V.12).

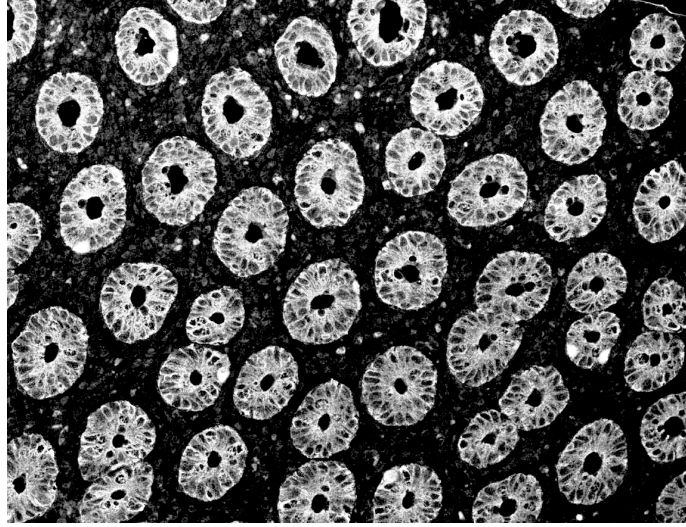


Fig.V.12. The enhanced image of Fig.V.10a by histogram processing; the bright regions indicate the crypts and the inside black regions are the lumens [Smochina, *et al.*, 2011c].

V.3.2. Crypt outer borders detection

The borders detection process must ignore the gaps within crypts. The low level cues (pixels, small areas) don't provide enough information to separate the regions having a particular meaning [Kropatsch, *et al.*, 2007]. A way must be found to keep only the important information and to remove the unnecessary details. In order to detect these regions, the role of local information (pixel grey values or gradient) is very important but not sufficient; also global information like the region's size and relation with the other region types must be included [Kropatsch, *et al.*, 2007].

In [Smochina, *et al.*, 2011b] the morphological closing operator is used in a multiresolution structure; the gaps between nuclei are filled by relating the structure element size to the size of the gaps. This gives good results for images with nuclei, but in our case elements within the stroma near the crypts may be merged by the closing operator. Since an accurate delimitation of the epithelial area is required, the anisotropic filtering is applied to homogenize the crypt regions, fill the inside holes while preserving the (weak) epithelial-stroma edge information.

V.3.2.1. Anisotropic diffusion pyramid

If the conventional spatial filters are used, the edges are blurred up by losing completely necessary information for crypt assessment.

The anisotropic diffusion pyramid (ADP) [Acton, *et al.*, 1994] Π_{γ} consists of L levels. The first level is the enhanced image $\Pi_{\gamma}^1 = I_{enh}$ (width $w = 1392$ and height $h = 1024$) and each level $\ell > 1$ is given by [Smochina, *et al.*, 2011c]

$$\Pi_Y^l = \Upsilon(\Pi_Y^{l-1}) \downarrow_4, \quad \ell = \overline{2, L} \quad (\text{V.18})$$

where the \downarrow_4 denotes the sub-sampling process which reduce the image size by four times (halving the w and h , a scale pyramid with one octave between scale).

Using the ADP, the edge sharpening properties of anisotropic diffusion can be exploited together with the performance of the multiresolution hierarchical process. The anisotropic diffusion smooths the objects' interior and removes the dark holes. The gaps are continually filled by going to the coarser levels of the pyramid.

A resolution level must be selected from this coarse-to-fine representation such that the crypts area is accurately delineated and all gaps filled. From experimental tests resulted that the 4th level ($w = 174$, $h = 128$) (critical level) is the maximum level of the pyramid which offers the minimum details to extract relevant information (Fig.V.15 and Fig.V.17b).

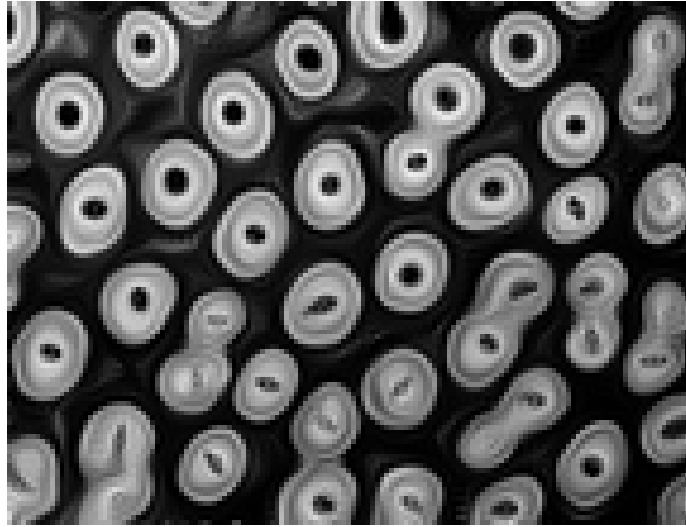


Fig.V.13. The image from the 4th level of the ADP, up scaled to the size of the original image (Fig.V.10a) for better visualization [Smochina, *et al.*, 2011c].

In Fig.V.10c and Fig.V.17b the bright round areas represent the epithelial regions and the interstitial details were spread out between crypts. Due to the anisotropic diffusion, the pixels intensities in the middle of the “donut” decreased because of the small holes. Although the histogram equalization has been applied for image contrast enhancement, the global or adaptive threshold will not offer stable results.

Instead, the MSER is used (II.5.5) on the 4th level of ADP. The best results were obtained by setting the stability range parameter Δ to 15.

The round dark channel within the ‘donut’ causes the MSER to produce more than one stable region per crypt, but they are nested. Since we are interested in only one region per crypt, the final binary result is obtained by considering the union of all MSERs.

$$I_{bw} = \bigcup_{t \in T, i_t \in M_t} R_{i_t}^t \quad (\text{V.19})$$

where T is the set of thresholds values for which a MSER has been found and M_t contains the MSERs for the threshold t .

This approach has been chosen also for its preference for round regions [Kimmel, *et al.*, 2010] given by the affine-invariant property [Matas, *et al.*, 2002]. The regions from Fig.V.15 and Fig.V.17b are homogeneous regions with distinctive boundaries; high detection accuracy especially in these situations has also been concluded in [Mikolajczyk, *et al.*, 2005].

In case of using the pyramid in image segmentation, the proper reconstruction of the regions found on the top levels must be done by analysing the finer lower levels of the hierarchy where more details are present. In our anisotropic diffusion pyramid this is not required due to the anisotropic filtering which preserves (and even enhance) the boundaries between the epithelial areas and stroma.

The borders of the MSERs+ delimit the epithelial areas and actually represent the outer border of the crypt (the green curves in Fig.V.14). The segmentation produces FP results in which two close crypts are detected as a single region (regions A and B in Fig.V.14); the crypts in this situation are rechecked and split in V.3.3.1.

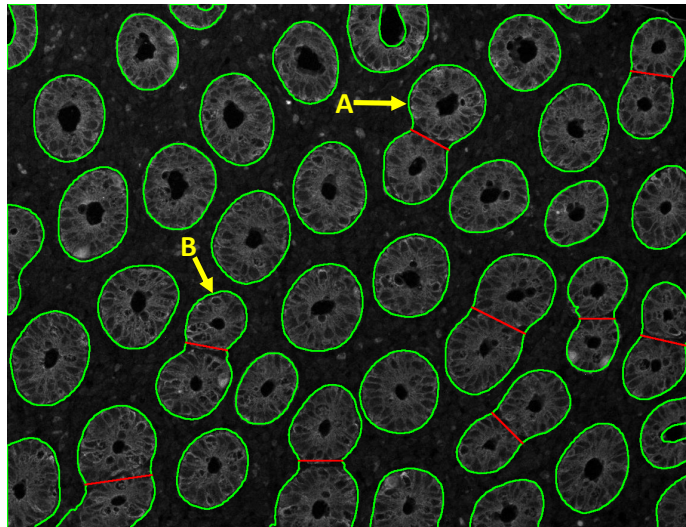


Fig.V.14. The green curves delimit the epithelial regions and the red lines split the FP results with two close crypts (Fig.V.10a) [Smochina, *et al.*, 2011c].

V.3.3. Crypts separation and lumen detection

The anisotropic filtration can shrink or even totally fill the lumen; in these cases the MSER- is not able to give good results and MSER+ is unstable. Before performing the lumen

detection, the touching crypts mis-segmented as a single region are split by considering their geometrical features.

V.3.3.1. Crypts separation

The split of the crypts from a FP result (e.g. regions A, B in Fig.V.14) is made by considering the round-like shape, the size and the concavities near the separation area. The FP results are concave regions and the concavities of these regions give critical information about how the crypts can be separated.

For each region G^i obtained by MSER+, the convex hull G_{convex}^i can be computed. Considering the round shape of the crypt we expect that $G_{convex}^i = G^i$. This is true for the true positive results but for the FP results the difference between the convex hull and the concave region $G_{convex}^i - G^i \neq 0$ offers two regions C_1 and C_2 on both sides of the crypts (depicted as blue in Fig.V.15a). These concavities can be approximated with two triangles and their apexes indicate the entrance into the thin separation area between the two crypts. The separation line is determined by the points $p_{C_1} \in C_1$ and $p_{C_2} \in C_2$ such that the distance $d(p_{C_1}, p_{C_2})$ is minim (pink line in Fig.V.15a). This is a rough separation used for detecting the proper lumen per crypt.

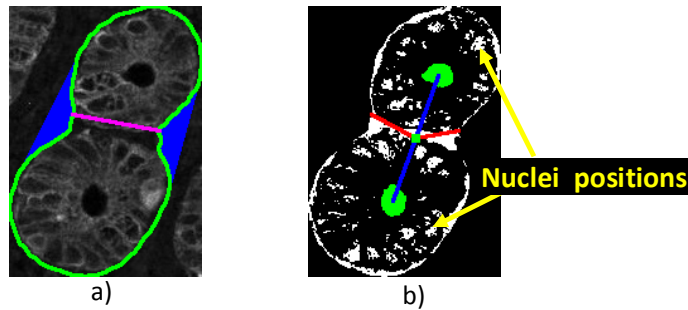


Fig.V.15. a) The pink line approximately separates the crypts. b) The cluster with the lowest values contains the lumens (green regions connected by the blue line) and the white regions; the separation line connects the middle of this line with the two concave points.

[Smochina, *et al.*, 2011c]

V.3.3.2. Lumen detection

The lack of cytokeratins in the cell nuclei produces the dark regions considerable smaller than the lumen. Three intensity classes exist within a found region (from Fig.V.14) corresponding to the i) background and the noisy pixels (lowest intensities), ii) weak cytokeratins binding and iii) strong cytokeratins binding. These classes are detected using the k-means clustering [Gonzalez and Woods, 1992]. The cluster with the lowest values contains the pixels from the lumen and the small dark holes corresponding to the nuclei (Fig.V.15b).

The proper region r_L for lumen is selected by considering its size bigger than the nuclei [Smochina, *et al.*, 2011c].

$$r_L \mid |r_L| = \max \left\{ |r_i|, i = \overline{1, N} \right\} \wedge (|r_L| > a_{\min}) \quad (\text{V.20})$$

where $|\cdot|$ returns the area of a region, N denotes the number of regions from the lowest cluster and a_{\min} is the minimum area of a lumen region. The Fig.V.15b shows the regions from the lowest cluster (white) and the selected regions as lumen (green).

The set of pixels on which the k-means is applied is very important. E.g. in [Gunduz-Demir, *et al.*, 2010], the hematoxylin and eosin images are used for glands detection. The pixels are first quantized into a number of clusters and the cluster corresponding to epithelial layer is further processed in the proposed technique. In our case, even though the image was enhanced so that the intensities are better distributed on the image, the k-mean clustering of the entire image doesn't guarantee good results. Instead, the pixels from the small regions found in Fig.V.14, which cover one or two crypts, are successfully classified into the proper three clusters.

Even though the exact crypt delineation is not needed (more arguments in section V.3.4), the separation line can be better approximated by considering the band width of the crypts. By connecting the middle of the centroids line with the concave points found in V.3.3.1, a better crypt separation is obtained (Fig.V.15b, Fig.V.16). Having better crypt segmentation might enable computing new statistics per crypt once additional markers are used: i.e. percentage of proliferating cells per crypt when staining with a proliferation marker (Ki67).

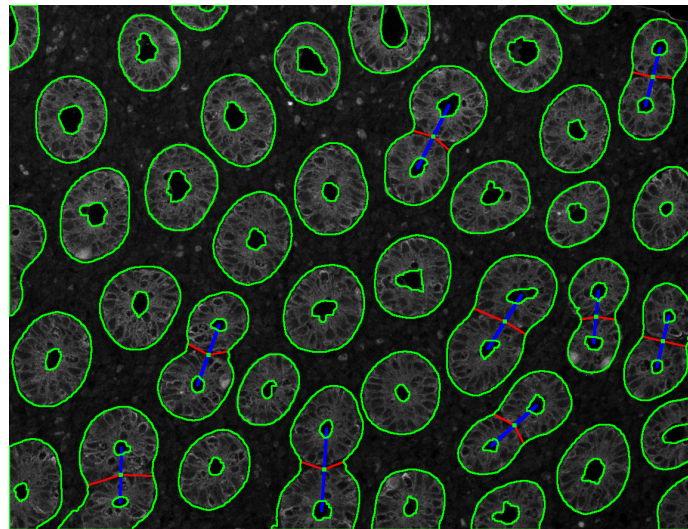


Fig.V.16. The crypts and the lumens boundaries for the image Fig.V.10a are depicted as green.

In case of two touching crypts the blue line connects the lumens centroids and the red lines separate the crypts by connecting the two concave points with the middle of the centroids line. [Smochina, *et al.*, 2011c]

V.3.4. Results

The main issue is to segment the epithelial layer by detecting the area covered by crypts; in the case of two touching/very close crypts the outer boundaries detected in V.3.2 delimit the epithelial cells. An exact segmentation of the pixels within this area is not really necessary, but the number of crypts must be accurately found since it may be used in computing statistics about crypts distribution within colon tissue. We tested the proposed segmentation technique on different datasets of images from CK-8 labelled tissue sections; some results are show in Fig.V.16, Fig.V.17b and Fig.V.18.

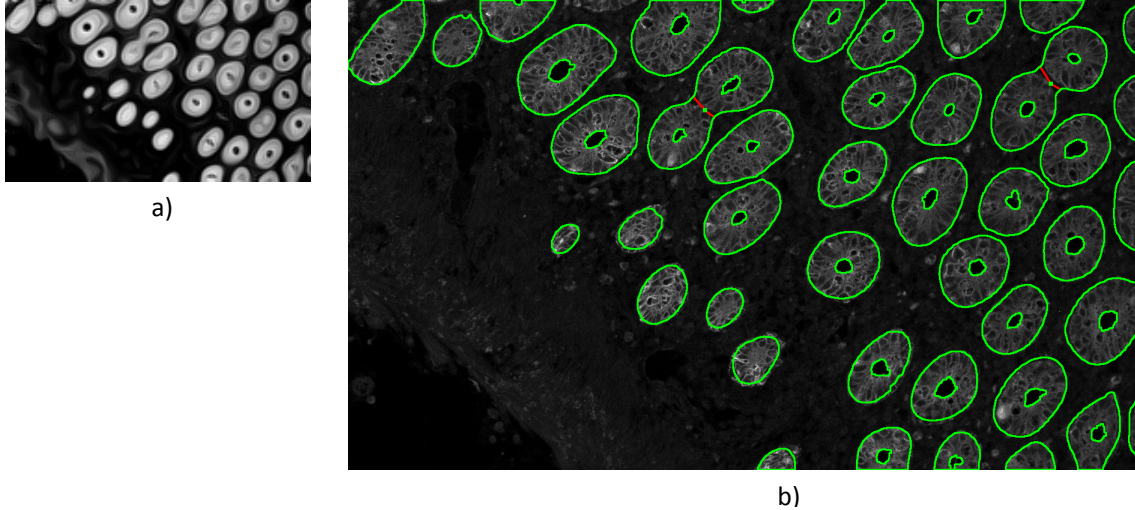


Fig.V.17. a) The image from the 4th level of the ADP, up scaled for better visualization. b) The crypts and the lumens boundaries from the image Fig.V.10b are depicted as green; the red lines separate the touching crypts. [Smochina, *et al.*, 2011c]

A more rigorous evaluation must be done by comparing the results against the ground truth segmentations. Since a database with reference segmentations for this type of images does not yet exist, a human expert has been asked to manually create a set of ground truth segmentations (GTS). The performance of the algorithm is established by determining how far the obtained segmentation is from the GTS.

Using the precision, recall and accuracy measures described in III.1.1, the following results have been obtained by comparing the segmentation of more than 450 crypts: $P = 0.952$, $R = 0.944$ and $A = 0.947$. The results confirmed that the proposed method could efficiently segment the epithelial area with a high accuracy. Since this evaluation is influenced by the accuracy of the crypt boundaries drawn by the expert, a more suitable approach to properly quantify the performance of the algorithm is still a challenge.

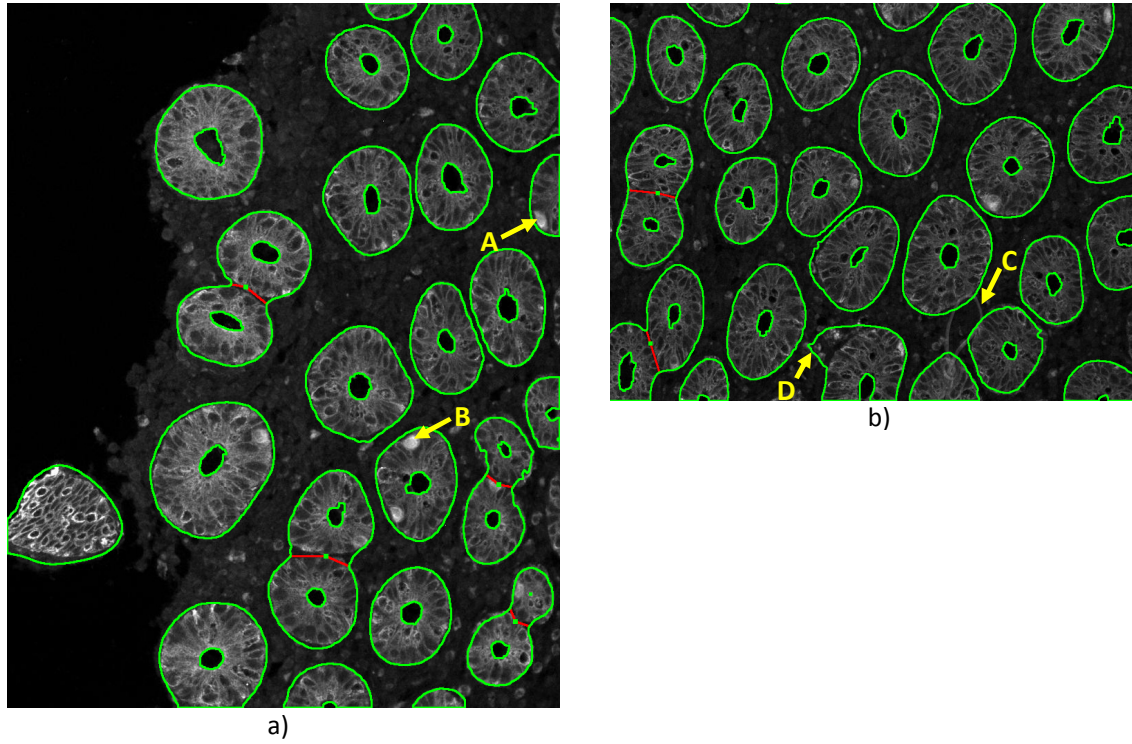


Fig.V.18. The crypts and the lumens boundaries are depicted as green; the red lines separate the touching crypts. In a) the bright spots (regions A and B) were correctly included in the crypt region. In b) region C indicates an artifact overlapping the crypts but eliminated due to ADP. Region D is a case of FP segmentation. [Smochina, *et al.*, 2011c]

V.4. Conclusions

In this chapter two automatic techniques for the crypts/epithelial layer segmentation have been proposed using two image types of colon tissues stained with DAPI and CK-8. Both techniques use different hierarchical representations, i.e., morphological hierarchy (V.1) [Smochina, *et al.*, 2011b] and anisotropic pyramid (V.2) [Smochina, *et al.*, 2011c] having in common the coarse-to-fine approach. A detailed analysis of the hierarchical representations was presented and the importance of the sampling step in building the pyramid has been pointed out (V.3) [Smochina, *et al.*, 2011d]. Based on this comparative study and using the found relation between the levels of the hierarchical structures, the first technique has been improved by using a morphological pyramid instead of a morphological hierarchy [Smochina, *et al.*, 2011d].

In Section V.1 the crypts are segmented from DAPI images [Smochina, *et al.*, 2011b]. Firstly the ‘obvious’ areas like lumens (delimited by the inner border) are detected by employing a hierarchical representation build using the morphological closing operator due to the patterns of nuclei arrangements and its associated binary hierarchy. The isolines of the inner border are used to eliminate the FP results and to get the outer border. A significant implication of this new automatic technique consists of the top-down approach; the high level information is preferred against the local one.

The advantages/disadvantages of this hierarchical representation are analysed in more details in Section V.2 [Smochina, *et al.*, 2011c]. This study highlights the sampling step importance in building the pyramid (e.g., computational efficiency, reduced amount of used memory) and provides the necessary equations to switch from the un-sampled domain (hierarchy) to the sampled domain (pyramid). A suggestive graph with the number of accessed pixels in each level creation for the hierarchy and the pyramid is shown.

The same biological information (crypts) is segmented from CK-8 images using the anisotropic pyramid in Section V.3 [Smochina, *et al.*, 2011d]. In this approach, the edge sharpening properties of the anisotropic diffusion are exploited together with the performance of the multiresolution hierarchical process. After the crypt positions were highlighted, the MSER algorithm segments the critical level of the pyramid where only the important information persisted. The k-means clustering is used to identify the lumens and the geometrical information is used to split the touching crypts.

These techniques uses a coarse-to-fine approach and can be easily extended on any image with epithelial area (crypts) from different tissues types (e.g. prostate, breast or lung) but also in any other field in which the objects of interest have the features considered in designing this method.

VI. Conclusions

This chapter highlights the main contributions presented throughout this thesis. It discusses their strengths and possible improvements and presents several possible directions for future researches related to this work.

VI.1. Contributions

In this dissertation we have presented our contributions in the field of microscopic image analysis, in particular the automatic segmentation of fluorescent images of cell nuclei and crypts, and the evaluation of the segmentation results. The major contributions are related to:

- Segmentation evaluation criteria;
- Image processing techniques used in microscopic image analysis;
- Cell nuclei segmentation within complex arrangement structures;
- Semantic segmentation of the epithelial layer/crypts;
 - The relationship between the sampled and un-sampled domain.

The contributions are summarised below.

VI.1.1. Segmentation evaluation criteria

We have developed a novel segmentation evaluation criterion, adapted for concave objects and able to manage the object-shape similarity importance in the error computation. We have compared this with the state-of-the-art techniques and revealed itself as being the most effective.

The proposed error measure offers two main advantages compared to other quality measures. The first advantage is given by the use of the geodesic distance instead of Euclidean one in computing the distance between the segmentation and the reference curves. The second improvement comes from adding a weighted shape fitting score: the error score contain a tuneable factor which indicates the similarity between the two curves.

VI.1.2. Image processing techniques used in microscopic image analysis

We provide a list of the most used image processing methods and details about how they are usually combined to achieve good segmentation results in the microscopy. This study is helpful for a better use of the existing methods and for improving their performance, as well as for designing new ones. Two main tendencies have been extracted from the analysed papers which seem to provide stable and accurate segmentation results: one based on the geometrical properties of the interest objects used as *a priori* knowledge and the second one based on features extraction used in the training process of a classifier.

VI.1.3. Cell nuclei segmentation within complex arrangement structures

Three segmentation techniques have been proposed to segment the cell nuclei in colon tissue stained with DAPI in isolated, chained and touching/clustered configurations. The automatic proposed techniques are based on methods which firstly detect the background and then highlight the separation regions between nuclei in order to obtain the complete nuclei boundaries.

The accurate background detection is a common step and is performed using two approaches based on thresholding and region growing, respectively anisotropic diffusion, morphological reconstruction and hysteresis thresholding.

The first proposed method employs the geometrical information as *a priori* knowledge to define a set of rules able to highlight the separation regions between chained nuclei. This method gives good segmentation results even in situations without any visible clues about the separation regions by considering the points with high concavity and a set of rules which validate and pair these points.

The other two techniques segment the nuclei using different approaches based on grey level criteria in order to highlight the separation lines between touching/clustered cell nuclei. The first one uses a sequence of filters to detect the V shape-like regions; these filters were created considering the profile of the separation sections. The second one also considers the pixels intensities distribution within the separation regions but defines a template to characterize small areas from the separation regions; the cross-correlation was used to check the similarity between the template and the image.

After the separation regions have been validated, both methods use the watershed algorithm and the compactness descriptor as merging criterion to obtain the full nuclei boundaries.

The proposed techniques can be extended to any image with human body cells from different tissues types but also in any other field in which the object of interest has the features considered in designing these approaches.

The stability and robustness of these methods is given by focusing on the separation regions between nuclei and not on the features of the nuclei. Otherwise, the strong variation of the pixel intensities inside the nuclei as well as features like size, area, orientation, increase the difficulty in developing a segmentation method suitable in all situations.

VI.1.4. Semantic segmentation of the epithelial layer/crypts

We proposed two automatic techniques for the crypts/epithelial layer segmentation using two image types of colon tissues stained with DAPI and CK-8. Both techniques use different hierarchical representations, i.e., morphological hierarchy and anisotropic pyramid having in common the coarse-to-fine approach.

The crypts are segmented from DAPI images. Firstly the ‘obvious’ areas like lumens (inner border) are detected by employing a hierarchical representation build using the morphological closing operator (due to the patterns of nuclei arrangements) and its associated binary hierarchy. The isolines of the inner border are used to eliminate the FP results and to get the outer border. A significant implication of this new automatic technique consists of the top-down approach; the high level information is preferred against the local one.

The same biological information (crypts) is segmented from CK-8 images using the anisotropic pyramid. In this approach, the edge sharpening properties of the anisotropic diffusion are exploited together with the performance of the multiresolution hierarchical process. After the crypt positions were highlighted, the MSER algorithm segments the critical level of the pyramid where only the important information persisted. The k-means clustering is used to identify the lumens; the geometrical information (e.g., convexity) is used to split the touching crypts.

VI.1.4.1. The relationship between the sampled and un-sampled domain

A detailed analysis of the hierarchical representations was presented and the importance of the sampling step in building the pyramid has been pointed out. Based on this comparative study and using the found relations between the levels of the hierarchical structures, the first technique has been improved by using a morphological pyramid instead of a morphological hierarchy.

This study highlights the sampling step importance in building the pyramid (e.g., computational efficiency, reduced amount of used memory) and provides the necessary equations to switch from the un-sampled domain (hierarchy) to the sampled domain (pyramid). A suggestive graphic representation with the number of accessed pixels in each level creation for the hierarchy and the pyramid is shown.

The developed segmentation methods allow automated assessment of crypts in microscopic images from colorectal tissue sections. Areas of epithelium and stroma are properly identified across a statistically relevant image dataset. The developed techniques can be used to assess the areas of epithelium and stroma and their ratios in large tissues sections. The information provided by these measurements allows a better understanding of epithelium-stroma interactions in colon tissue, as well as to confirm the existing qualitative knowledge with new quantitative measurements.

These techniques uses a coarse-to-fine approach and can be easily extended on any image with epithelial area (crypts) from different tissues types (e.g. prostate, breast or lung) but also in any other field in which the objects of interest have the features considered in designing this method.

VI.2. Future research

The encountered problems in this work and especially the obtained results outlined some interesting research directions that can be pursued.

The properly tuning of the parameters for a segmentation algorithm could be achieved by integrating the segmentation evaluation methods within a framework. Given a set of ground-truth segmentations and a discrepancy method, a space of quality scores (the dimensionality is equal to the number of parameters) could be obtained. Different approaches have been tried in this direction by mathematically modelling this unknown space; some good results could be obtained by deeply focusing on this problem.

The cell nuclei segmentation problem has been approached by highlighting the separation regions between nuclei. This approach has been used due to high variations of the nuclei features. A possible and challenging research direction could be the designing and developing of specific classifiers using as training set the ground-truth segmentation provided by the human expert; in this case the features used are critical.

An interesting research implies the use of a different way to represent the image, i.e., to characterize the tissue. For instance, graphs can be build using the segmented objects and by analysing its properties (e.g., topology) to get useful information about the structure, organization, objects (nuclei, cells, crypts) distributions and particular changes on the tissue.

References

- [Acton, *et al.*, 1994] Acton S.T., Bovik A.C., Crawford M.M., *Anisotropic diffusion pyramids for image segmentation*, In Proc. of 1st IEEE International Conference on Image Processing, vol. 3, pp. 478-482, 1994.
- [Angulo, 2008] Angulo J., *Nucleus modelling and segmentation in cell clusters*, Progress in Industrial Mathematics at ECMI'2008, pp. 217-222, 2008.
- [Baggett, *et al.*, 2005] Baggett D., Nakaya M., McAuliffe M., Yamaguchi T.P., Lockett S., *Whole cell segmentation in solid tissue sections*, International Society for Advancement of Cytometry, vol. 67(2)-A, pp. 137-143, 2005.
- [Bai, *et al.*, 2009] Bai X., Sun C., Zhou F., *Splitting touching cells based on concave points and ellipse fitting*, Pattern Recognition, vol. 42(11), pp. 2434-2446, 2009.
- [Bamford and Lovell, 1998] Bamford P., Lovell B.C., *Unsupervised cell nucleus segmentation with active contours*, Journal Signal Processing, vol. 71(2), pp. 203-213, 1998.
- [Beauchemin, *et al.*, 1998] Beauchemin M., Thomson K., Edwards G., *On the Hausdorff distance used for the evaluation of segmentation results*, Canadian Journal of Remote Sensing, vol. 24(1), pp. 3-8, 1998.
- [Begelrnan, *et al.*, 2004] Begelrnan G., Gur E., Rivlin E., Rudzsky M., Zalevsky Z., *Cell nuclei segmentation using fuzzy logic engine*, International Conference on Image Processing, vol.5, pp. 2937-2940, 2004.
- [Boland and Murphy, 2001] Boland M.V., Murphy R.F., *A neural network classifier capable of recognizing the patterns of all major subcellular structures in fluorescence microscope images of HeLa cells*, Bioinformatics, vol. 17(12), pp. 1213-1223, 2001.
- [Boucheron, *et al.*, 2010] Boucheron L.E., Manjunath B.S., Harvey N.R., *Use of imperfectly segmented nuclei in the classification of histopathology images of breast cancer*, IEEE International Conference on Acoustics Speech and Signal Processing, vol. 1, pp. 666-669, 2010.
- [Bowyer, *et al.*, 2001] Bowyer K., Kranenburg C., Dougherty S., *Edge Detector Evaluation Using Empirical ROC Curves*, Computer Vision and

Image Understanding, vol. 84(1), pp. 77–103, 2001.

- [Breu, *et al.*, 1995] Breu H., Gil J., Kirkpatrick D., Werman M., *Linear Time Euclidean Distance Transform Algorithms*, IEEE Transactions on Pattern Analysis and Machine Intelligence, vol. 17(5), pp. 529-533, 1995.
- [Brunelli and Poggio, 1993] Brunelli R., Poggio T., *Face Recognition: Features versus Templates*, IEEE Transactions Pattern Analysis and Machine Intelligence, vol. 15(10), pp. 1042-1052, 1993.
- [Canny, 1986] Canny J., *A computational approach to edge detection*, IEEE Transactions on PAMI, vol.8(6), pp. 679–698, 1986.
- [Carpenter, *et al.*, 2006] Carpenter E.A., Jones R.T., Lamprecht R.M., Clarke C., Kang H.I., Friman O., Guertin A.D., Chang H.J., *Cellprofiler: Image analysis software for identifying and quantifying cell phenotypes*, Genome Biology, vol. 7(10):R100, 2006.
- [Cavallaro, *et al.*, 2002] Cavallaro A., Gelasca E.D., Ebrahimi T., *Objective evaluation of segmentation quality using spatio-temporal context*, In Proc. of the IEEE International Conference on Image Processing, Rochester, New York, pp. 301-304, 2002.
- [Chabrier, *et al.*, 2004] Chabrier S., Laurent H., Emile B., Rosenberger C., Marche P., *A comparative study of supervised evaluation criteria for image segmentation*, In Proc. of the 12th European Signal Processing Conference, Vienna, Austria, pp. 1143-1146, 2004.
- [Chabrier, *et al.*, 2006] Chabrier S., Laurent H., Rosenberger C., Zhang Y.J., *Supervised evaluation of synthetic and real contour segmentation results*, In Proc. of the 14th European Signal Processing Conference, 2006.
- [Chabrier, *et al.*, 2008] Chabrier S., Laurent H., Rosenberger C., Emile B., *Comparative study of contour detection evaluation criteria based on dissimilarity measures*, EURASIP Journal on Image and Video Processing, 13 pages, 2008.
- [Chalana and Kim, 1997] Chalana V., Kim Y., *A methodology for evaluation of boundary detection algorithms on medical images*, IEEE Trans. Med. Imag, vol. 16(5), pp. 642–652, 1997.
- [Chen and Lee, 1997] Chen C.H., Lee G.G., *Image segmentation using multiresolution wavelet analysis and expectation-maximization (EM) algorithm for digital mammography*, International Journal of Imaging Systems and Technology, vol. 8(5), pp. 491-504, 1997.

- [Chen, *et al.*, 2008] Chen Y.T., Hou C.J., Lee M.W., Chen S.J., Tsai Y.C., Hsu T.H., *The image feature analysis for microscopic thyroid tissue classification*, Conf Proc IEEE Eng Med Biol Soc., pp. 4059-4062, 2008.
- [Cheng and Rajapakse, 2009] Cheng J., Rajapakse J.C., *Segmentation of Clustered Nuclei With Shape Markers and Marking Function*, IEEE Transactions on Biomedical Engineering, vol. 56(3), pp. 741-748, 2009.
- [Cloppet and Boucher, 2010] Cloppet F., Boucher A., *Segmentation of complex nucleus configurations in biological images*, Pattern Recognition Letters, vol. 31(8), pp. 755-761, 2010.
- [Coelho, *et al.*, 2009] Coelho L.P., Shariff A., Murphy, R.F., *Nuclear Segmentation in Microscope Cell Images: A Hand-Segmented Dataset and Comparison of Algorithms*, IEEE International Symposium on Biomedical Imaging, pp. 518-521, 2009.
- [Colantonio, *et al.*, 2007] Colantonio S., Salvetti O., Gurevich I.B., *A two-step approach for automatic microscopic image segmentation using fuzzy clustering and neural discrimination*, Pattern Recognition and Image Analysis, vol. 17(3), pp. 428-437, 2007.
- [Cong and Parvin, 2000] Cong G., Parvin B., *Model based segmentation of nuclei*, Pattern Recognition, vol. 33(8), pp. 1383-1393, 2000.
- [Correia and Pereira, 2000] Correia P., Pereira F., *Objective evaluation of relative segmentation quality*, In Proc. of the IEEE International Conference on Image Processing, pp. 308-311, 2000.
- [Dalle, *et al.*, 2009] Dalle J.R., Huang C.H., Leow W.K., Racoceanu D., Putti T.C., *Nuclear pleomorphism scoring by selective cell nuclei detection*, In Proc. IEEE Workshop on Applications of Computer Vision, 2009.
- [Danek, *et al.*, 2009] Danek O., Matula P., Ortiz-de-Solórzano C., Muñoz-Barrutia A., Maška M., Kozubek, M., *Segmentation of touching cell nuclei using a two-stage graph cut model*, Lecture Notes in Computer Science, vol. 5575, pp. 410-419, 2009.
- [Danielsson, 1980] Danielsson P.E., *Euclidean distance mapping*, Computer Graphics and Image Processing, vol. 14, pp. 227-248, 1980.
- [de Kruijf Esther, *et al.*, 2011] de Kruijf Esther M., van Nes Johanna G.H., van de Velde Cornelis J.H., Putter H., Smit Vincent T.H.B.M., Liefers Gerrit J., Kuppen P.J.K., Tollenaar Rob A.E.M., Mesker Wilma E., *Tumor-stroma*

ratio in the primary tumor is a prognostic factor in early breast cancer patients, especially in triple-negative carcinoma patients, Breast cancer research and treatment, vol. 125(3), pp. 687-696, 2011.

- [Donoser and Bischof, 2006] Donoser M., Bischof H., *3D Segmentation by Maximally Stable Volumes (MSVs)*, In Proc. 18th International Conference on Pattern Recognition, vol. 1, pp. 63-66, 2006.
- [Dubuisson and Jain, 1994] Dubuisson M.P., Jain A.K., *A Modified Hausdorff Distance for Object Matching*, In Proc. of the 12th IAPR International Conference on Computer Vision & Image Processing, vol. 1, pp. 566-568, 1994.
- [Dzyubachyk, et al., 2008] Dzyubachyk O., Niessen W., Meijering E., *Advanced level-set based multiple-cell segmentation and tracking in time-lapse fluorescence microscopy images*, 5th IEEE International Symposium on Biomedical Imaging: From Nano to Macro, pp. 185-188, 2008.
- [Everingham, et al., 2002] Everingham M., Muller H., Thomas B.T., *Evaluating Image Segmentation Algorithms Using the Pareto Front*, In Proc. of the 7th European Conference on Computer Vision, Copenhagen, Denmark, pp. 34-48, 2002.
- [Farjam, et al., 2007] Farjam R., Soltanian-Zadeh H., Jafari-Khouzani K., Zoroofi R.A., *An image analysis approach for automatic malignancy determination of prostate pathological images*, Clinical Cytometry, vol. 72B(4), pp. 227-240, 2007.
- [Figueiro, et al., 2003] Figueiro T., Schuch N., Guimarães L.V., Susin A., *A Method for Automatic Detection of Blood Cells on Images using Image Correlation and Connected Components*, In Proc. WICCGPI, São Carlos, Brazil, 2003.
- [Figueiro, et al., 2005] Figueiro T., Schuch N., Soares A., Guimaraes L., Susin A., *Automatic detection of blood cells on color images using image matching and flood map*, Brazilian Symposium on Computer Graphics and Image Processing, 2005.
- [Gonzalez and Woods, 1992] Gonzalez R.C., Woods R.E., *Digital Image Processing*, Reading, Massachusetts: Addison-Wesley 2nd ed., 1992.
- [Goumeidane, et al., 2003] Goumeidane A.B., Khamadja M., Belaroussi B., Benoit-Cattin H., Odet C., *New discrepancy measures for segmentation evaluation*,

- In Proc. of the IEEE International Conference on Image Processing, vol. 3, pp. II-411-14, 2003.
- [Guimarães, *et al.*, 2000] Guimarães L.V., Suzim A.A., Maeda J., *A New Automatic Circular Decomposition Algorithm Applied to Blood Cell Images*, In Proceedings of IEEE Int. Conf. on Bio-Informatics & Biomedical, Washington, pp. 277-280, 2000.
- [Gunduz-Demir, *et al.*, 2010] Gunduz-Demir C., Kandemir M., Tosun A.B., Sokmensuer C., *Automatic segmentation of colon glands using object-graphs*, Medical Image Analysis, vol. 14(1), pp. 1-12, 2010.
- [Haralick, *et al.*, 1987] Haralick R., Lee J., Lin C., Zhuang X., *Multi-resolution Morphology*, In First IEEE conference on Computer Vision, London, 1987.
- [Haralick, *et al.*, 1989] Haralick R.M., Zhuang X., Lin C., Lee J.S.J., *The digital morphological sampling theorem*, IEEE Trans. Acoust., Speech, Signal Processing, vol. 37, pp. 2067-2090, 1989.
- [Herghelegiu, *et al.*, 2010] Herghelegiu P., **Smochina C.**, Manta V., *GPU method for registering multiple MRI sequences*, In Journal Buletinul Institutului Politehnic din Iasi, Automatic Control and Computer Science, Tom LVI(LX), fasc. 4, pp. 175-183, 2010.
- [Hu, *et al.*, 2004] Hu M., Ping X., Ding Y., *Automated cell nucleus segmentation using improved snake*, International Conference on Image Processing, vol. 4, pp. 2737-2740, 2004.
- [Humphries and Wright, 2008] Humphries A., Wright N.A., *Colonic Crypt Organization and Tumorigenesis: Human Colonic Crypts*, In Nature Reviews Cancer, vol. 8(6), pp. 415-424, 2008.
- [Jeong, *et al.*, 2009] Jeong M.R., Ko B.C., Nam J.Y., *Overlapping nuclei segmentation based on Bayesian networks and stepwise merging strategy*, Journal of Microscopy, vol. 235(2), pp. 188–198, 2009.
- [Jiang, *et al.*, 2006] Jiang X., Marti C., Irniger Ch., Bunke H., *Distance measures for image segmentation evaluation*, EURASIP Journal on Applied Signal Processing, vol. 2006, pp. 1–10, 2006.
- [Jung and Kim, 2010] Jung C., Kim C., *Segmenting Clustered Nuclei Using H-minima Transform-Based Marker Extraction and Contour Parameterization*, In IEEE Trans Biomed Eng., vol. 57(10), pp. 2600-2604, 2010.

- [Kapuściński and Skoczylas, 1978] Kapuściński J., Skoczylas B., *Fluorescent complexes of DNA with DAPI 4',6-diamidine-2-phenyl indole.2HCl or DCI 4',6-dicarboxyamide-2-phenyl indole*, Nucleic Acids Res., vol. 5(10), pp. 3775–3799, 1978.
- [Kimmel, *et al.*, 2010] Kimmel R., Zhang C., Bronstein A.M., Bronstein M.M., *Are MSER features really interesting?*, IEEE Trans. PAMI in press 2010.
- [Kononenko, 2001] Kononenko I., *Machine learning for medical diagnosis: History, State of the Art and Perspective*, Artificial Intelligence in Medicine, vol. 23(1), pp. 89-109, 2001.
- [Kropatsch, *et al.*, 2007] Kropatsch W.G., Haxhimusa Y., Ion A., *Multiresolution Image Segmentations in Graph Pyramid*, Applied Graph Theory in Computer Vision and Pattern Recognition, vol. 52, pp. 3-41, 2007.
- [Laurain, *et al.*, 2005] Laurain V., Ramoser H., Nowak C., Steiner G., Ecker R., *Fast automatic segmentation of nuclei in microscopy images of tissue sections*, In Proc. IEEE Engineering in Medicine and Biology Society, vol. 4, pp. 3367-3370, 2005.
- [Lebrun, *et al.*, 2007] Lebrun G., Charrier C., Lezoray O., Meurie C., Cardot H., *A fast and efficient segmentation scheme for cell microscopic image*, Cellular and molecular biology, vol. 53(2), pp. 51-61, 2007.
- [Lewis, 1995] Lewis J.P., *Fast template matching*, in Proc. Vision Interface, pp. 120–123, 1995.
- [Ling and Jacobs, 2007] Ling H., Jacobs D.W., *Shape Classification Using the Inner-Distance*. IEEE Transactions on Pattern Analysis and Machine Intelligence, vol. 29(2), pp. 286–299, 2007.
- [Lopez, *et al.*, 1999] Lopez A.M., Lumbreras F., Serrat J., Villanueva J.J., *Evaluation of methods for ridge and valley detection*, IEEE Trans. Pattern Analysis and Machine Intelligence, vol. 21(4), pp. 327–335, 1999.
- [Madhloom, *et al.*, 2010] Madhloom H.T., Kareem S.A., Ariffin H., Zaidan A.A., Alanazi H.O., Zaidan B.B., *An automated white blood cell nucleus localization and segmentation using image arithmetic and automatic threshold*, Journal of Applied Sciences, vol. 10(11), pp. 959-966, 2010.
- [Malpica and de Solorzano, 2002] Malpica N., de Solorzano C.O., *Automated nuclear segmentation in fluorescence microscopy*, Science, Technology and Education of

Microscopy: an Overview, vol. 2, pp. 614-621, 2002.

- [Malpica, *et al.*, 1997] Malpica N., Solórzano C.O., Vaquero J.J., Santos A., Vallcorba I., García-Sagredo J.M., del Pozo F., *Applying watershed algorithms to the segmentation of clustered nuclei*, Cytometry, vol. 28(4), pp. 289-297, 1997.
- [Matas, *et al.*, 2002] Matas J., Chum O., Urban M., Pajdla T., *Robust wide baseline stereo from maximally stable extremal regions*, In Proc. BMVC, pp. 384-393, 2002.
- [Meftah, *et al.*, 2010] Meftah B., Lezoray O., Lecluse M., Benyettou A., *Cell microscopic segmentation with spiking neuron networks*, International Conference on Artificial neural networks, vol. 6352, pp. 117-126, 2010.
- [Mezaris, *et al.*, 2003] Mezaris V., Kompatsiaris I., Strintzis M.G., *Still image objective segmentation evaluation using ground truth*, In Proc. of the 5th Workshop on Information and Knowledge Management for Integrated Media Communication, pp. 9-14, 2003.
- [Mikolajczyk, *et al.*, 2005] Mikolajczyk K., Tuytelaars T., Schmid C., Zisserman A., Matas J., Schaffalitzky F., Kadir T., Van Gool L., *A comparison of affine region detectors*, International Journal of Computer Vision, vol. 65, pp. 43-72, 2005.
- [Moll, *et al.*, 2008] Moll R., Divo M., Langbein L., *The human keratins: biology and pathology*, Histochemistry and Cell Biology, Springer-Verlag, vol. 129(6), pp. 705-733, 2008.
- [Montero, 2009] Montero R.S., *State of the Art of Compactness and Circularity Measures*, International Mathematical Forum, vol. 4(27), pp. 1305 – 1335, 2009.
- [Morales, *et al.*, 1995] Morales A., Acharya R., Ko S.J., *Morphological Pyramids with Alternating Sequential Filters*, IEEE Transactions on Image Processing, vol. 4(7), pp. 965-977, 1995.
- [Morikawa and Morikawa, 1981] Morikawa K., Yanagida J., *Visualization of individual DNA molecules in solution by light microscopy: DAPI staining method*, Japanese Biochemical Society, vol. 89(2), pp. 693-696, 1981.
- [Mosaliganti, *et al.*, 2009] Mosaliganti K., Gelas A., Gouaillard A., Megason S.G., *Tissue level segmentation and tracking of biological structures in microscopic images based on density maps*, Proc IEEE Int Symp Biomed Imaging, pp.1354-1357, 2009.

- [Naik, *et al.*, 2007] Naik S., Doyle S., Feldman M., Tomaszewski J., Madabhushi A., *Gland segmentation and computerized Gleason grading of prostate histology by integrating low-, high-level and domain specific information*, In 2nd MICCAI Workshop Microscopic Image Analysis with Appl. in Biology, Piscataway, 2007.
- [Naik, *et al.*, 2008] Naik S., Doyle S., Agner S., Madabhushi A., Feldman M.D., Tomaszewski J., *Automated gland and nuclei segmentation for grading of prostate and breast cancer histopathology*, In Proceedings of 5th IEEE International Symposium on Biomedical Imaging, pp. 284-287, 2008.
- [Nattkemper, 2005] Nattkemper T.W., *Automatic segmentation of digital micrographs: A survey*, Journal Studies in health technology and informatics, vol. 107(2), pp. 847-852, 2005.
- [Nedzved, *et al.*, 2000] Nedzved A., Ablameyko S., Pitas I., *Morphological segmentation of histology cell images*, 15th International Conference on Pattern Recognition, pp. 1500, 2000.
- [Nilsson and Heyden, 2005] Nilsson B., Heyden A., *Segmentation of complex cell clusters in microscopic images: application to bone marrow samples*, Cytometry, vol. 66(1), pp. 24-31, 2005.
- [Nixon and Aguado, 2002] Nixon M.S., Aguado A.S., *Feature Extraction & Image Processing*, Elsevier Ltd., 2002.
- [Odet, *et al.*, 2002] Odet C., Belaroussi B., Benoit-Cattin H., *Scalable discrepancy measures for segmentation evaluation*, In Proc. of the IEEE International Conference on Image Processing, Rochester, pp. 785-788, 2002.
- [Otsu, 1979] Otsu N., *A Threshold Selection Method from Gray-Level Histograms*, In IEEE Transactions on Systems, Man, and Cybernetics, vol. 9(1), pp. 62-66, 1979.
- [Palacios and Beltrán, 2007] Palacios G., Beltrán J.R., *Cell nuclei segmentation combining multiresolution analysis*, Clustering Methods and Colour Spaces, International Machine Vision and Image Processing Conference, pp. 91-97, 2007.
- [Pinheiro and Facon, 2005] Pinheiro R.J.G., Facon J., *Measuring the quality evaluation for image segmentation*, In Proc. 10th Iberoamerican Congress on Pattern Recognition, Havana, Cuba, pp. 120-127, 2005.

- [Polak, *et al.*, 2009] Polak M., Zhang H., Pi M., *An evaluation metric for image segmentation of multiple objects*, Image and Vision Computing, vol. 27(8), pp. 1223-1227, 2009.
- [Pratt, 2001] Pratt W.K., *Digital Image Processing*, 3rd ed., Wiley Interscience, NY, 2001.
- [Pratt, *et al.*, 1978] Pratt W.K., Faugeras O.D., Gagolowicz A., *Visual discrimination of stochastic texture fields*, IEEE Transactions on Systems, Man and Cynernetics, vol. 8(11), pp. 796–804, 1978.
- [Rijsbergen, 1979] Rijsbergen C.V. van, *Information retrieval*, Butterworth-Heinemann Newton, MA, USA, 1979.
- [Rogojanu, *et al.*, 2010] Rogojanu R., Bises G., **Smochina C.**, Manta V., *Segmentation of cell nuclei within complex configurations in images with colon sections*, In Proc. IEEE 6th International Conference on Intelligent Computer Communication and Processing, pp. 243-246, 2010.
- [Roman-Roldan, *et al.*, 2001] Roman-Roldan R., Gomez-Lopera J.F., Atae-Allah C., Martinez-Aroza J., Luque-Escamilla P.L., *A measure of quality for evaluating methods of segmentation and edge detection*, Pattern Recognition, vol. 34(5), pp. 969-980, 2001.
- [Roshni and Raju, 2011] Roshni V.S., Raju G., *Image segmentation using multiresolution texture gradient and watershed algorithm*, International Journal of Computer Applications, vol. 22(5), pp. 21-28, 2011.
- [Russell, *et al.*, 2009] Russell R.A., Adams N.M., Stephens D.A., Batty E., Jensen K., Freemont P.S., *Segmentation of Fluorescence Microscopy Images for Quantitative Analysis of Cell Nuclear Architecture*, Biophysical Journal, vol. 96(8), pp. 3379-3389, 2009.
- [Scharr and Weickert, 2000] Scharr H., Weickert J., *An anisotropic diffusion algorithm with optimized rotation invariance*, German Association for Pattern Recognition, pp. 460–467, 2000.
- [Smochina and Manta, 2008] **Smochina C.**, Manta V., *Industrial inspection system using triangulation*, In Journal Buletinul Institutului Politehnic din Iasi, Tom LVI(LVIII), fasc. 3-4, Automatic Control and Computer Science, pp. 75-82, 2008.
- [Smochina, *et al.*, 2010a] **Smochina C.**, Manta V., Rogojanu R., *New discrepancy measure for evaluation of segmentation quality*, In Proc. 11th IASTED International Conference on Computer Graphics and Imaging,

track 679-053, 2010.

- [Smochina, *et al.*, 2010b] **Smochina C.**, Manta V., Bises G., Rogojanu R., *Automatic cell nuclei detection in tissue sections from colorectal cancer*, In Proc. 14th International Conference on System Theory and Control, pp. 519-524, 2010.
- [Smochina, *et al.*, 2011a] **Smochina C.**, Serban A., Manta V., *Segmentation of cell nuclei within chained structures in microscopic images of colon sections*, In Proc. 27th Spring conference on Computer Graphics, pp. 146-154, 2011.
- [Smochina, *et al.*, 2011b] **Smochina C.**, Manta V., Kropatsch W.G., *Semantic segmentation of microscopic images using a morphological hierarchy*, In Proc. 14th International Conference on Computer Analysis of Images and Patterns, LNCS 6854, pp. 102-109, 2011.
- [Smochina, *et al.*, 2011c] **Smochina C.**, Rogojanu R., Manta V., Kropatsch W.G., *Epithelial area detection in cytokeratin microscopic images using MSER segmentation in anisotropic pyramid*, In Proc. 6th IAPR International Conference on Pattern Recognition in Bioinformatics, LNBI 7036, pp. 318, 2011.
- [Smochina, *et al.*, 2011d] **Smochina C.**, Manta V., Kropatsch W.G., *Sampling step importance in hierarchical semantic segmentation of microscopic images*, In Proc. 15th International Conference on System Theory and Control, pp. 570, 2011.
- [Smochina, *et al.*, 2011e] **Smochina C.**, Herghelegiu P., Manta V., *Image processing techniques used in microscopic image segmentation*, In Journal Buletinul Institutului Politehnic din Iasi, Automatic Control and Computer Science, Tom LVII (LXI), fasc. 2, pp. 83-98, 2011.
- [Soille, 2001] Soille P., *Morphological Image Analysis Principles & Applications*, Springer, 2nd ed., 2001.
- [Solorzano, *et al.*, 1999] Solorzano C.O., Rodriguez G., Jones A., Pinkel D., Gray J.W., Sudar D., Lockett S., *Segmentation of confocal microscope images of cell nuclei in thick tissue sections*, Journal of Microscopy, vol. 193(3), pp. 212-226, 1999.
- [Srinivasa, *et al.*, 2009] Srinivasa G., Fickus M.C., Guo Y., Linstedt A.D., Kovacević J., *Active mask segmentation of fluorescence microscope images*, IEEE Transactions on Image Processing Volume, vol. 18(8), pp. 1817-1829, 2009.

- [Ta, *et al.*, 2009] Ta V.T., Lezoray O., El Moataz A., Schupp S., *Graph-based tools for microscopic cellular image segmentation*, Pattern Recognition, vol. 42(6), pp. 1113-1125, 2009.
- [Todman and Claridge, 1997] Todman A., Claridge E., *IntroCell segmentation in histological images of striated muscle tissue reduction – a perceptual grouping approach*, In Proceedings of Medical Image Understanding and Analysis, 1997.
- [Tolba, *et al.*, 2003] Tolba M.F., Mostafa M.G., Gharib T.F., Salem M.A., *MR-Brain image segmentation using gaussian multiresolution analysis and the EM algorithm*. In Proc. ICEIS (2), pp. 165-170, 2003.
- [Velliste and Murphy, 2002] Velliste M., Murphy R.F., *Automated determination of protein subcellular locations from 3D fluorescence microscope images*, IEEE International Symposium on In Biomedical Imaging, pp. 867-870, 2002.
- [Vincent, 1993] Vincent L., *Morphological Grayscale Reconstruction in Image Analysis: Applications and Efficient Algorithms*, IEEE Transactions on Image Processing, vol. 2(2), pp. 176-201, 1993.
- [Wahlby, *et al.*, 2004] Wahlby C., Sintorn I.M., Erlandsson F., Borgefors G., Bengtsson E., *Combining intensity, edge and shape information for 2D and 3D segmentation of cell nuclei in tissue sections*, Journal of Microscopy, vol. 215(1), pp. 67–76, 2004.
- [Wang, *et al.*, 2008] Wang M., Zhou X., Li F., Huckins J., King R.W., Wong S.T., *Novel cell segmentation and online SVM for cell cycle phase identification in automated microscopy*, Bioinformatics, vol. 24(1), pp. 94-101, 2008.
- [Wei, *et al.*, 2011] Wei W.Y., Li Z.M., Zhang G.Q., *Novel Color Microscopic Image Segmentation with Simultaneous Uneven Illumination Estimation based on PCA*, Information Technology Journal, vol. 9(8), pp. 1682-1685, 2011.
- [Weickert, 1998] Weickert J., *Anisotropic Diffusion in Image Processing*, Teubner, Stuttgart, 1998.
- [Wu, *et al.*, 2005] Wu H.S., Xu R., Harpaz N., Burstein D., Gil J., *Segmentation of intestinal gland images with iterative region growing*, Journal of Microscopy, vol. 220(3), pp. 190-204, 2005.
- [Yang and Choe, 2009] Yang H.F., Choe Y., *Cell tracking and segmentation in electron*

microscopy images using graph cuts, IEEE International Symposium on Biomedical Imaging: From Nano to Macro, pp. 306-309, 2009.

- [Yang, *et al.*, 2005] Yang L., Meer P., Foran D.J., *Unsupervised segmentation based on robust estimation and color active contour models*, IEEE Trans. Inf. Technol. Biomed., vol. 9(3), pp. 475–486, 2005.
- [Yang, *et al.*, 2006] Yang X., Li H., Zhou X., *Nuclei segmentation using marker-controlled watershed, tracking using mean-shift and Kalman filter in time-lapse microscopy*, IEEE Trans on Circuits and Systems, vol. 53(11), pp. 2405-2414, 2006.
- [Zhang, 1996] Zhang Y.J., *A survey on evaluation methods for image segmentation*, Pattern Recognition, vol. 28(8), pp. 1335-1346, 1996.
- [Zhang, 1997] Zhang Y.J., *Evaluation and comparison of different segmentation algorithms*, Pattern Recognition Letters, vol. 18(10), pp. 963 – 974, 1997.
- [Zhang, 2001] Zhang Y.J., *A review of recent evaluation methods for image segmentation*, Sixth International Symposium on Signal Processing and its Applications, Kuala Lumpur, Malaysia, pp. 148-151, 2001.
- [Zhang, 2006] Zhang Y.J., *An Overview of Image and Video Segmentation in the Last 40 Years*, Advances in Image and Video Segmentation, IRM Press, Chapter 1, pp. 1-15, 2006.
- [Zhou, *et al.*, 2009] Zhou, X., Li, F., Yan, J., Wong, S.T., *A novel cell segmentation method and cell phase identification using Markov model*, IEEE Trans. Info. Tech. Biomed., vol. 13(2), pp. 152–157, 2009.